Analecta Technica Szegedinensia
Vol. 14, No. 2 ISSN 2064-7964 2020

ESTIMATED SEASONAL DAILY EVAPOTRANSPIRATION RATES FOR A HORIZONTAL SUBSURFACE FLOW CONSTRUCTED WETLAND

[1]Dávid Somfai, [1]Ernő Dittrich, [2]Éva Salamon-Albert, [1]Anita Dolgos-Kovács

[1]Institute of Smart Technology and Engineering, Department of Environmental Engineering, Faculty of Engineering and Information Technology, University of Pécs, Boszorkány út 2, Pécs, 7624 Hungary
[2]Department of Plant Biology, Institute of Biology, University of Pécs, Ifjúság útja 6, Pécs, 7624 Hungary
e-mail: somfai.david@mik.pte.hu

Received: August 13, 2020 • Accepted: November 16, 2020

ABSTRACT

We measured the daily evapotranspiration on a horizontal sub-surface flow constructed wetland in Hódmezővásárhely, Hungary. The main focus of our research was the seasonality of evapotranspiration in this CW. We measured the water balance of the CW and searched days when no precipitation, no inlet or outlet impacted on the water balance of the constructed wetland, only the evapotranspiration. had impact on the water balance. The results show that in spring the evapotranspiration rates were between 18-42,6 mm/day, in summer 12,3-42,3 mm/ day and in autumn the values were 13,6-22,7 mm/day. The highest hourly evapotranspiration was 16,3% of the daily evapotranspiration. This value was 415 % of the average, hourly hydraulic load that can significantly affects on the effluent concentration. The results also show the morning and evening condensation which has two main effects. On the other hand, the water balance of the CW is increased, which results the decrease of the concentration of wastewater.

Keyword: horizontal subsurface flow constructed wetlands, evapotranspiration, tufted sedge, condensation, water balance

1. INTRODUCTION

Constructed wetlands (CWs), also known as treatment wetlands, are sustainable and efficient solutions used around the world to treat wastewater. There are two main types of constructed wetlands, free-surface flow systems (FSF-CW), and sub-surface flow systems (SSF-CW). SSF-CWs can be constructed with the wastewater flowing either horizontally (HSSF-CWs) or vertically (VSSF-CW) through the substrate that supports the growth of plants.

The two components of evapotranspiration that can negatively affect the water balance of constructed wetlands by causing loss of water are the transpiration of plants and the evaporation from the water surface and soil [1], [2]. Under warm and windy environmental conditions, evapotranspiration can be high [3], [4], [5].

The rate of evapotranspiration mostly depends on climatic factors, such as precipitation, temperature and wind [6], as well as the growth [7] and height of the plants in the system and the density of the leaves [8] [9]. Plants also play a key role in determining water loss in a CW [10].

Pedescoll *et al.* [11] showed that the evapotranspiration in subsurface flow constructed wetlands was 20–22 mm/day, the water loss via evapotranspiration was around 44% of the hydraulic load, but there were days when it reached 100%. Freedman *et al.* [12] measured similar values of 20 mm/day but observed 40 mm/day in certain times of the day. In another study, values of evapotranspiration in HSSF-CWs fluctuated between 19.5 and 40 mm/day [13].

Tuttolomondo *et al.* [14] measured evapotranspiration in a constructed wetland in Italy and observed that on some summer days evapotranspiration reached 25–35 mm/day; this value was 20–30% of the hydraulic load. Tanner [15] studied a evapotranspiration rates of a constructed wetland during a hot (30-33 °C) summer in New Zealand, the values measured were around 7.1–11.7 mm/day meaning that transpiration accounted for 20% of the daily hydraulic load.

DOI: https://doi.org/10.14232/analecta.2020.2.1-12

Milani *et al.* [16] investigated evapotranspiration rates in twelve pilot-scale horizontal subsurface flow constructed wetlands in eastern Sicily in which they had five different species. The results showed that the evapotranspiration rates varied between 7,35 to 17,31 mm/ day.
Queluz *et al.* [17] had similar values in pilot-scale HSSF-CWs, their results were 4,9 to 20 mm/day, nevertheless, they obtained very high results at around 46 mm/day. They did not find the exact reason for this extreme value.
Yano *et al.* [18] studied the influence of the plant growth on the evapotranspiration. The results showed that the evapotranspiration increased the growth of the plants, and that there were weeks when the water loss via evapotranspiration increased up to 80 % of the inflow rate. Hamouri *et al.* [19] measured the water loss via evapotranspiration in HSSF-CWs in Marocco. They concluded that the water loss amounted to 11-17 % of the inflow rate.
Chazarenc *et al.* [20] estimated evapotranspiration using a 1 m^2 pilot-scale constructed wetland planted with Common reed (*Phragmites australis*). The evapotranspiration water loss accounted for 13–40% of the hydraulic load. The results showed that in constructed wetlands evapotranspiration increased hydraulic retention time and decreased dispersion [20].
As a result of evapotranspiration, concentration of solutes increases in constructed wetlands [21]. The highest evapotranspiration rates in a HSSF-CW were found to occur at midday, at around 12:00 to 13:00 [22], [23].
Bialowiec *et al.* [9] measured the pollutant removal efficiency of constructed wetlands under different evapotranspiration rates and concluded that higher evapotranspiration caused higher effluent concentrations. In another study of the relationship between evapotranspiration and removal efficiency, the results showed that increased rate of evapotranspiration positively affected outflow Biochemical Oxygen Demand (BOD_5) and Chemical Oxygen Demand (COD) concentrations [24].
The above findings show that evapotranspiration indirectly affects effluent water quality, thus it is imperative to obtain in-depth knowledge about evapotranspiration in subsurface flow constructed wetlands. Among the many studies on water management processes of surface flow constructed wetlands [25] [26] [27], only a few contain detailed water balance analysis of subsurface flow constructed wetlands [20].
These studies are not enough detailed about these viewpoints:

- Don't show any information about morning and evening condensation processes.
- Don't show enough detailed analysis of separation between daytime and night time periods.
- Don't show enough detailed analysis of changing the hourly evaporation rates.

These detailed information are very important because the effluent concentration of wastewater can be changed dynamically in a day by the highly changing evaporation rates, and condensation processes.
In this study, our aims are to estimate the answers to these interesting scientific viewpoints. Otherwise, we don't know so detailed analysis of CW's evaporation processes from the Middle-European region.

2. MATERIALS AND METHODS

2.1. Study site

Our study site was a subsurface flow constructed wetland treatment plant near Hódmezővásárhely (Hungary). This constructed wetland treats 1-1.5 m^3 of wastewater per day from a dairy farm. The technology consists of a septic tank, a pump system, VSSF-CW planted with common reed (*Pragmites Australis*), HSSF-CW planted with Tufted sedge (*Carex elata* All.), a polishing pond and a trickling system planted with poplar trees (*Populus* spp). This study focuses exclusively on HSSF-CW.

2.2. Species description

Tufted sedge is a widespread species found all over Europe, except for the Mediterranean. This species is native to Hungary and is generally abundant throughout much of its Central European range

DOI: https://doi.org/10.14232/analecta.2020.2.1-12

(http://www.iucnredlist.org). It can be found in shallow water, preferring oligotrophic to eutrophic and often calcareous freshwater habitats, and in seasonally flooded areas. The primary life form of the species is perennial and aquatic. Tufted sedge grows as a tussock-forming graminoid, often forming extensive stands. Being a Eurasian temperate flora element, it presents broad ecological tolerance to light as well as the moisture, nitrogen and salt content of the soil. It can be up to 40-120 cm tall, has a triangular shape and is very rough at the top (https://www.brc.ac.uk/plantatlas). The cross section of the leaf is M-shaped, the blade is 2-5 mm wide, greyish-green, and the underside of the leaf is dull. Tufted sedge is a hypostomatic plant, which means that the stomatal openings for gas exchange are on the underside of the leaf [28]. Stomatal openings are also generally found on the leafy floral shoots (personal observation). Mostly in summer, drained soil conditions can strongly decrease the stomatal conductance-induced transpiration rate [29].

2.3. Measurement method

For investigation of the daily fluctuation, we were looking for days characterized by:

- No inflow and outflow
- No precipitation
- Significant decrease in daily water levels

Apparently, the change in water level on these days depends only on the extent of evapotranspiration. A significant amount of daily water level change was needed to eliminate measurement inaccuracies in the water pressure transmitters. Water level observations were recorded at 10-s intervals on the test days to an accuracy of 0.1 mm (± measurement error). We found 16 days to test. Three water level pressure transmitters were installed in the object under investigation. Perforated pipes were placed vertically in the CW. The level transmitters were placed in these pipes, and all three series of data were used and the values measured were averaged by the 3 pressure transmitters so that we could eliminate measurement errors and thus accurately track hourly changes.

3. RESULTS AND DISCUSSION

The measurement data values provided by pressure transmitters and the average values generated from them, and figure 1. below, shows data for day 2012-05-24.

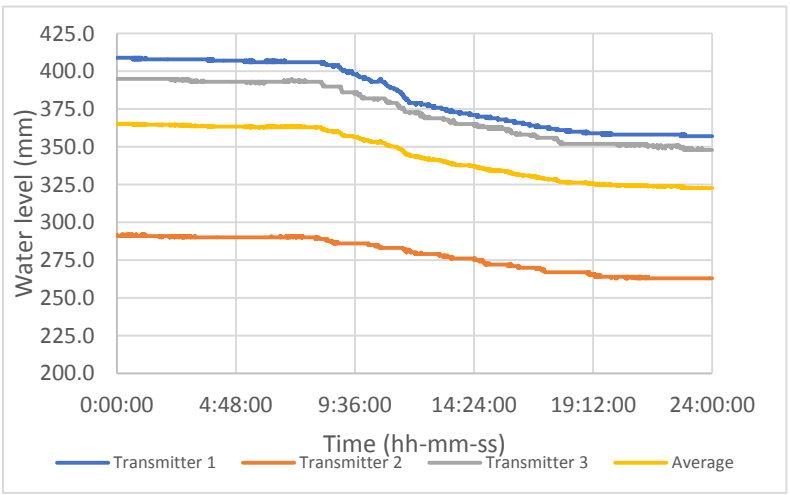

Figure 1.: Registered water levels

DOI: https://doi.org/10.14232/analecta.2020.2.1-12

The significant difference between the water level values is due to the different depths of the transmitters. For the purposes of this study, the position of the transmitters is not relevant. From our viewpoint, only the degree of water level change is important. It can be clearly seen from all 4 functions shown that during the night period the water level change is lower than during the day. This can be explained by increased evapotranspiration during the day.

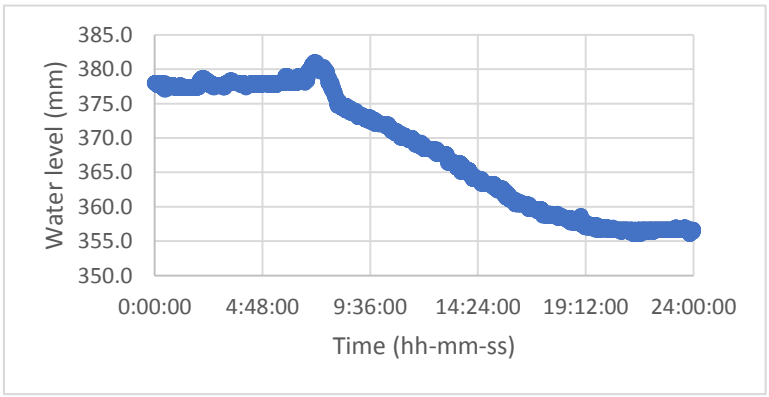

Figure 2: Evolution of average water level on the date of 2011-08-29.

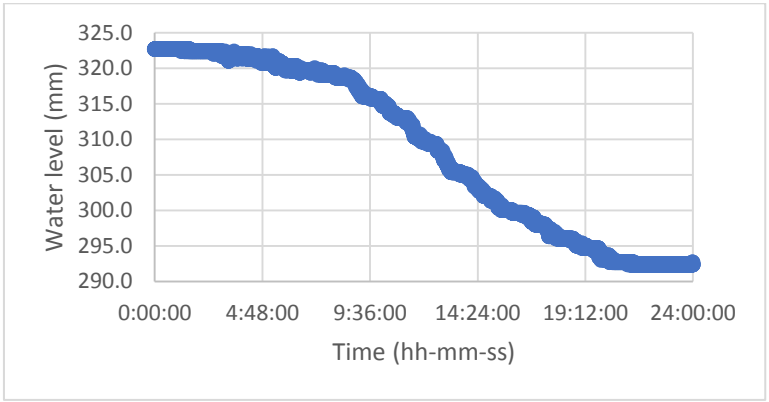

Figure 3: Evolution of average water level on the date of 2012-05-25

We have produced values of water level change as illustrated by the following figures. The two figures (Figure 2. and 3.) are noteworthy as the second figure shows a gradual decrease in water level during the day, while the first figure demonstrates an increase in the water level due to condensation after sunrise and sunset.

DOI: https://doi.org/10.14232/analecta.2020.2.1-12

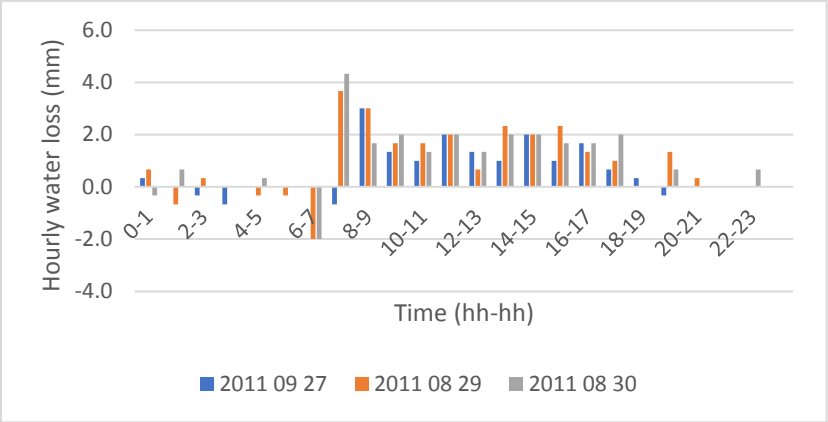

Figure 4.: Hourly changes in water level during the day

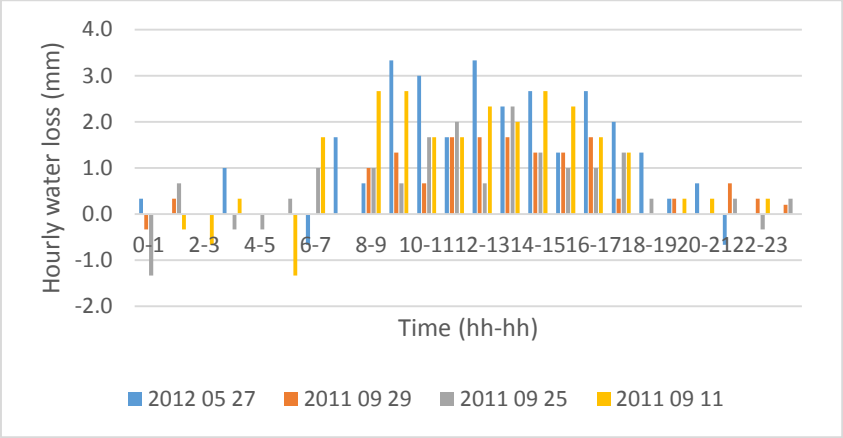

Figure 5.:Hourly changes in water level during the day

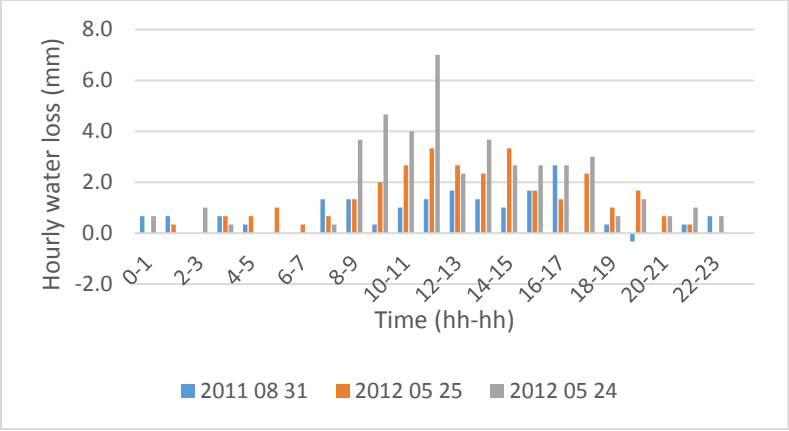

Figure 6.:Hourly changes in water level during the day

DOI: https://doi.org/10.14232/analecta.2020.2.1-12

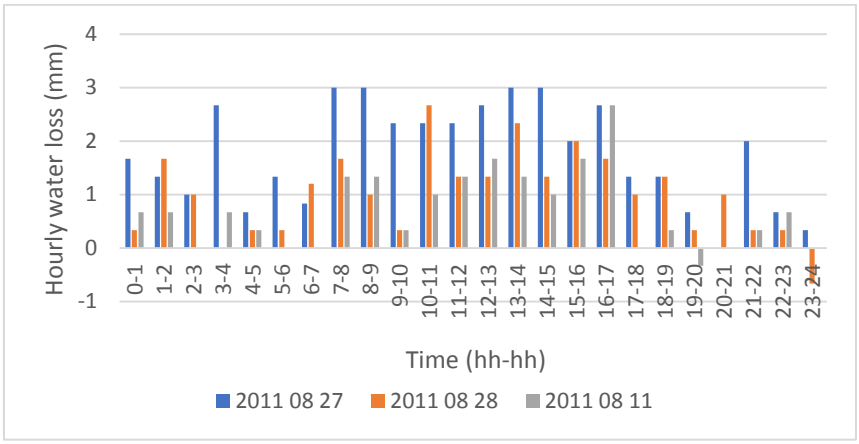

Figure 7.:Hourly changes in water level during the day

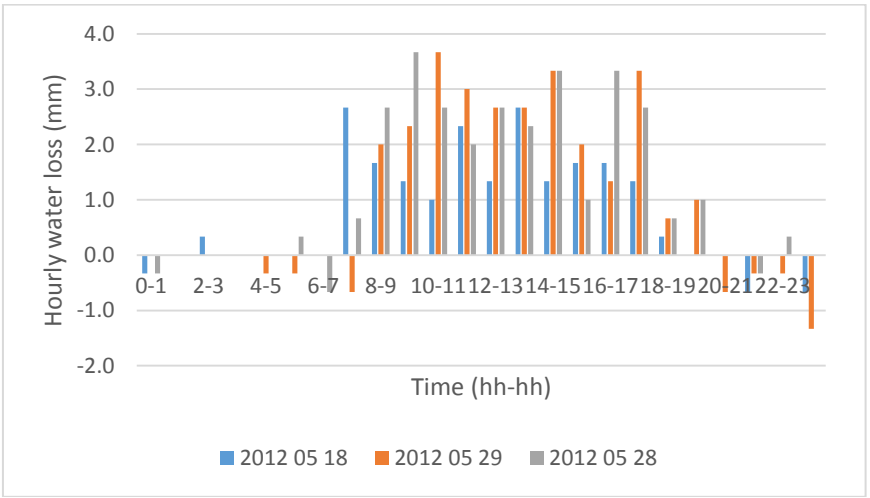

Figure 8: Hourly changes in water level during the day

Figure 4-8. show the hourly calculated water loss values. The measured days were divided into 3 groups. Values found in the first group are shown on figures 4 and 5. Here, due to the effect of morning condensation, negative values appear after sunrise. The highest hourly water change values were recorded by the transmitters One hour after sunrise. Further research is needed to explore the underlying cause.
In the second group, as shown on Figure 8, we didn't calculate negative values at morning but also at night (neither in the morning nor during the night did we calculate negative values). The values show that on 2012-05-29, this effect lasted several hours. The highest water loss values were between 10 am. and 14 pm.
In the third group, shown on Figures 6 and 7, there was no morning or evening condensation and the water loss gradually increased to its maximum at around 12 -13 pm. and then gradually decreased. On 2012-05-24, the maximum hourly water loss reached 7 mm/hour. The highest daytime water loss and the highest nighttime water loss were also recorded on this day.

DOI: https://doi.org/10.14232/analecta.2020.2.1-12

Table 1: The data for measured days

	Sunrise	Sunset	Daily hour (hh:mm)	Nightly hour (hh:mm)	Average daily temperature (C°)	Water level changes at day (mm)	Water level changes at night (mm)	Daily water level changes (mm)
2011.08.11	5:27	20:00	14:33	9:27	17	9,0	3,3	12,3
2011.08.27	5:49	19:31	13:42	10:18	26	30,3	12,0	42,3
2011.08.28	5:50	19:30	13:40	10:20	22	20,0	4,3	24,3
2011 08 29	5:53	19:26	13:29	10:31	22	22	-0,3	21,7
2011 08 30	5:54	19:24	13:30	10:30	23	19,7	2	21,7
2011 08 31	5:55	19:22	13:27	10:33	21	14	3,7	17,7
2011 09 11	6:09	19:01	12:52	11:08	24	23,7	-1	22,7
2011 09 25	6:27	18:33	12:05	11:55	16	14,4	-0,8	13,6
2011 09 27	6:29	18:29	12:00	12:00	18	14,4	-0,7	13,7
2011 09 29	6:32	18:25	11:53	12:07	17	12,7	1	13,7
2012 05 18	5:02	20:08	15:07	8:53	14	19,7	-1,7	18
2012 05 24	4:56	20:15	15:19	8:41	20	38,6	4	42,6
2012 05 25	4:55	20:16	15:21	8:39	20	28,3	2,1	30,4
2012 05 27	4:54	20:17	15:23	8:37	17	25	2	27
2012 05 28	4:53	20:18	15:25	8:35	17	28	0	28
2012 05 29	4:52	20:19	15:27	8:33	18	26	-2	24

Table 1. shows the data for each day, the day/night ratio, and the daytime and nighttime water level changes. There are days when the morning and evening condensation causes the water level to be negative. The smallest change in water level was 13.6 and the biggest was 42.6 mm. Average daily temperatures on spring days varied between 14 to 20 ° C, on summer days between 17 to 26 ° C and on autumn days between 16 to 24 ° C.

Table 2.: Daily, daytime and nighttime evapotranspiration values for days measured

Date	Evapotranspiration (mm/day)	Evapotranspiration and maximum hydraulic loading rate ratio (%)	Evapotranspiration at day time (%)	Evapotranspiration at night time (%)	Daily condensation and maximum hydraulic load rate ratio (%)
2011 08 11	12,3	30,8	73,0	27,0	0,0
2011 08 27	42,3	105,8	71,7	28,3	0,0
2011 08 28	24,3	60,8	82,2	17,8	1,8

DOI: https://doi.org/10.14232/analecta.2020.2.1-12

2011 08 29	21,7	54,3	100	0	8,3
2011 08 30	21,7	54,3	90,8	9,2	5,8
2011 08 31	17,7	44,3	79,1	20,9	0,8
2011 09 11	22,7	56,8	100	0	5,8
2011 09 25	13,6	34,0	100	0	5,8
2011 09 27	13,7	34,3	100	0	5,8
2011 09 29	13,7	34,3	92,7	7,3	0,8
2012 05 18	18,0	45,0	100	0	4,3
2012 05 24	42,6	106,5	90,6	9,4	0,0
2012 05 25	30,4	76,0	93,1	6,9	0,0
2012 05 27	27,0	67,5	92,6	7,4	3,3
2012 05 28	28,0	70,0	100	0	3,3
2012 05 29	24,0	60,0	100	0	10,0

The daily evapotranspiration values and the degree of condensation were compared to the maximum hydraulic load, which is 40 mm / day for the horizontal sub-surface flow constructed wetlands, and the daytime and nighttime evapotranspiration were separated. The results of the calculations summarized in Table 2., lead to the following conclusions:

- On the days under investigation, 71.7-93.1% of the total daily amount evaporated during the daytime hours. It follows that the concentration processes caused by evapotranspiration were 4-10 times more potent during daytime than nighttime in this constructed wetland.
- The evapotranspiration at night is significant, as there are some days when the total, daily water loss via evapotranspiration is 21.0-28.0 % of the total daily water loss, these values are similar to Dittrich *et al.* [30].
- There were days when the condensation values were high, consequently, the daytime and nighttime ratio could not be divided.
- During the spring, the estimated evapotranspiration is 18.0-42.6 mm/day, which is 45.0 - 106.5 % of the maximum hydraulic load.
- During the summer, the estimated evapotranspiration is 12.3-42.3 mm/day, which is 30.8-105.8 % of the maximum hydraulic load.
- The estimated evapotranspiration in autumn is 13.6-22.7 mm/day, which is 34.0-56.8 % of the maximum hydraulic load**.**
- Days when there was measurable condensation in the constructed wetland, the value varied between 1.8 to 10.0 % of the daily maximum hydraulic load, this phenomenon was found to decrease the concentration in the CW, especially after sunrise.

DOI: https://doi.org/10.14232/analecta.2020.2.1-12

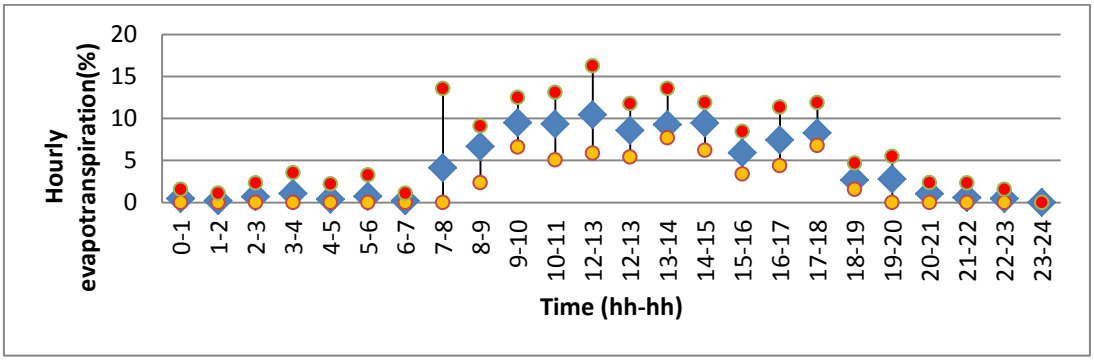

Figure 9.: Changes in the mean, minimum and maximum hourly evapotranspiration on spring days, expressed as a percentage of daily evapotranspiration

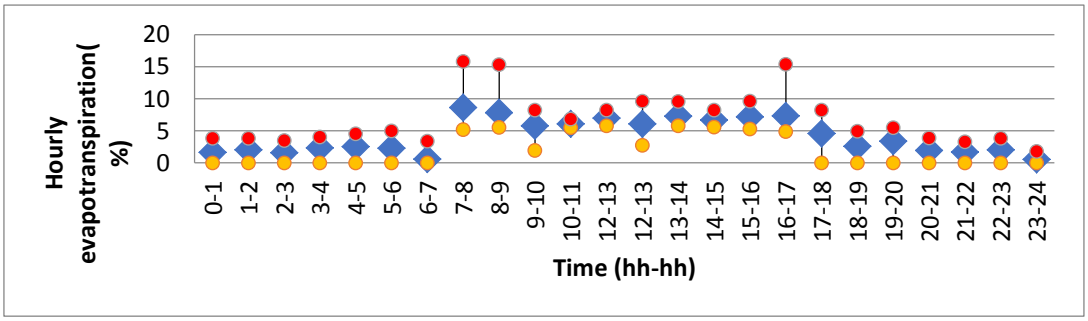

Figure 10.: Changes in the mean, minimum and maximum hourly evapotranspiration on summer days, expressed as a percentage of daily evapotranspiration

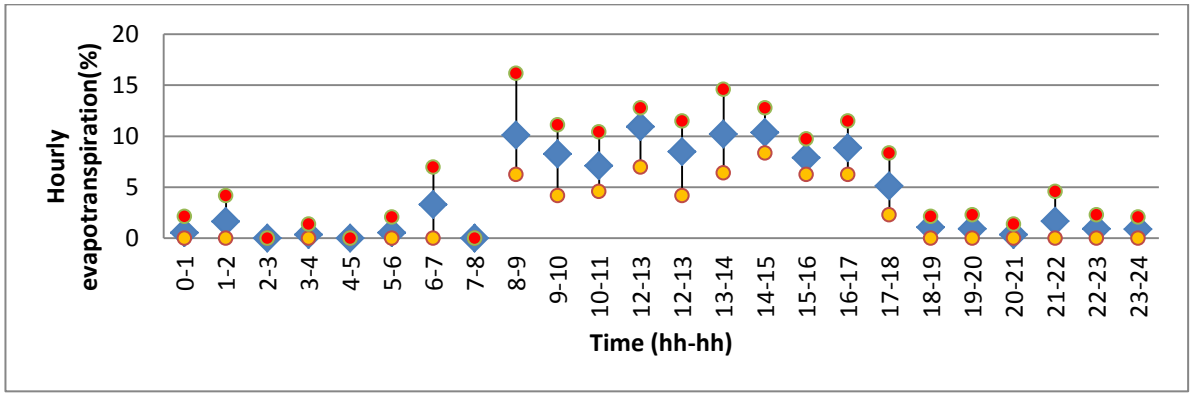

Figure 11.: Changes in the mean, minimum and maximum hourly evapotranspiration on autumn days, expressed as a percentage of daily evapotranspiration

Figures 9.-11. show changes in the mean, minimum and maximum hourly evapotranspiration rates in spring, summer and autumn, expressed as a percentage of daily evapotranspiration. The mean evapotranspiration is low at night and then gradually increases until sunrise when the evapotranspiration decreases due to the morning condensation and then increases after sunrise and reaches the mean maximum at 12 to 13 pm. and then gradually decrease. These results were similar to Galvao *et al.* [23]. There are

DOI: https://doi.org/10.14232/analecta.2020.2.1-12

days when the maximum amount of evapotranspiration is in the morning and then a gradual decrease is observable.
The Figure 9. shows that the peak spring hourly evapotranspiration was around 16.3 % of the daily evapotranspiration, this value was around 15.8 % in summer and 16.2 % in autumn. Estimating the maximum spring hourly evapotranspiration from 42.6 mm/day, this value is 6.94 mm/h, 415 % of the average hourly hydraulic load (1.7 mm/h) of the cw. In summer and autumn these values are 229 % and 150 % of the average hourly hydraulic load of the CW. From This result led to the conclusion that the concentration processes occurring during the spring and summer can be extremely significant.

4. CONCLUSIONS

We measured the hourly, daily and seasonal evapotranspiration of a horizontal sub-surface flow constructed wetland for four months. We found 16 days when there was no precipitation and there was no inlet or outlet affecting this constructed wetland, meaning that the only effect upon the water balance of this CW was the evapotranspiration.
On the days investigated, 71.7-93.1% of the total daily amount evaporated during the daytime hours. It follows that the concentration processes caused by evapotranspiration were 4-10 times more potent during daytime than nighttime in this constructed wetland. The evapotranspiration at night is significant, as there are some days when the total daily water loss via evapotranspiration is 21-28 % of the total daily water loss.
We measured the evapotranspiration under local climatic conditions: in springtime the values were between 18.0-42.6 mm/day which amounted to 45.0-106.5% of the maximum hydraulic load, in summertime 12.3-42.3 mm/day; these values are similar to results of Freedman *et al.* [12]. The values were 30.8-105.8% of the maximum hydraulic load. The values were 13.6-22.7 mm/day in autumn, which is 34.0-56.8% of the maximum hydraulic load. These values are similar to those of Dittrich *et al.* [30]
There were days when the morning and evening condensation were very high causing significant increase in water level. This has two consequences, on the one hand, condensed vapor increases the water level supplying the constructed wetland, on the other hand, due to humidity of around 100%, evapotranspiration is slightly reduced. There were some days when during the hour following the morning condensation the transmitters registered the highest hourly water loss. Further research is needed to explore this causes of this phenomenon.
There was a day in springtime when the peak hourly evapotranspiration was around 16% of the daily evapotranspiration. This value was 415 % of the average hourly hydraulic load of the CW. These values were 229 % and 150 % in summer and autumn. As a result, the concentration processes occurring during the summer may be extremely significant**.**
Our research results showed the daily evapotranspiration rates in three different seasons in horizontal subsurface constructed wetland, and the effect of the morning and evening condensation in Central Eastern European region.
In the future, we plan to conduct 24-hour on-site measurements at the same field site in order to clarify the evaporation transpiration ratio as a function of local climatic conditions. Based on these measurements, we expect to develop an environment-calibrated engineering model to better estimate system-level evapotranspiration processes and mechanisms.

ACKNOWLEDGEMENTS

We would like to thank the water and sewage management research team of the University of Pécs, Faculty of Engineering and Information Technology for their cooperation. The project was supported by the European Union, co-financed by the European Social Fund under grant agreement No. EFOP-3.6.1.-16-2016-00004. The research was financed by NKFIH in Hungary, within the framework of the 2020-4.1.1-TKP2020 3rd thematic programme of the University of Pécs.

REFERENCES

[1] Allen, R.G. Pereira, L.S. Raes, D. & Smith, M. (1998): Crop evapotranspiration guidelines forc omputing crop water requirements. *FAO Irrigation and Drainage Paper* **56**. United Nations Food and Agriculture Organization. Rome. Italy.

[2] Kadlec, R.H. & Wallace, S.D. 2009 Treatment Wetlands. 2nd ed. Taylor and Francis Group LLC. Boca Raton. 107–113.

[3] Białowiec, A. & Wojnowska - Baryla, I.(2007): The efficiency of landfill leachate evapotranspiration in soil-plant system with reed Phragmitesaustralis. *Ecohydrologic Hydrobiologic* **7** (3–4). 331–337. doi.org/10.1016/S1642-3593(07)70116-7

[4] Albuquerque, A., Arendacz, M., Gajewska, M., Obarska-Pempkowiak, H., Randerson, P.F. & Kowalik, P. (2009): Removal of organicmatter and nitrogen in an horizontal subsurface flow (HSSF) constructed wetland under transient loads. *Water Science and Technology* **60,** 1677–1682. doi:10.2166/wst.2009.548

[5] Headley, T.R., Davison, L., Huett, D.O. & Müller, R. (2012): Evapotranspiration from subsurface horizontal flow wetlands planted with Phragmites australis in sub- tropical Australia. *Water Research* 46 (2). 345–354. doi: 10.1016/j.watres.2011.10.042.

[6] Kumar, R., Jat, M.K. & Shankar, V. (2012): Methods to estimate irrigated reference crop evapotranspiration – a review. *Water Science and Technology*. **66** (3). 525–535. doi: 10.2166/wst.2012.191

[7] Borin, M. Milani, M. Salvato, M. & Toscano, A. (2011): Evaluation Phragmites australis (Cav.) Trin. Evapotranspiration in Northern and Southern Italy. *Ecological Engineering* 37 (5). 721–728. doi: 10.1016/j.ecoleng.2010.05.003

[8] Pauliukonis, N. & Schneider, R. (2001): Temporal patterns in evapotranspiration from lysimeters with three common wetland plant species in the eastern United States. *Aquatic Botany* **71**. 35–46. doi:10.1016/S0304-3770(01)00168-1

[9] Bialowiec, A., Albuquerque, A. & Randerson, P.F. (2014): The influence of evapotranspi-ration onvertical flow subsurface constructed wetland performance. *Ecological Engineering* **67.** 89–94. doi: 10.1016/j.ecoleng.2014.03.032

[10] Leto, C., Tuttolomondo, T., La, Bella, S., Leone, R. & Licata, M. (2013): Effects of plant species in a horizontal subsurface flow constructed wetland – phytoremediation of treated urban wastewater with Cyperusalternifolius L. and Typhalatifolia L. in the West of Sicily (Italy*). Ecological Engineering* **61,** 282–291. doi: 10.1016/j.ecoleng.2013.09.014

[11] Pedescoll, A., Sidrach-Cardona, R., Sánchez, J.C. & Bécares, E. (2013): Evapotranspiration affecting redox conditions in horizontal constructed wetlands under Mediterranean climate: influence of plant species. *Ecological Engineering* **58.** 335–343. doi: 10.1016/j.ecoleng.2013.07.007

[12] Freedman, A., Gross, A., Shelef, O., Rachmilevitch, S. & Arnon, S. (2014): Salt uptake and evapotranspiration under arid conditions in horizontal subsurface flow constructed wetland planted with halophytes. *Ecological Engineering* **70:** 282-286. doi.:10.1016/j.ecoleng.2014.06.012

[13] Beebe, D. A., Castle, J. W., Molz, F.J. & Rodgers, Jr. (2014): Effects of evapotranspiration on treatment performance in constructed wetlands: Experimental studies and modelling. *Ecological Engineering* Volume **71**, 394-400. doi:10.1016/j.ecoleng.2014.07.052

[14] Tuttolomondo, T., Licata, M., Leto, C., Leone, R. & La, Bella, S. (2015): Effect of plant species on water balance in a pilot-scale horizontal subsurface flow constructed wetland planted with Arundodonax L. and Cyperusalternifolius L. – Two-year tests in a Mediterranean environment in the West of Sicily (Italy). *Ecological Engineering*. Volume **74**. 79-92. doi: 10.1016/j.ecoleng.2016.01.038

[15] Tanner, C. C., (1995): Accumulation of organic solids in gravel-bed constructed wetlands. *Water Science and Technology* Vol. **32**. No.3., 229-239. doi: 10.1016/0273-1223(95)00624-9

DOI: https://doi.org/10.14232/analecta.2020.2.1-12

[16] Milani M., Marzo A.,Toscano A. , Consoli S. , Cirelli G. L. , Ventura D. ,Barbagallo S. (2019): Evapotranspiration from horizontal subsurface flow constructed wetlands planted with different perennial plant species. *Water* 11(10):2159 doi: 10.3390/w11102159
[17] Queluz J. G. T., Francisca Franciana Sousa Pereira F. F. S., Sánchez-Román R. M. (2018): Evapotranspiration and crop coefficient for Typha latifolia in constructed wetlands. *Water Quality Journal.* **53** *(*2): 53-60. doi.org/10.2166/wqrj.2018.041
[18] Yano T., Nakayama M., Yamada K., Inoue-Kohama A., Sato S., Enari K. (2017): Influence of Growth of Reeds on Evapotranspiration in Horizontal Subsurface Flow Constructed Wetlands. *Environment and Ecology Research* 5(6): 427-435. doi: 10.13189/eer.2017.050603
[19] Hamouri El B., Nazih J, Lahjouj J. (2007): Subsurface-horizontal flow constructed wetland for sewage treatment under Moroccan climate conditions. *Desalination* **215**: 153–158. doi: 10.1016/j.desal.2006.11.018
[20] Chazarenc, C. Merlin, G. & Yves, G. (2003): Hydrodynamics of horizontal subsurface flow constructed wetlands. *Ecological Engineering.* **21**, 165-173. doi:10.1016/j.ecoleng.2003.12.001
[21] Kadlec, R.H., Knight, R.L., Vymazal, J., Brix, H., Cooper, P. & Haberl R. (2000): Constructed wetlands for pollution control: processes. performances. design and operation. IWA Specialist Group on Use of Macrophytes in Water Pollution Control. IWA Publishing. London. UK
[22] Jacobs, J.M., Myers, D.A., Anderson, M.C & Diak, G.R. (2002): GOES surface insolation to estimate wetlands evapotranspiration. *Journal of Hydrology* **266**, 53–65.. doi:10.1016/S0022-1694(02)00117-8
[23] Galvão, A., Matos, J., Ferreira, F. & Correia, F., (2010): Simulating flows in horizontal subsurface flow constructed wetlands operating in Portugal. Ecological Engineering 36: 596–600. doi: 10.1016/j.ecoleng.2009.11.014
[24] Tuttolomondo, T., Leto, C., La, Bella, S., Leone, R., Virga, G. & Licata, M. (2016): Water balance and pollutant removal efficiency when considering evapotranspiration in a pilot-scale horizontal subsurface flow constructed wetland in Western Sicily (Italy). *Ecological Engineering.* Volume **87**. 295-304. doi: 10.1016/j.ecoleng.2015.11.036
[25] Konyha, D. K.; Shaw, D.T. & Weiler, K. W. (1995): Hydrologic design of a wetland: advantages of continuous modelling. *Ecological Engineering.* **4** 99-116. doi: 10.1016/0925-8574(93)E0052-R
[26] Kadlec, R.H. (1999): Chemical, physical and biological cycles in treatment wetlands. *Water Science and Technology* **40:** 37-44. doi:10.1016/S0273-1223(99)00417-5
[27] Kadlec, R.H. (2006): Water temperature and evapotranspiration on surface flow wetland sin hot arid climate. *Ecological Engineering.* **26:** 328-340. doi:10.1016/j.ecoleng.2005.12.010
[28] Dean, M. & Ashton, P.A. (2008): Leaf surfaces as a taxonomic tool: the case of Carex section Phacocystis (Cyperaceae) in the British Isles. Plant Systematics Evulotion **273**: 97–105. doi: 10.1007/s00606-008-0029-8
[29] Busch., J. & Lösch., R. (1998): Stomatal behaviour and gas exchange of sedges (Carex spp.) under different soil moisture regimes. *Physics and Chemistry of the Earth* **23**: 443-448. doi: 10.1016/S0079-1946(98)00051-2
[30] Dittrich E., Salamon-Albert É., Somfai D., Dolgos-Kovács A., Kiss T. (2019): Transpiration effect of Tufted sedge for a horizontal subsurface flow constructed wetland. Water Sci Technol (2019) 79 (10): 1905–1911.https://doi.org/10.2166/wst.2019.187

Analecta Technica Szegedinensia
Vol. 14, No. 2 ISSN 2064-7964 2020

THE FREQUENCY OF THE TWO LOWEST ENERGIES OF INTERACTION IN DIPOLAR HARD SPHERE SYSTEMS

Sandor Nagy

Daniel Berzsenyi Teacher Training Centre, Károly Gáspár tér 4. A-building, 9700, Szombathely, Hungary,
e-mail: sata123.sandor@gmail.com

Received: September 13, 2020 • Accepted: October 28, 2020

ABSTRACT

This publication was inspired by the study of chaining in dipolar systems. Two adjacent particles form a chain is usually decided by energy or distance criterion. This prompted the author to investigate the frequency of interaction energy between nearby chain-forming particles in the dipolar system. So what is the frequency of the two lowest energies. Does have raison d'etre of the energy-based chaining criterion? Because if so, in the frequency chart qualitative change should have see at 70-75%, compared to the lowest possible energy. No such qualitative change was observed in the computer simulations. Monte Carlo simulations were performed at many densities and dipole moments in a dipolar hard sphere system. The simulation results were theoretically interpreted using the Boltzmann distribution The theoretical relationship was generalized to a wide range of density and dipole moments by fitting three suitable parameters. The fitting was necessary due to the compressive effect of density.

Keywords: interaction energy, pair energy, dipolar hard spheres

1. INTRODUCTION

Dipolar particles are organized into chains under certain conditions. There are some types of chaining criteria. The most common is the energy criterion: e.g. if the pair energy between two adjacent particles is less than 70-75% of the minimum pair energy, they form a chain [1-4]. Another criterion combines the distance and the energy criterion [5, 6]: if the pair energy is negative and the distance is less then 1.3 (in diameter unit). So the criterion in all cases is unit jump-like. According to the author, this assumes that there must also be some kind of unit jump-like change in the energy between the particles. Therefore, in the first half of the study, Monte Carlo simulation results on the energy distribution between adjacent particles are presented. The simulations were performed in a dipolar hard sphere (DHS) system. No unit jump-like change was experienced in the pair energy distribution. A similar study was performed by Tavares et al. [4], but they treated the lowest and second lowest pair energies separately. However, they did not find a unit jump-like change either. The shape of the curves was then explained using the Boltzmann distribution. The increasing of density modifies the initial distribution, so parameters were fitted.

2. SIMULATION RESULTS

Monte Carlo simulations of DHS fluids were performed using a canonical NVT ensemble. Boltzmann sampling [7], periodic boundary conditions and the minimum-image convention were applied. In order to take into account the long-range character of the dipolar interaction, the reaction field method under boundary conditions of conduction was used. After 100,000 equilibration cycles, 500,000 production cycles were conducted involving N = 1000 particles. In each cycle, for each particle, the pair energy belonging to the two lowest energy neighbors was taken into account. In the DHS system, the particles must not be closer to each other than the particle diameter (d), and at a greater distance, the HS portion of the pair energy between them is zero. The dipolar pair energy is given by the following relation for point dipoles in 3 dimensions:

$$U_{ij}^{dd} = -\frac{m^2}{r_{ij}^3}\left[3\left(\hat{\boldsymbol{m}}_i \cdot \hat{\boldsymbol{r}}_{ij}\right)\left(\hat{\boldsymbol{m}}_j \cdot \hat{\boldsymbol{r}}_{ij}\right) - \left(\hat{\boldsymbol{m}}_i \cdot \hat{\boldsymbol{m}}_{j_j}\right)\right] \quad (1)$$

DOI: https://doi.org/10.14232/analecta.2020.2.13-18

where the particles have dipole moments of strength m as well as an orientation given by unit vector $\hat{\boldsymbol{m}}$, and the distance between the centers of the particles is denoted by r_{ij} and $\hat{\boldsymbol{r}}_{ij} = \boldsymbol{r}_{ij}/r_{ij}$. The dot symbolizes scalar product. Based on this, it can be easily obtained that the smallest energy value, when the dipoles are in the tail-to-nose position, is: $U_{min}^{dd} = -2m^2/d^3$. In general and hereafter, this will be the unit of energy, as this is the most favorable position in terms of energy, to which the percentage limits mentioned in the introduction. The most unfavorable position (nose to nose) is when two particles are at the minimum distance (d) but stand in opposite directions. The associated energy value is: $U_{max}^{dd} = 2m^2/d^3$. As the distance increases, these extreme energies decay cubically. Let introduce the following variable: $u = U^{dd}/U_{min}^{dd}$, and the reduced quantities as follows: $\rho^* = \rho d^3$, $m^* = m/\sqrt{d^3 k_B T}$, where ρ and d are the concentration and diameter of the particles, k_B is the Boltzmann constant, and T is the temperature. Then the minimum reduced value of the pair energy: $\left(U_{min}^{dd}\right)^* = -2m^{*2}$ (while $u_{max} = 1$), and the maximum reduced value of the pair energy: $(U_{max}^{dd})^* = 2m^{*2}$ (while $u_{min} = -1$). Two osculant particles can be in a favorable energetic position even if they are in opposite directions, but then they must be located next to each other in antiparallel position. In this case: $(U^{dd})^* = -m^{*2}$, and $u = 0.5$. It has a symmetrical (parallel) position: $(U^{dd})^* = m^{*2}$, and $u = -0.5$. Fig. 1 shows all this.

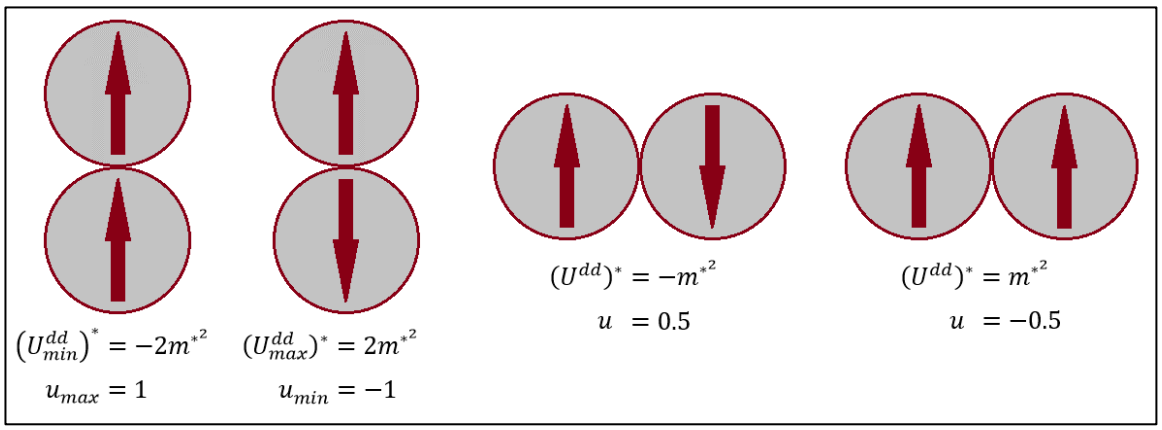

Figure 1. The privileged positions of the dipole pairs and the associated pair energies.

Fig. 2 shows the probability density functions (denoted by P) of the two lowest pair energy interactions, as simulation results for 3 dimensions. The dipole moment values from left to right: $m^* = 1$, $m^* = \sqrt{3}$, and $m^* = \sqrt{5}$. Each subfigures has 3 lines for 3 different reduced densities: $\rho^* = 0.1$ (green), $\rho^* = 0.5$ (blue), $\rho^* = 0.9$ (red). The x-axis shows the dipolar pair energy as a proportion of the minimum pair energy. Integrating P we get that:

$$\int_0^1 P(U^{dd})du = 1 \tag{2}$$

Because it is true for all particles that the maximum values of the two lowest energy pair energies are zero. It is possible that the pair energy taken with a nearby particle is greater than zero, but even for that particle

DOI: https://doi.org/10.14232/analecta.2020.2.13-18

there is a particle with zero pair energy at high distance. However, only nearby particles can be considered in the chaining, so those parts of the curves where *u* approaches 1 are of interest to us.

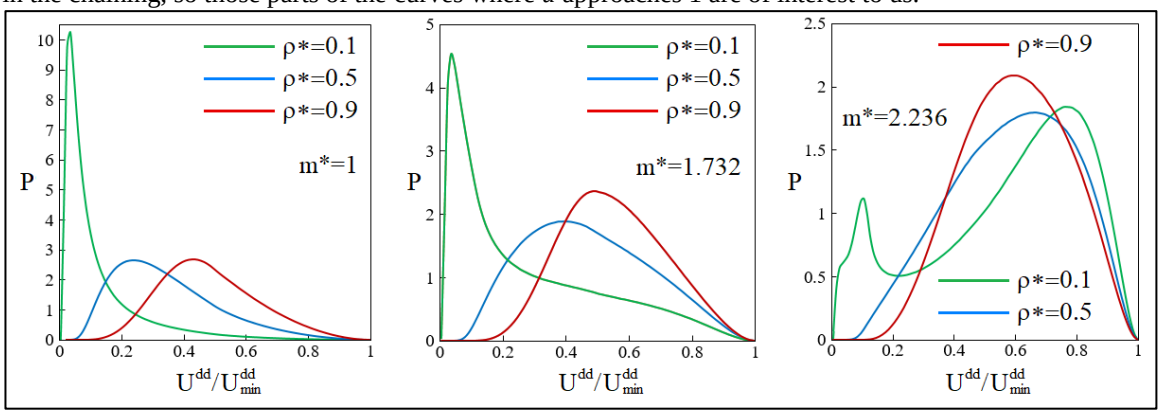

Figure 2. Simulation results of the probability density functions of the two lowest pair energy.

It can be seen that increasing both of density and dipole moment pushes the maximum of the curves to the right, towards the lower energies. The higher density forces the particles to a close location and the higher dipole moment also means lower pair energy, which increases the frequency of energetically favorable situations.

3. THEORY

The Boltzmann distribution is used to explain the curves on Fig. 2. According to the Boltzmann distribution, the probability that two particles are in a state characterized by U^{dd} pair energy in DHS conditions, is given by the following relation:

$$P(U^{dd})du = \frac{g(U^{dd})\,\exp(-U^{dd}/k_BT)}{\int_0^1 g(U^{dd})\,\exp(-U^{dd}/k_BT)du}du \tag{3}$$

where $g(U^{dd})$ is the number of states that realize a given dipolar energy. In DHS system for the pair energy of two dipoles with each other, the size of a part of a five-dimensional Euclidean space gives the size of $g(U^{dd})$. The direction of the two dipoles is determined by two-two angle values: the polar angle (ϑ), and the azimuthal angle (φ). The relative spatial position of the two dipoles is given by the Cartesian coordinates (x, y, z) or the two mentioned angles and a distance (ϑ, φ, r). These are seven parameters from which the direction of one of the dipoles can be fixed, so the other five parameters remain independent. The size of this five-dimensional Euclidean space is shown on a logarithmic scale as a function of pair energy on Fig. 3. The calculation can be performed with a simple computer algorithm. While keeping one of the dipoles fixed, the five parameters are scanned evenly with sufficient accuracy, and determining the dipolar energy between the two dipoles, and if the dipolar energy is in the vicinity of the selected energy level, the configuration is included in the summation. The number of aggregated configurations specifies the size of Euclidean space for that energy level. Mathematically, this is expressed by the following formula:

$$g(U^{dd}) = \int_{U^{dd}-\varepsilon<U^{dd}\le U^{dd}+\varepsilon} p(x)dx\,p(y)dy\,p(z)dz\,p(\vartheta)d\vartheta\,p(\varphi)d\varphi \tag{4}$$

DOI: https://doi.org/10.14232/analecta.2020.2.13-18

where $0 \leq \vartheta < \pi$ and $0 \leq \varphi < 2\pi$, and for Cartesian coordinates (e.g. x), $p(x)dx = dx/(x_{max} - x_{min})$, and $p(\vartheta)d\vartheta = sin\vartheta d\vartheta/2$, and $p(\varphi)d\varphi = d\varphi/2\pi$. Fig. 3 shows that the curve $g(U^{dd})$ (blue line) approaches the linear on a logarithmic scale, at least for small *u* values, furthermore, for *u* values close to 1, it deviates from the line toward zero. Therefore, the function $g(U^{dd})$ can be approximated by the expression:

$$g(U^{dd}) \approx A \exp\big(B(1-u)\big)cos^{C}\left(\frac{\pi}{2}u\right) \tag{5}$$

where *A*, *B*, and *C* are constants. The value of *A* depends on how close u is to zero, since at zero the frequency becomes infinite. However, the values of *B* and *C* can be determined exactly by fitting. On Fig. 3, the constant B indicates the slope of the straight line, while the constant C indicates the degree of deflection. From the fitting: *B=5.034* és *C=1.624*. On Fig. 3 the blue line indicates the size of the Euclidean space determined from the computer algorithm, and the red dotted line is the curve of the fitted formula (5) with the mentioned data.

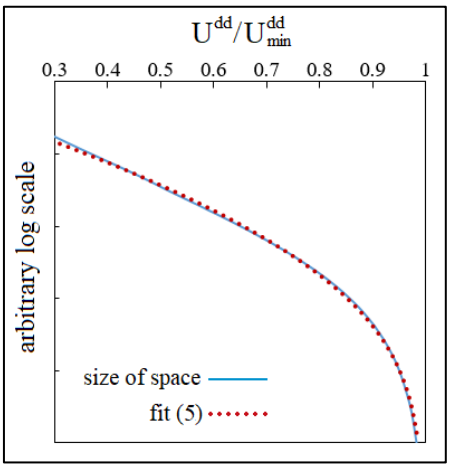

Figure 3. The number of states of the pair energy in dipolar hard sphere system

Comparing (3) and (5) for the frequency of the pair energy, we get:

$$P(U^{dd})du \approx A \exp\big(B(1-u)\big)cos^{C}\left(\frac{\pi}{2}u\right)\exp\big(2um^{*2}\big) \tag{6}$$

Hereinafter, this term is used to fit the curves shown on Fig. 2, even if the increasing of dipole moment and density obviously distort the initial *B* and *C* data. Fig. 4 shows the fitting of (6) for three different dipole moments. The density does not yet appear here because (6) does not include it. For infinite dilute fluids, the distributions of pair energy are different for different dipole moments. The solid lines are the exact probability density functions, expressed as the product of the real Euclidean space size and the pair energy term:

$$P(U^{dd})du = g(U^{dd})\exp\big(2um^{*2}\big) \tag{7}$$

DOI: https://doi.org/10.14232/analecta.2020.2.13-18

The dotted lines show the values of (7) fitted by (6). If $m^* = 1$, then *B=6.259* and *C=1.072*. If $m^* = 1.732$, then *B=5.460* and *C=1.369*. If $m^* = 2.236$, then *B=4.731* and *C=1.584*. The vertical scale is not logarithmic.

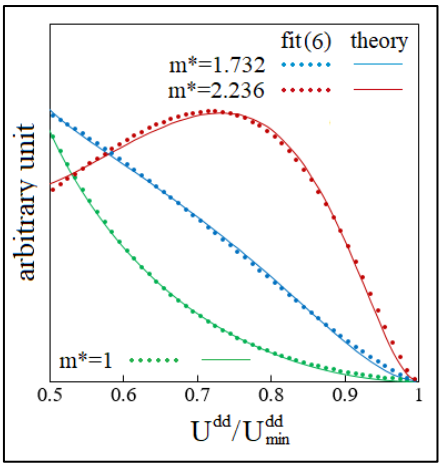

Figure 4. The probability density functions of the two lowest pair energy in infinite dilute fluids at different dipole moments.

The constants just given are, of course, distorted by the density conditions, but (6) is still suitable for describing the simulation curves shown on Fig. 2 at all densities and dipole moments. From now on, the constant A will also have a definite value, since (2) holds. Tab. 1 contains the values of the constants A, B, C at five different dipole moments and over a wide density range (per tenth), which can be substituted for (6) to obtain the pair energy distribution from at least half of the minimum pair energy to the minimum pair energy (u = 0.5-1).

Table 1. The constants for calculating the probability density function according (6).

	ρ*	0.1	0.2	0.3	0.4	0.5	0.6	0.7	0.8	0.9
m*=1	**A**	0.00725	0.0168	0.0285	0.0445	0.0653	0.0979	0.147	0.236	0.415
	B	5.353	5.173	5.034	4.846	4.649	4.351	3.989	3.461	2.726
	C	1.322	1.351	1.365	1.401	1.432	1.493	1.564	1.670	1.818
m*= 1.414	**A**	0.00778	0.0150	0.0214	0.0274	0.0343	0.0439	0.0588	0.0845	0.131
	B	4.870	4.712	4.665	4.643	4.591	4.458	4.205	3.792	3.198
	C	1.444	1.471	1.490	1.504	1.535	1.588	1.662	1.770	1.905
m*= 1.732	**A**	0.00726	0.0101	0.0114	0.0122	0.0130	0.0144	0.0171	0.0221	0.0319
	B	4.295	4.363	4.506	4.672	4.821	4.872	4.795	4.515	4.000
	C	1.568	1.560	1.563	1.569	1.595	1.638	1.706	1.810	1.946
m*=2	**A**	0.00482	0.00495	0.00469	0.00421	0.00400	0.00397	0.00427	0.00496	0.00628
	B	3.827	4.126	4.464	4.886	5.203	5.446	5.524	5.423	5.002
	C	1.641	1.616	1.604	1.590	1.608	1.652	1.724	1.815	1.876
m*= 2.236	**A**	0.00232	0.00194	0.00154	0.00124	0.00104	0.000939	0.000933	0.000990	0.00105
	B	3.246	3.823	4.487	5.132	5.701	6.149	6.386	6.370	6.293
	C	1.702	1.657	1.613	1.586	1.593	1.627	1.698	1.744	1.753

DOI: https://doi.org/10.14232/analecta.2020.2.13-18

4. CONCLUSIONS

The two lowest energies of interaction were studied by the help of Monte Carlo simulations and Boltzmann distribution in dipolar hard sphere systems. The simulations showed that there is no unit jump-like change at 70-75% of the minimum pair energy, thus, this criterion of chaining is not theoretically substantiated. Nevertheless, the frequency of pair energy can be well explained by the Boltzmann distribution (6). For this the number of states of the pair energy (Fig. 3) calculation was required. Due to the distorting effect of density, it was necessary to fit three parameters (Tab. 1). Based on this research, it can be said that a new chaining criterion needs to be established.

REFERENCES

[1] A. O. Ivanov, Z. Wang, C. Holm, Applying the chain formation model to magnetic properties of aggregated ferrofluids, Physical Review E, 69 (2004), 031206.
[2] Z. Wang, C. Holm, H. W. Müller, Molecular dynamics study on the equilibrium magnetization properties and structure of ferrofluids, Physical Review E, 66 (2002), 021405.
[3] M. Valiskó, T. Varga, A. Baczoni, D. Boda, The structure of strongly dipolar hard sphere fluids with extended dipoles by Monte Carlo simulations, Molecular Physics, 108 (1) (2010), 87-96.
[4] J. M. Tavares, J. J. Weis, M. M. Telo da Gama, Strongly dipolar fluids at low densities compared to living polymers, Physical Review E, 59 (1999), 4388.
[5] S. Kantorovich, A. O. Ivanov, L. Rovigatti, J. M. Tavares, F. Sciortino, Nonmonotonic magnetic susceptibility of dipolar hard-spheres at low temperature and density, Physical Review Letters, 110 (2013), 148306.
[6] L. Rovigatti, J. Russo, F. Sciortino, Structural properties of the dipolar hard-sphere fluid at low temperatures and densities, Soft Matter, 8 (2012), 6310.
[7] M. P. Allen, D. J. Tildesley, Computer simulation of liquids, Clarendon Press, Oxford (1987).

DOI: https://doi.org/10.14232/analecta.2020.2.13-18

Analecta Technica Szegedinensia
Vol. 14, No. 2 ISSN 2064-7964 2020

CHARACTERISATION OF ACTIVATED CHARCOAL, SAWDUST CHARCOAL AND RICE HUSK CHARCOAL AS ADSORBENTS IN WATER TREATMENT

[1]Adebola A. Adekunle, [2]Ayokunle O. Familusi, [3]Adedayo A. Badejo,
[4]Olayemi J. Adeosun, [5]Suhaib A. Arogundade

[1,2,3]Department of Civil Engineering, Federal University of Agriculture, Abeokuta, Nigeria,
[4]Department of Agricultural and Bio-Resources Engineering, Federal University of Agriculture, Abeokuta, Nigeria,
[5]School of Civil Engineering, University of Leeds, Leeds, United Kingdom
email: adebolamay@gmail.com

Received: October 1, 2020 • Accepted: November 26, 2020

ABSTRACT

This study is an investigation into the characterisation of commercial activated charcoal, sawdust charcoal and rice husk charcoal as adsorbents for water treatment. The ground rice husk and waste sawdust collected, were sieved to obtain a nominal size of 1mm, washed and oven-dried for 12hours. The two materials were pyrolyzed in a furnace for 30minutes, and the chars produced were later air-dried. The three charcoals (sawdust charcoal, rice husk charcoal, and the activated charcoal purchased from the market) were all subjected to X-ray Fluorescence (XRF) analysis, Scanning Electron Microscope (SEM) analysis and Energy Dispersive X-ray (EDX) analysis in order to characterise the filter materials. The SEM analysis showed that the three materials developed more pores, which is a property of an adsorbent. Likewise, the XRF and EDX analyses confirm that all the three adsorbents possess larger proportion of Silica, Carbon and Oxygen**.**

Keywords: Adsorbent, charcoal, pyrolysis, water treatment

1. INTRODUCTION

An adsorbent is a solid substance used to collect solute molecules from a liquid or gas [1]. Most adsorbents [2] are manufactured (such as activated carbons), but a few, such as some zeolites, occur naturally. Each material has its own characteristics such as porosity, pore structure and nature of its adsorbing surfaces. Activated charcoal or carbon [3], the oldest adsorbent known, is a highly porous, amorphous solid consisting of micro crystallites with a graphite lattice, usually prepared in small pellets or a powder. It is non-polar and cheap. The main drawbacks are that it reacts with oxygen at moderate temperatures and that of the recycling costs. Low cost activated carbon can be produced from agricultural wastes which include sawdust, banana peel, orange peel, coconut shell and rice husks [3]. Most activated carbons are made from raw materials such as nut shells, wood, coal and petroleum, which are high in carbon. Heat is used to activate the surface area of the carbon. Typical surface areas for activated carbons are approximately $1000m^2/g$. However, different raw materials produce different types of activated carbon varying in hardness, density, pore and particle sizes, surface areas, extractable, ash and pH [4, 5]. The main objective in the manufacture of granular activated carbon is the development of an optimum pore structure associated with a high surface area with minimum loss of the carbon content through carbonization and oxidation and of a product with sufficient structural strength to withstand normal usage without excessive attrition of the particles [6]. Charcoal is made by pyrolyzing wood or other organic matter such as coconut or rice husks, nut hulls, peat, etc. in earthen kilns, brick ovens, or underground pits. The process involves heating the base material to temperatures of 600 – 900^oC in the absence of oxygen. "Activation" of charcoal typically refers to physical or chemical processes designed to increase the reactive surface area of the carbon. Industrial activation processes may use chemicals and/or steam to enhance surface area, although simply heating the material to sufficient temperatures can produce a significantly activated charcoal [7]. The properties of activated carbon produced from activated sludge using sulphuric acid as a chemical activation agent, which include surface area, chemical functional groups and chemical composition reveal that it had an improved adsorption behaviour comparable to those of high performance adsorbents [8], while the work

DOI: https://doi.org/10.14232/analecta.2020.2.19-25

of [9] confirms that activated carbons produced from sawdust are good adsorbents for pesticides. The thrust of this research work is to characterise activated charcoal, sawdust charcoal and rice husk charcoal as adsorbents in water treatment.

2. MATERIALS AND METHODS

2.1. Materials and Equipment Required for the Study

The materials and equipment used in carrying out this research work include:

- Sawdust (of nominal size 1mm)
- Rice Husk (of nominal size 1mm)
- Activated Charcoal (of nominal size 2mm)
- The X-ray Fluorescence (XRF) analysis equipment (Phillips PW-1800)
- The Scanning Electron Microscope (SEM)/Energy Dispersive X-ray (EDX) analysis equipment
- Furnace (Vecstar product)
- Sieves (of 1mm and 2mm size)
- Oven.

2.2. Methods

Sample Preparation
The activated charcoal (purchased at Osogbo, Nigeria) was sieved in order to obtain a nominal size of 2mm.The waste sawdust (collected from a sawmill at Ede, Nigeria) was sieved in order to obtain a nominal size of 1mm.The rice husk collected was ground and sieved in order to obtain a nominal size of 1mm.The two materials (sawdust and rice husk) above were washed and later oven-dried at 80degree centigrade for 12hours as specified by [10]. After the two materials had been dried, they were pyrolyzed in a furnace at temperature 550^0C for thirty minutes. Then, the char produced was later air-dried.

XRF Analysis
Sample of activated charcoal was crushed with an electric crusher and then pulverized for 60 seconds using Herzog Gyro-mill (Simatic C7-621). Pellets were prepared from the pulverized sample, first by grinding 20g of the sample with 0.4g of stearic acid for 60 seconds. After each grinding, the Gyro-mill was cleansed to avoid contamination. 1g of stearic acid was weighed into an aluminum cup to act as binding agent and the cup was subsequently filled with the sample to the level point. The cup was then taken to Herzog pelletizing equipment and it was passed at a pressure of 200KN for 60 seconds. The 2mm pellets were added into a sample holder of the X-ray equipment (Phillips PW-1800) for analysis. Two distinct measurements were taken for the analysis. The whole XRF process was also repeated for sawdust charcoal and rice husk charcoal.

SEM and EDX Analyses
Sample of activated charcoal was placed on the aluminum holder stub using a double sticky carbon tape. The sample was given a conductive coating and electrically grounded. Mark was inscribed on the sample stub for identification. The sample was completely oven-dried at 60ºC for about 3 hours, and then loaded into the SEM holder of the microscope (JEOLJSM-7600F) for SEM and EDX analyses. Two distinct measurements were taken for the analyses.The whole SEM and EDX processes were also repeated for sawdust charcoal and rice husk charcoal.

DOI: https://doi.org/10.14232/analecta.2020.2.19-25

3. RESULTS AND DISCUSSION

XRF Analysis

The results obtained from XRF analysis of the filter materials are shown in Tables 1 and 2. Table 1 reveals that all the three filter materials selected, contain Silica (SiO_2), Alumina (AI_2O_3), Ferric Oxide (Fe_2O_3), Calcium Oxide (CaO), and other oxides. Loss on ignition (LOI) of about 10% was found in the sawdust and rice husk charcoals, but was absent in the activated charcoal. This suggests that the LOI is moderate (approximately 10%) and that the composition of hydrates and volatile materials in the sawdust and rice husk charcoals is moderate. The activated charcoal contains 15% ash instead of LOI found in the other two forms of charcoals. Table 2 shows that the three forms of charcoals contain trace elements like Barium, Copper, Chromium, Nickel, Zinc, Cobalt, Strontium, Lead, Scandium and Cadmium. Niobium, Rubidium and Zirconium are only found in the sawdust charcoal but not in the other two forms of charcoal.

Table 1: XRF Analysis Showing Concentrations of Oxides in the Charcoals

Major Oxides	Concentration (Wt %)		
	Activated Charcoal	Sawdust Charcoal	Rice Husk Charcoal
SiO_2	80.80	80.04	80.20
AI_2O_3	3.03	2.11	2.00
Fe_2O_3	0.05	0.72	0.15
TiO_2	0.07	-	0.20
CaO	0.10	0.18	2.75
P_2O_5	0.02	0.65	0.02
K_2O	0.11	2.16	3.45
MnO	0.01	0.06	0.41
MgO	0.01	3.12	0.01
Na_2O	0.02	0.44	0.14
LOI	-	10.52	10.60
Ash	15.60	-	-

Table 2: XRF Analysis Showing Concentrations of Trace Metals in the Charcoals

Trace Elements	Concentration (Ppm)		
	Activated Charcoal	Sawdust Charcoal	Rice Husk Charcoal
Ba	450.60	230.1	855.60
Cu	13.50	1.8	18.50
Cr	12.10	1.2	12.50
Ni	11.50	0.3	15.80
Zn	10.40	12.3	12.60
Co	10.20	2.6	10.20
Sr	7.00	1.9	4.80
Pb	10.45	0.43	12.25
Sc	7.25	0.90	10.25
Cd	0.14	1.1	0.02
Nb	-	1.5	-
Rb	-	1.0	-
Zr	-	1.6	-

DOI: https://doi.org/10.14232/analecta.2020.2.19-25

SEM Analysis

The surface morphologies of the filter materials determined using SEM are as shown in Figures 1, 2 and 3. It can be observed from Figures 1, 2 and 3 that more pores were developed in all the filter materials at the magnification of 10,000 times and the adsorbent size is smaller. The three filter materials (charcoals) possess nsmaller pores and approximately the same size. Adsorption is a surface phenomenon; therefore smaller adsorbent particle size offers a comparatively larger and more accessible surface area (more pores developed) in such a typical material (as cited in [10]).

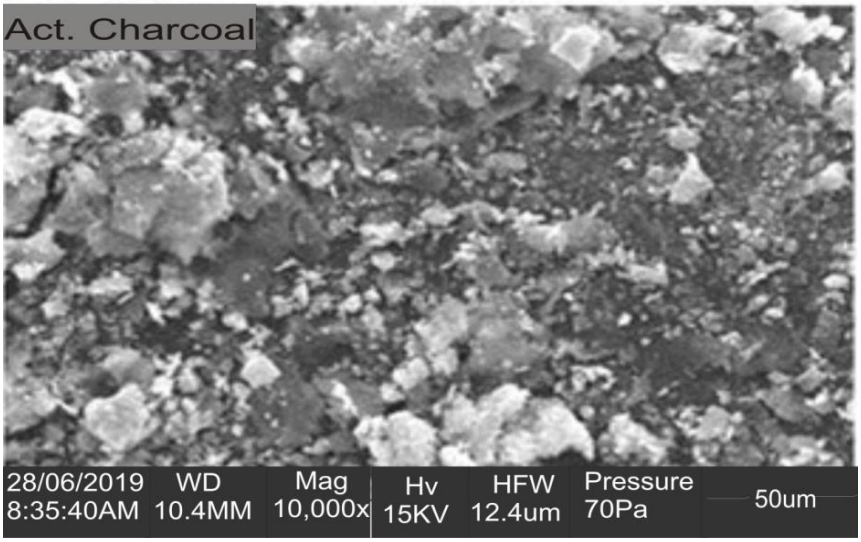

Figure 1: SEM Analysis Showing Surface Morphology of the Activated Charcoal

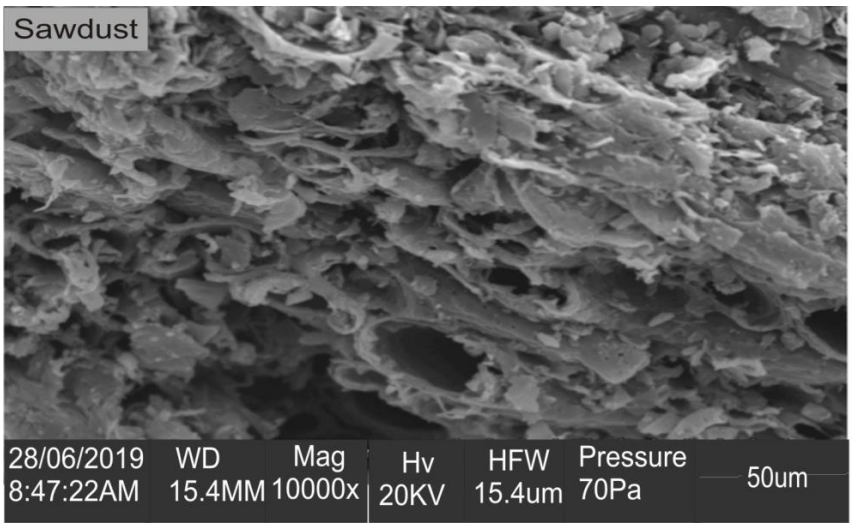

Figure 2: SEM Analysis Showing Surface Morphology of the Sawdust Charcoal

DOI: https://doi.org/10.14232/analecta.2020.2.19-25

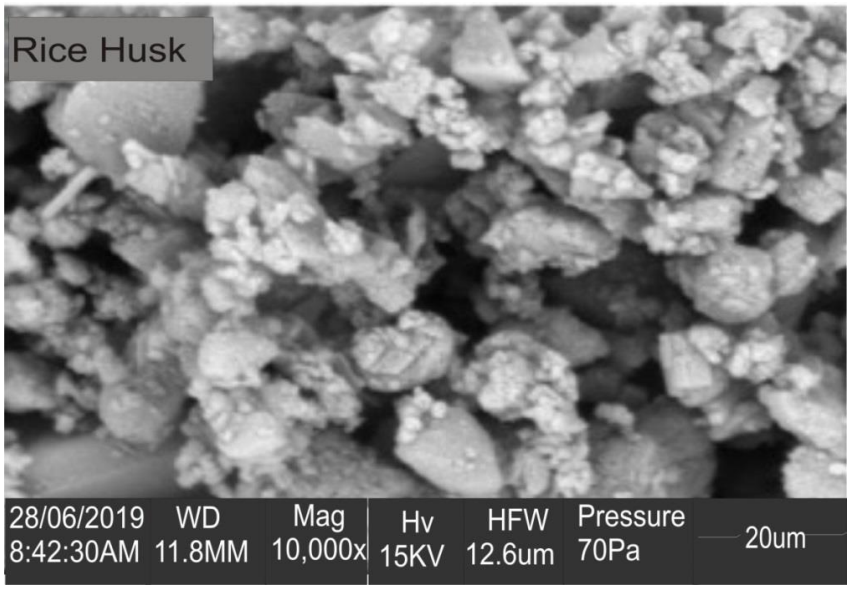

Figure 3: SEM Analysis Showing Surface Morphology of the Rice Husk Charcoal

EDX Analysis

The EDX results are shown in Figures 4, 5 and 6. Further chemical characterization (that is, EDX analysis) of the activated charcoal shown in Figure 4 revealed that the activated charcoal contains Carbon, Oxygen and Sulphur in descending order. The EDX analysis of the sawdust charcoal as shown in Figure 5 revealed that the sawdust charcoal contains Carbon, Oxygen, Silicon, Potassium, Aluminium and Calcium in descending order while Figure 6 revealed that rice husk charcoal contains Calcium, Silicon, Oxygen, Potassium, Carbon, Chlorine and Chromium in descending order.

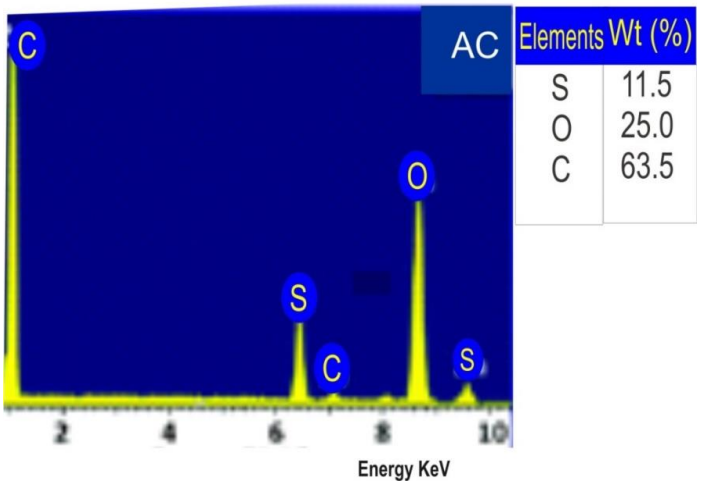

Figure 4: EDX Analysis Showing Chemical Characterisation of the Activated Charcoal

DOI: https://doi.org/10.14232/analecta.2020.2.19-25

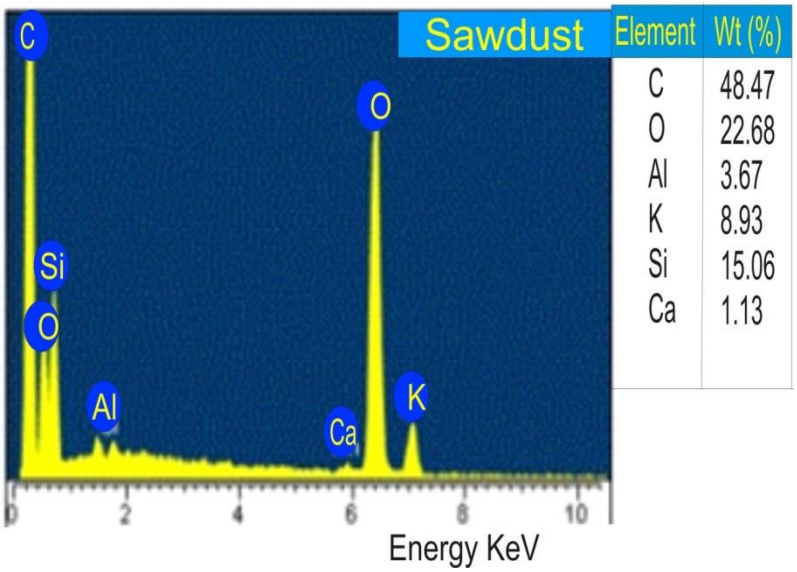

Figure 5: EDX Analysis Showing Chemical Characterisation of the Sawdust Charcoal

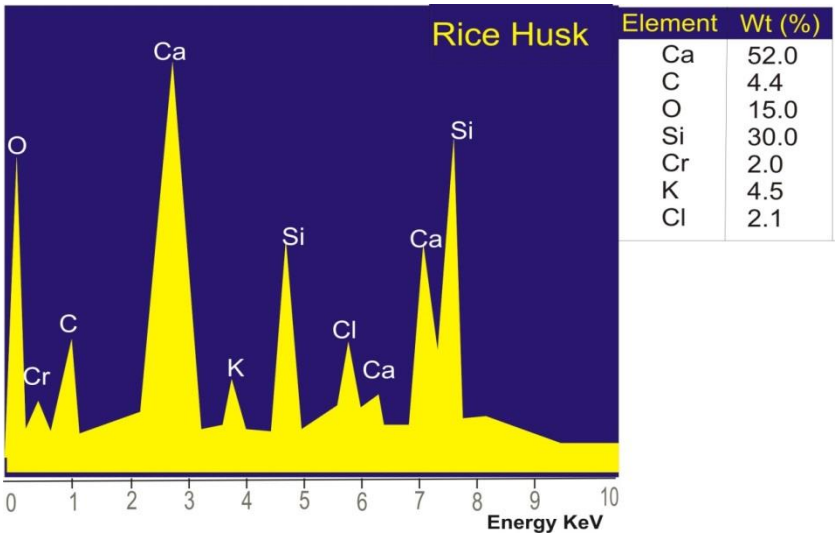

Figure 6: EDX Analysis Showing Chemical Characterisation of the Rice Husk Charcoal

4. CONCLUSIONS

All the three filter materials (Activated Charcoal, Sawdust Charcoal and Rice Husk Charcoal) selected possess larger proportion of Silica and Carbon, and they also possess more pores which are typical features of an adsorbent. Silica and Carbon are regarded as natural materials used for water filtration [11]; hence the selected materials are good adsorbents in water or waste water treatment.

DOI: https://doi.org/10.14232/analecta.2020.2.19-25

REFERENCES

[1] Collins Dictionary, Adsorbents, Retrieved from: https://www.collinsdictionary.com/dictionary/english/adsorbent 2019.
[2] Separation Processes, Adsorbents, Retrieved from: http://www.separationprocesses.com/Adsorption/AD_Chp01a.htm 2019.
[3] S. A. Azeem, Development of New Sorbents for Removal of Contaminants from Water, Retrieved from: http://www.suswatec.de/download/presentations/Abdelazeem.pdf 2013.
[4] F. J. De Silva, Exploring the Multifunctional Nature of Activated Carbon Filtration, A Publication of Water Quality Products, Retrieved from: htttps://www.waterqp.com 2000.
[5] Minnesota Pollution Control Agency, Granular Activated Carbon Filters, A Publication of Minnesota Pollution Control Agency, Retrieved from: https://www.pca.state.mn.us/sites/default/files/c-s1-05.pdf 2009.
[6] G. J. McDougall, The Physical Nature and Manufacture of Activated Carbon, Journal of the South African Institute of Mining and Metallurgy, 91 (4), 1991, pp. 109-120.
[7] J. Kearns, Charcoal Filtration Basics, A Publication of Aqueous Solutions Drinking Water Systems, Retrieved from: http://www.aqsolutions.org/resources/Charcoal_Filtration.pdf 2007.
[8] Z. Al-Qodah, R. Shawabkah, Production and Characterization of Granular Activated Carbon from Activated Sludge, Brazilian Journal of Chemical Engineering, 26 (1), 2009, pp. 127 – 136.
[9] B. Kakoi, J. W. Kaluli, G. Thumbi, A. Gachanja, Performance of Activated Carbon prepared from Sawdust as an Adsorbent for Endosulfan Pesticide, Journal of Sustainable Research in Engineering, 2 (1), 2015, pp. 1-10.
[10] M. K. Lam, R. Zakaria, Production of Activated Carbon from Sawdust using Fluidized Bed Reactor, International Conference on Environment, Retrieved from: http://www.eprints.usm.my/13227/1/production_of_activated.pdf 2008.
[11] J. Duvauchelle, Natural Materials Used for Water Filtration, Retrieved from: https://www.livestrong.com/article/165592-natural-materials-used-for-water-filtration/ 2019.

DOI: https://doi.org/10.14232/analecta.2020.2.19-25

Analecta Technica Szegedinensia
Vol. 14, No. 2 ISSN 2064-7964 2020

SUSTAINABLE FOOD CONSUMPTION INTENTIONS RELATED TO FOOD SAFETY AMONG YOUNG ADULTS

Ildiko Kovacs
Budapest Business School University of Applied Sciences, Diósy Lajos str. 22-24. 1165 Budapest, Hungary

Received: September 14, 2020 • Accepted: November 30, 2020

ABSTRACT

A long-term sustainability of food consumption is in the mainstream of the current trends in the production and consumption patterns of food. A growing number of analyses question this issue nowadays. Despite several papers investigating the profile of sustainable consumers, understanding of the determinants of consumer decision-making and intention towards sustainable food consumption needed further investigation. This study investigates determinants of sustainable food and food safety on consumer behaviour among young customers in Hungary. The objective of this paper is to explore the intention factors of food safety based on sustainable consumption patterns. To gain a better insight in sustainable consumption patterns, the research process was quantitative in nature.

Keywords: sustainable food, food safety, quantitative study, young customers

1. INTRODUCTION

Sustainable development and sustainable consumption have been studied in the last decades in various fields, such as marketing. The theoretical background of the consumer aspect of sustainable development for the current research is based on the Europe 2020 Strategy – A resource-efficient Europe, which calls for finding „new ways to reduce inputs, minimise waste, improve management of resource stocks, change consumption patterns, optimise production processes, management and business methods, and improve logistics" [1]. The Europe 2020 Strategy stresses that our natural resource base is being eroded by growing consumption amounts and the inflexibility of consumption patterns.

There are factors which makes the patterns difficult to change, the average Western diet with high intakes of meat, fat and sugar has a significant effect on social systems and the environmental life support systems as well [2]. On global demand, the energy and the food sector are priority areas and are highlighted for taking measures such as more sustainable production and consumption of food and reduction of food waste. The amount of waste throughout the whole food supply chain would be aimed such as the change of consumption patterns [1].

According to the European Sustainable Consumption and Production Policies, The Sustainable Consumption and Production Action Plan [3] „food production systems compromise the capacity of Earth to produce food in the future. Globally, and in many regions including Europe, food production is exceeding environmental limits or is close to doing so".

What exactly do we mean by 'sustainable' food? As it is defined in the EIPRO (Environmental Impact of Products) report, has a less negative effect on the environment and society: „food we produce and consume has a significant impact on the environment through, for example, greenhouse gas emissions, the use of land and water resources, pollution, depletion of phosphorus, and the impact of chemical products such as herbicides and pesticides." [4]

The Global Food Security Index 2019 [5], Hungary ranks 30th in the GFSI ranking of 113 countries with 72.8 points. It ranks 31st in terms of food affordability, 29th in terms of availability, and 33rd in terms of quality and food safety in the global rankings. Hungary scored a maximum of 100 points in the following areas: Presence and quality of food safety net programmes; Access to financing for farmers, food safety. Other strengths are: Proportion of population under global poverty line (99.3); Change in average food costs (98.7); Urban absorption capacity (95.1); Food loss (93.5); Dietary diversity (86.2); Agricultural import tariffs (81.1).

There were former studies aiming to explore the intention factors of sustainable food consumption, which found environmentally conscious food consumption as the most relevant factor [6],[8],[9], [10]. The

DOI: https://doi.org/10.14232/analecta.2020.2.26-34

present study attempts to find out if consumers actually do modify their food preferences, the factors that push consumers towards this modification, how consumers overcome their consumption habits.

2. MATERIALS AND METHODS

The research focuses on the principles of sustainable food consumption related to food safety. A quantitative online survey was used for data collection through self-administered questionnaires. The questionnaire consisted of several multi-item structure measurement on five-point scales and open-ended questions. The questionnaire included three qualitative questions on conscious purchasing behaviour, Top-of-mind sources of sustainable food and food types which are considered to be the most important in connection with sustainability. All scales to measure the study variables were adapted from former studies [8].

The data were collected between March 2019 and May 2019, a purposive sampling along with snowball sampling was applied and quota method was applied to ensure the appropriate rate of socio-demographic characteristics of the sample. The sampling strategy employed in this research was designed to obtain a sample based on the following criteria: the first criterion was demographic status of the respondents. All respondents in the sample were filtered by the age group 18–25. The second criterion was a purchasing one: the respondents had to be active in food purchasing; had to take part in at least 60 percent of the household food purchase. A sample of 1608 adult's socio-demographic characteristics are presented in Table 1.

Table 1. The socio-demographic characteristics of the sample and the Hungarian population according to the data of the Hungarian Central Statistical Office

	HCSO			Sample		
	Male	Female	Total	Male	Female	Total
Budapest	28.33	28.38	56.71	32.24	32.88	65.12
Pest county towns	15.27	14.40	29.66	13.20	13.46	26.66
Pest county villages	7.13	6.50	13.63	4.07	4.15	8.22
Total	50.73	49.27	100.00	49.51	50.49	100.00

Source: Hungarian Central Statistical Office (HCSO), current research 2020

3. RESULTS AND DISCUSSION

The overall objective of the study was to explore the most relevant factors of sustainable food consumption based on a former qualitative study and the validation of the scale. The structure of food safety was predicted to be multi-dimensional. A twenty-five item five-point Likert-scale (1 – "completely disagree"; 5 – "completely agree") was developed for measuring consumption intention. In the research, the validity test of the scale Cronbach's Alpha test was conducted. The value of Cronbach's Alpha was 0.797, while the Cronbach's Alpha Based on Standardized Items was 0.801. The summary item mean was 3.12. (Minimum: 1.763, Maximum: 4.646 Range: 2.883 Maximum/Minimum: 2.636, Variance: 0.531, N of Items: 25)
Descriptive and inferential statistics were used in the data analysis. The descriptive statistics of the research variables were based on a five-point Likert scale. The results highlighted the most relevant variables in case of risk avoidance: "I avoid purchasing illegal or too unexpensive food", "I purchase grocery products in the same grocery store", "I get more and more information about food (doctors, dieticians, magazines, internet)", "I better prepare and organize my purchases", "I prefer Hungarian food over foreign ones", "I trust the inspections of the Hungarian plant protection and veterinary authorities" and "I am confident in

DOI: https://doi.org/10.14232/analecta.2020.2.26-34

the food risk reduction activities of food control authorities". Table 2 presents the descriptive statistics of the research variables, including medians, modes, means, standard deviations.

Table 2. Descriptive statistics of the determinants

Scale items	Median	Mode	Mean	Std. Deviation
I avoid purchasing illegal or too unexpensive food.	4.60	5.00	5.00	1.93
I purchase grocery products in the same grocery store.	5.00	5.00	4.60	1.35
I get more and more information about food (doctors, dieticians, magazines, internet).	4.00	4.00	3.41	1.27
I better prepare and organize my purchases.	4.00	4.00	3.79	1.31
I prefer Hungarian food over foreign ones.	4.00	5.00	3.73	1.64
I trust the inspections of the Hungarian plant protection and veterinary authorities.	4.00	4.00	3.69	1.63
I am confident in the food risk reduction activities of food control authorities.	4.00	4.00	3.56	1.65
I regularly read blogs and forums about healthy diet.	3.00	3.00	2.66	1.19
I change my food consumption habits.	3.00	3.00	3.28	1.25
I read the product characteristics and labels on the product package.	3.00	4.00	3.39	1.32
I buy branded food.	3.00	4.00	3.27	1.43
I buy food with Protected Designations of Origin and Protected Geographical Indications.	3.00	3.00	2.86	1.73
I buy and consume seasonal food.	3.00	3.00	3.37	1.28
I prefer products that are not produced on a large scale.	3.00	3.00	3.20	1.36
I prefer food made with traditional technology.	3.00	3.00	3.51	2.07
I trust the product identification and tracking system of the food chain (producer, processor, and trader).	3.00	3.00	3.53	1.67
I am confident in the authorities' rapid and effective food recall system (rapid alert system,	3.00	4.00	3.42	1.41

DOI: https://doi.org/10.14232/analecta.2020.2.26-34

withdrawal from the market, destruction).				
I search for information on brands' websites.	2.00	1.00	2.15	1.09
I follow your favourite brand in the social media news (FB, Instagram).	2.00	1.00	2.14	1.10
I purchase products directly from producers.	2.00	1.00	2.34	1.33
I purchase organic products.	2.00	2.00	2.21	1.31
I buy from local producers and processors, not shipped remotely.	2.00	2.00	2.70	1.40
I prefer food that requires low water consumption.	2.00	1.00	2.71	2.08
I prefer food that requires low carbon production.	2.00	1.00	2.78	2.18
I buy locally from the producer.	1.00	1.00	1.93	1.30

Five-point Likert-scale (1 – "completely disagree"; 5 – "completely agree"), n=1605

The less certain intention is buying from local producers, and the following possibilities: searching for information on websites or on social media channels, purchasing organic products, and purchasing local food. The most frequent answers were completely disagreed with: "I search for information on brands' websites" (78 percent disagree or strongly disagree), "I follow your favourite brand in the social media news (FB, Instagram)" (67 percent disagree or strongly disagree), "I purchase products directly from producers" (67 percent disagree or strongly disagree, 13.2 percent agree or completely agree), "I prefer food that requires low water consumption" (58.3 percent disagree or strongly disagree, 12.7 percent agree or completely agree), "I prefer food that requires low carbon production (58.2 percent disagree or strongly disagree, 14.5 percent agree or completely agree). In terms of other variables, the answer range was higher, and mean shows higher diversity.

Based on the 25 statements, a factor analysis using a principal component technique was applied to identify food purchase intention patterns related to sustainable food consumption. To verify the suitability of the 25 food groups for the factor analysis, communalities were calculated for the scale items. Communality values were between 0.616 and 0.919.

Factor analysis was applied to examine the food safety patterns in terms of sustainable food consumption related to food safety. Exploratory factor analysis (principal component analysis with Promax and Varimax rotation) confirmed the final structure. (KMO–0.746, Bartlett's Test of Sphericity Approx. Chi-Square 19069.244, df 300, Sig. 0.000; factors accounted for 67.935% of variability of the overall original 25 scale items. A total variance Explained was 67.78%.

Cronbach's alpha coeffcients showed a high or satisfactory level of reliability. The items of all scales along with means and standard deviations are reported in Table 2.

DOI: https://doi.org/10.14232/analecta.2020.2.26-34

Table 3. Measurement quality parameters of scales for determinants of food safety

Factor	Cronbach's Alpha
1 Trust in authorities' measurements	0.904
2 Health consciousness	0.702
3 Purchasing local products	0.795
4 Environmentally responsible production	0.868
5 Purchasing form local producers	0.902
6 Brand consciousness	0.882
7 Information search on the Internet	0.720

The final exploratory factor analysis of the 25 variables resulted in 7 factors. Results of an exploratory factor analysis (principal component analysis with Varimax rotation) confirmed the unidimensional structure and internal consistency of each scale. Internal consistency of sub-scales and the overall scale was tested and Cronbach's alpha coefficients showed high levels of reliability in all the factors (see Table 3).
The seven factors: trust in authorities' measurements, health consciousness, purchasing local products, environmentally responsible production, purchasing form local producers, brand consciousness, information search on the Internet are based on the 25 scale items, and all fit to the factor structure.

Table 4. Factor structure matrix

Item	Factor	Factor value
I trust the product identification and tracking system of the food chain (producer, processor, and trader).	**F1**	**0.927**
I trust the inspections of the Hungarian plant protection and veterinary authorities.	**F1**	**0.915**
I am confident in the food risk reduction activities of food control authorities.	**F1**	**0.858**
I am confident in the authorities' rapid and effective food recall system (rapid alert system, withdrawal from the market, destruction).	**F1**	**0.821**
I get more and more information about food (doctors, dieticians, magazines, internet).	**F2**	**0.786**
I regularly read blogs and forums about healthy diet.	**F2**	**0.761**
I read the product characteristics and labels on the product package.	**F2**	**0.757**
I change my food consumption habits.	**F2**	**0.749**
I buy and consume seasonal food.	**F3**	**0.795**
I prefer Hungarian food over foreign ones.	**F3**	**0.747**
I buy from local producers and processors, not shipped remotely.	**F3**	**0.732**
I prefer products that are not produced on a large scale.	**F3**	**0.677**
I prefer food that requires low carbon production.	**F4**	**0.956**
I prefer food that requires low water consumption.	**F4**	**0.941**
I prefer food made with traditional technology.	**F4**	**0.791**
I purchase products directly from producers.	**F5**	**0.876**
I buy locally from the producer.	**F5**	**0.749**
I purchase organic products.	**F5**	**0.642**
I buy food with Protected Designations of Origin and Protected Geographical Indications.	**F5**	**0.485**
I purchase grocery products in the same grocery store.	**F6**	**0.810**
I avoid purchasing illegal or too inexpensive food.	**F6**	**0.668**
I better prepare and organize my purchases.	**F6**	**0.562**
I buy branded food.	**F6**	**0.496**
I follow your favourite brand in the social media news (FB, Instagram).	**F7**	**0.864**
I search for information on brands' websites.	**F7**	**0.766**

DOI: https://doi.org/10.14232/analecta.2020.2.26-34

Extraction Method: Principal Component Analysis. Rotation Method: Promax with Kaiser Normalization.

The "trust in the authorities' measurements" factor is the most relevant one forming the factor structure. The items of that factor are visualized on Figure 1. More than half of the respondents reported that they agree or completely agree with the statements, yet 20 percent gave neutral answers. Concerning "I trust the product identification and tracking system of the food chain (producer, processor, and trader)" the neutral answers' frequency was 28.7 percent and the answers "agree" or "completely agree" were around 40 percent.

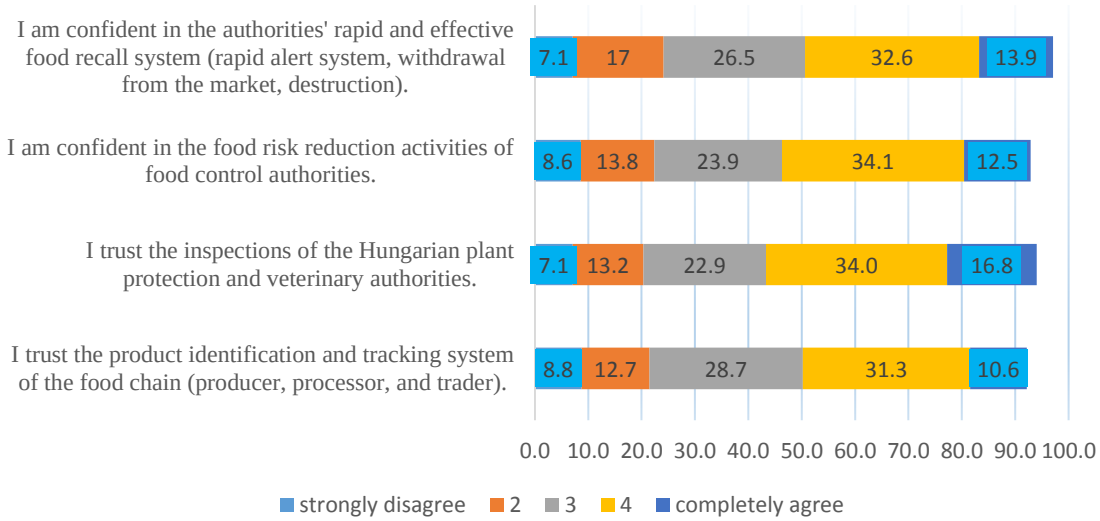

Figure 1. Trust in the authorities' measurements factor – item frequencies in percent

The seven factor components' (n=1608) value was examined in total the sample and two segments: "high sustainable consumption consciousness" versus "low sustainable consumption consciousness" segments. The sustainable consciousness was examined through structured questions. The high consciousness was associated with the focus on the importance of purchasing environmentally friendly food and the intention of influencing others (25% in the sample) and strived to purchase environmentally friendly food but not influenced others (33% in the sample).

DOI: https://doi.org/10.14232/analecta.2020.2.26-34

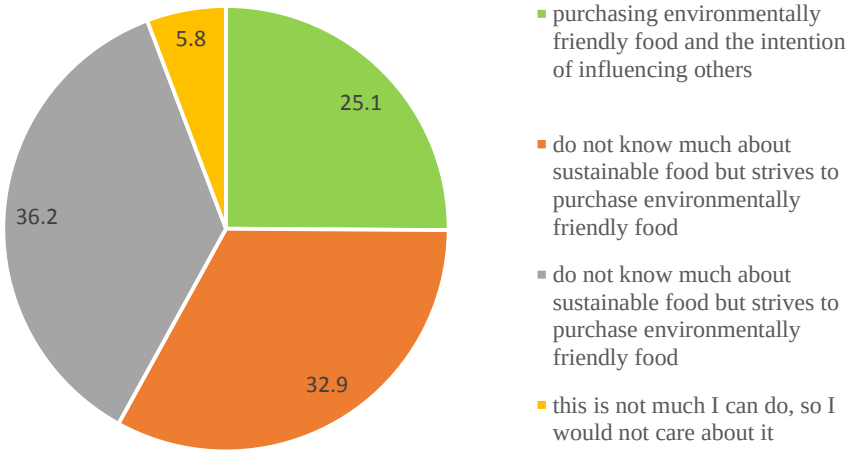

Figure 2. Sustainable conscious food purchase segments - answer frequencies

The low consciousness is associated with the following characteristics: I do not know much about sustainable food but strives to purchase environmentally friendly food (36.2%), this is not much I can do, so I would not care about it. (Figure 2) Another criterion was: the respondents in the low importance of sustainable food consumption segment could not mention relevant environmentally conscious determinant of food purchase, never or rarely purchase environmentally friendly products. For segmentation, open ended and structured questions were used in the questionnaire.

Table 4. The intention in two segments: high and low importance of sustainable food consumption

	Segment 1. High importance of sustainable food consumption	Segment 2. Low importance of sustainable food consumption	Total sample
Trust in authorities	high	high	high
Health consciousness	high	high	high
Local products	average	low	low
Environmentally responsible production	average	low	average
Local producers	low	low	low
Brand consciousness	high	average	average
Search for information on the Internet	average	low	low

DOI: https://doi.org/10.14232/analecta.2020.2.26-34

The factor item values were used to establish categories high, average and low based on sum of scale items' aswers. There are significant differences between the two segments in terms of purchasing local products, searching for information on the brands' environmentally responsible production, brand consciousness and searching for information on the Internet. (Table 4) There are two dominant factors: environmentally resonsible productions and search for information on the Internet which cause the largest difference between the two groups.

4. CONCLUSIONS

The study examined the factors of food safety related to sustainable food consumption, attempting to integrate food safety issues to sustainable food consumption intentions. Food safety have had an even growing importance and would determine the near future as well. In the findings, the identified seven factors in the sustainable food purchase scale was based on former qualitative research. Stimulating sustainable food production, promoting sustainable food consumption and purchasing local food were examined in realation with sustainable consciousness.

The lack of empirical research in the area does not allow making meaningful comparisons with findings of similar former research. However, existing former research that involves sustainable consumption without the structure of consumer engagement showed trust in the authorities, positive intentions to local food and environmental characteristics, and preferring local (Hungarian) food and grocery products. In this exploratory factor analysis, the study identified seven factors that characterized food safety patterns in therms of sustainable food consumption.

Seven factors were identified: trust in authorities' measurements, health consciousness, purchasing local products, environmentally responsible production, purchasing form local producers, brand consciousness, information search on the Internet were identified. There are significant differences between the two segments: high and low importance of sustainable food consumption groups in terms of purchasing local products, searching for information on the brands' environmentally responsible production, brand consciousness and searching for information on the Internet.

The limitation of the study is the regional sample, the respondents live in Pest county or in Budapest. The other limitation comes from the age group covered by the research, therefore the findings may not be generalized.

REFERENCES

[1] EC, The roadmap to a Resource Efficient Europe, https://ec.europa.eu/environment/resource_efficiency/about/roadmap/index_en.htm, (2011), Accessed: 2020. 09. 09.
[2] EC, Sustainable Agriculture, Forestry and Fisheries in the Bioeconomy, https://ec.europa.eu/research/scar/pdf/ki-01-15-295-enn.pdf, (2015), Accessed: 2020. 09. 09.
[3] EC, European Sustainable Consumption and Production Policies, https://ec.europa.eu/environment/eussd/escp_en.htm, (2008), Accessed: 2020. 09. 09.
[4] EC, Environmental Impact of Products (EIPRO), Analysis of the life cycle environmental impacts related to the final consumption of the EU-25, https://ec.europa.eu/environment/ipp/pdf/eipro_report.pdf, (2006), Accessed: 2020. 09. 09.
[5] EIU, The Global Food Security Index, https://foodsecurityindex.eiu.com/Country/Details#Hungary, (2019) Accessed: 2020. 09. 09.
[6] Farzana Quoquab, Jihad Mohammad, Nurain Nisa Sukari A multiple-item scale for measuring "sustainable consumption behaviour" construct: Development and psychometric evaluation, Asia Pacific Journal of Marketing and Logistics, (31) 4 (2019), pp. 791-806.

DOI: https://doi.org/10.14232/analecta.2020.2.26-34

[7] Hungarian Central Statistical Office, Stadat, https://www.ksh.hu/stadat, Accessed: 2020. 09. 09.
[8] Kovacs. I., Lehota, J., Komaromi, N. Analysis of the characteristics of the sustainable food consumption in Hungary. (2016) EMOK XXII. Országos konferencia 2016 Tanulmánykötet : Hitelesség és értékorientáció a marketingben. Debrecen
[9] Piligrimienė, Ž., Žukauskaitė, A., Korzilius, H., Banytė, J., Dovalienė, A., Internal and External Determinants of Consumer Engagement in Sustainable Consumption. Sustainability, 12 (4) (2020), pp. 1349-1369.
[10] ShabbirHusain, R.V., Varshney S., Is Current Way of Promoting Sustainability, Sustainable?, Journal of Nonprofit & Public Sector Marketing, 31(1) (2019) pp. 84-113.

DOI: https://doi.org/10.14232/analecta.2020.2.26-34

Analecta Technica Szegedinensia
Vol. 14, No. 2 ISSN 2064-7964 2020

MATHEMATICAL MODELLING AND EXPERIMNTATION OF SOY WAX PCM SOLAR TANK USING RESPONSE SURFACE METHOD

[1]Rajab Ghabour, [2] Péter Korzenszky

[1] Mechanical Engineering Doctoral School, Szent István University, Gödöllő, Hungary.
e-mail: Ghabour.Rajab@hallgato.uni-szie.hu
[2]Institute of Machinery and Informatics, Faculty of Mechanical Engineering, Szent István University, Gödöllő, Hungary.
e-mail: Korzenszky.Peter@gek.szie.hu

Received: August 4, 2020 • Accepted: September 28, 2020

ABSTRACT

Worldwide, governments tend to reduce the CO_2 emissions, and the storage of the solar energy system is still considered the most challenging problem to solve under the current state. Mainly, in relatively cold countries, as domestic hot water or for heat process services, where the loss in the tank is huge. Any improvement in the design can achieve a higher solar yield. Since water is the usual medium for heat storage, the integration with phase change material (PCM) can store energy when there is abundant energy and release it when it is needed. In this study, we conducted a capsulated PCM soy wax 52°C in an insulated water tank filled with 5 litres of water. To estimate the appropriate number of samples and the quantity of the PCM at two temperature levels using the response surface method with non-linear correlation for the charging phase. The results show 3.16, 0.95, 0.38 first degree magnitude effect for temperature, sample numbers, and wax quantity respectively and 0.29, -0.38 second-degree magnitude effect for quantity and temperature. In addition, an illustration of each two-factors interaction contour plots.

Keywords: solar tank, PCM, energy storage, process heat

1. INTRODUCTION

The human civilisation's fast development and technology revolution in the last few decades brought with it an essential consequence of environment and natural resources over-exploitation. These all drove the researchers to find a better sustainable solution and to optimise the current ones. While fossil fuel is currently the primary source of energy causing a massive amount of carbon dioxide emissions, the environment-friendly solutions, like renewable energy systems, started to appear with long life spans, and high reliability and efficiency [1]. Those systems became an alternative solution to the old ones. The utilisation of the renewable energies is not just because of the conventional fuel CO_2 and being environment friendly, but also because of the continually increasing energy demand and oil price fluctuation. Nowadays, renewable technologies are suitable to supply stable, independent energy for isolated areas. For instance, in Hungary, the desire of supporting the new projects with renewable energy increased because it showed an excellent economic investment with a payback period of less than ten years [2]. Where it became clear that, by using renewable energies, it is the best way to complying with the Kyoto protocol. Even under difficult economic situations, solar heating and cooling proved its place as a driver according to the data published by ESTIF (European solar thermal industry federation) [3]. With more than 37 Mm^2 of a solar power equalling 26.3 GW_{th}.

Agri-Food sector is famous for many problems: high carbon emissions, packaging waste, and food waste[4], with massive consumption of water, land, and considerable environment-friendly growth of the human population worldwide, sustainability is needed urgently in this sector. This means that any small improvement in machines, storage, and energy consumption can lead to a massive saving [5].

Another way of integrating the PCM is the latent heat storage material. Where the chemical bonds of the material break when it changes its phase, they are more commonly used in the solar system as a cooling technology for the PV panels which increases its efficiency. Or it can be used as a storing material [6] to increase the solar system energy capacity in case of thermal collectors. A significant advantage of the integrated PCMs in the solar systems that is easy to mount and has no components' complexity [2]. Adding

*DOI: **https://doi.org/10.14232/analecta.2020.2.35-42***

to high storage density at a small temperature change [7]. Therefore, any research in this direction can lead to an increase in the efficiency of the tank and decrease the size [8], which leads to higher solar system efficiency. Other researchers tried successfully to integrate the PCMs in the solar domestic hot water (SDHW) loop using mono and multi genetic algorithms [9], [10], which is a stochastic optimisation method particularly efficient with discontinuous parameters.

Energy is usually stored and retrieved as sensible heat, latent heat, or thermo-chemical reaction, all through a change in the internal power of the medium. The sensible heat storage (SHS) stores by raising the medium's temperature. While latent heat storage (LHS) utilise the absorbed/released heat when the storage medium changes its phase from solid to liquid, liquid to gas, or vice-versa. The PCM is a latent storage material that absorbs a large amount of heat at an almost constant temperature. This process remains until the whole PCM transferred into the liquid phase. While the surrounding temperature falls, the PCM starts to solidify, which releases the stored latent heat. The usual range of the melting temperature is wide (from -5°C up to 190°C). Within the human comfort zone (20-30°C), some PCMs are very useful, allowing the storage of 5 to 14 times more heat density compared to conventional storage mediums like water or rocks [7], [11].

The numerical model of the whole system is used to choose the adequate operating parameters, and to optimise the stored energy by using a response surface method RSM. The storage system is a critical component and aspect of the solar system. Moreover, to maximise the solar yield, storage density (amount of energy per the volume or mass), the efficiency of the appliances (solar collector, tank, and so forth), and the demand consumption [12], are essential factors to determine the potential of using PCM in the storage tank [13],[14]. This can be useful to satisfy the energy demand because of solar energy's sporadic nature [15]. Where different simulation efforts have been executed to determine the performance of the water storage tanks with PCM [16], but there are no references to model the optimisation of the working variables [8], since it causes 2^k experiments operated differently, where k is the number of the factors.

2. MATERIALS AND METHODS

The system consists of a well-insulated water tank covered by 5 cm of expanded polystyrene (EPS), an insulation material extracted from oil, that works as a perfect insulator in foam form. This foam is an environmentally friendly material that's properties do not change with time. The thermal conductivity is ≈0.033 W/m.K. Tank dimensions are 42x13x16 cm and can store up to 8.7 litres of water as shown in Figure 1a, but during the measurement it was filled with 5 litres and the rest volume was for the specimen tray. The tray has 7x3 specimens, each one can store 50 ml of the assigned material as shown in Figure 2a. After fixing the specimen tray inside the tank and filling it with the assigned material, the heater as in Figure 1b, turns on to a specific desired temperature ranged between (-20 – 100) °C. During the heating process, the by-pass line mixes the water better, which leads to a temperature homogeneity in the tank. In the meanwhile, the data-logger (Almemo 2890-9) with nine input channels as shown in Figure 2b, stores the data coming from the sensors. The sensors are two temperature sensors NiCr-Ni type k (-40 →1000°C) at the right and left side of the tank, and one ambient temperature sensor used as the reference temperature, to identify when the container cools down to near ambient temperature, and another sensor inside the PCM capsule, as well as two heat flux sensors in the internal and external part of the insulation. In the end, the objective is to estimate the time needed for each experiment where the water cools down to a near ambient temperature after heating, that is represented by the following equation:

$$T_{avg\_tank} - T_{amb} \leq +1\ ^{0}C \quad (1)$$

DOI: **https://doi.org/10.14232/analecta.2020.2.35-42**

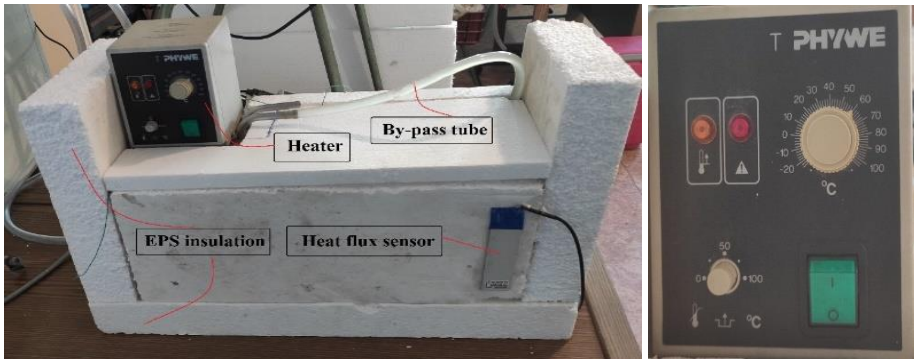

(a) *(b)*

Figure 1.(a) Experiment tank (b) Heater

(a) *(b)*

Figure 2. (a) Capsules tray (b) Data logger

3. RESULTS AND DISCUSSION

The modelling process was created using R-program, with coded values varying between [-1, +1] for each variable and the variables being "S" representing **S**ample numbers where the code -1 is used for four samples and +1 for eight samples. **Q**uantity of the PCM in each sample represented by "Q" where -1 code is 5g and +1 is 10g. Finally, the **T**emperature represented by "T", where code -1 is 30°C and +1 is 40°C. Together this creates a cube pattern, where each corner represents a set of these three variables creating one experiment, as shown in Figure 3. The number of experiments calculated by the form 2^k where k is the number of variables, so 2^3 equals eight measurements, as shown in Table 1. Adding to the fact that the correlation known before starting the measurement is non-linear, another two measurements were conducted out of the cube borders at (S=0, Q=0g, T=30°C) and (S=8, Q=10g, T=60°C) to identify the second-degree non-linear coefficients.

DOI: ***https://doi.org/10.14232/analecta.2020.2.35-42***

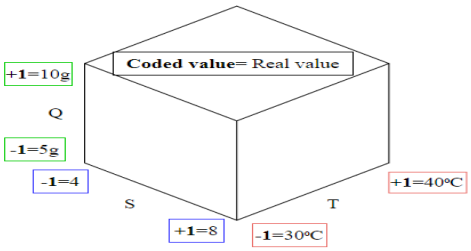

Figure 2. Expirement data set cube

To transfer between coded values and real values the following equations represents the relationship:

$$Coded\ value = \frac{Real\ value - Center\ point}{\frac{1}{2}(range)} \tag{2}$$

Table 1. Experiment parameters and results

	1	2	3	4	5	6	7	8	9_extra _pre	10_extra _post
Samples	-1	+1	-1	+1	-1	+1	-1	+1	-3=0	+1=8
Quantity	-1	-1	+1	+1	-1	-1	+1	+1	-3=0g	+1=10g
Temperature	-1	-1	-1	-1	+1	+1	+1	+1	-1=30^0 C	+5=60^0 C
y [hour]	**4.86**	**6.33**	**5.87**	**7.28**	**10.88**	**13.4**	**11.58**	**13.75**	**4.68**	**17.62**

The applied method is the least-squares method, which attributes to Carl Friedrich Gauss in 1795, that provides the overall rationale for the best fit placement of the line among the studied data points. In our experiment, the non-linear model is solved using iterations. The following coded equation represents the generated model:

$$y = 9.33 + 0.95\boldsymbol{S} + 0.38\boldsymbol{Q} + 3.16\boldsymbol{T} - 0.38\boldsymbol{T^2} + 0.29\boldsymbol{Q^2} \\ -0.05\boldsymbol{S} * \boldsymbol{Q} + 0.23\boldsymbol{S} * \boldsymbol{T} - 0.11\boldsymbol{Q} * \boldsymbol{T} - 0.04\boldsymbol{S} * \boldsymbol{Q} * \boldsymbol{T} \tag{3}$$

To understand the relationship between the factors and the objective, Pareto plot is conducted as in the Figure 4.

DOI: ***https://doi.org/10.14232/analecta.2020.2.35-42***

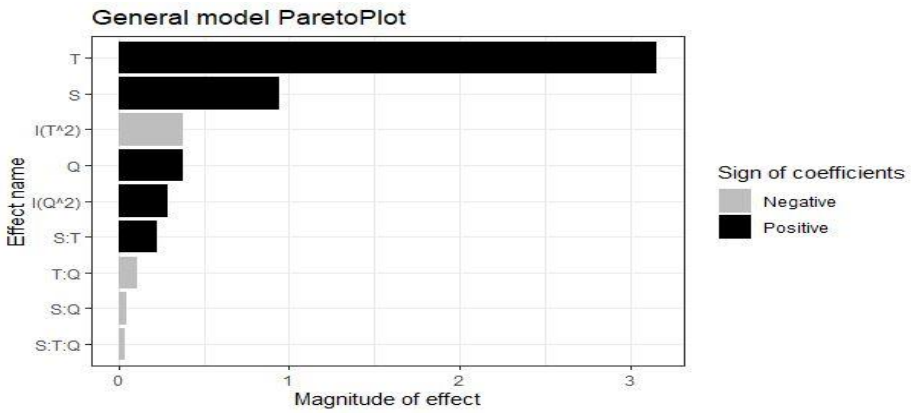

Figure 3. General model Pareto plot

The magnitude of each parameter is easily observed using Pareto plot, while temperature has the biggest positive magnitude, followed by sample numbers. At the third place, contrariwise the second-degree temperature coefficient has a negative magnitude due to the non-linear behaviour. In the end, the quantity first and second degree has a low positive magnitude on the overall result. Adding to the fact that the 3-factor interaction S*Q*T or any three-factor interactions are not existing in nature, but as it is shown in the Pareto plot, it has almost zero magnitude. This is similar to S*Q and Q*T that has a low influence. On the other hand, the contour plot of each two-factor interaction shows the curves where the overall result can be better as seen in Figure 5,6 and 7. Paying attention to some coded values that may have no meaning on the chart, for instance, Q = -3 or S = -3 matches 0g and 0 samples, so below -3 value in the chart has no meaning in real-world values. As we can see in the chart, to increase the time we should increase the samples and the PCM quantity as in the referring arrow. On the other hand, the coefficient of S, Q and T in the equation (3) shows the direction of the plot. In other words, a coded value of $\Delta T \rightarrow [+1]$ will add 3.16 hours to the overall result. Similarly, $\Delta Q \rightarrow [+1]$ will add 0.38 hours and $\Delta S \rightarrow [+1]$ adds 0.95 hours.

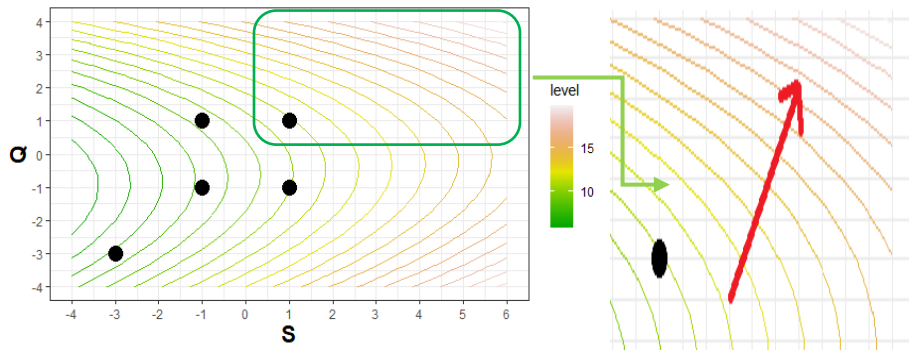

Figure 4. Quantity samples correlation

On the other hand, the T*Q interaction shows better results (as shown in the Figure 6), using more PCM materials and no more than 3.5 coded value temperature equaling 52.5°C which is close to the melting temperature of the PCM. This result is another proof that the melting point of the PCM is around 52.5°C compared to 52°C as mentioned in the material description. The black dots in the graph represents the 4 corners of the cube from 2D Q*T prospective, adding to two pre and post experiments that were needed to

DOI: ***https://doi.org/10.14232/analecta.2020.2.35-42***

identify the second order coefficients. The interpretations of those factors corresponding with the coefficients are 0.38Q, 3.16T, $-0.38T^2$, and $0.29Q^2$.

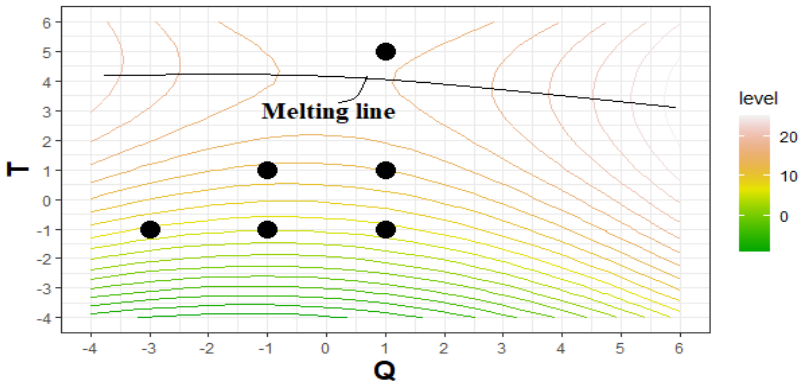

Figure 5. Temperature Quantity correlation

Like T*Q contour, T*S contour has similar results (as in igure 7). They show that at a near-code value of 4, corresponding to 55°C temperature, with extra samples we should obtain better results. The black dots show the cube corners adding to two pre- and post-measurement values from 2D projection.

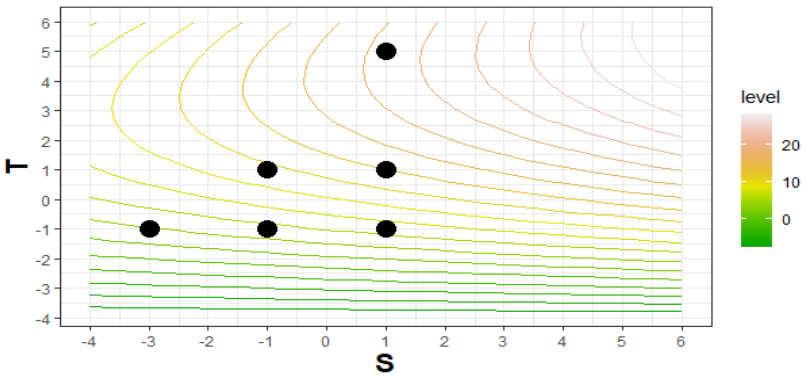

Figure 6. Temperature Samples correlation

4. CONCLUSIONS

This paper presents mathematical modelling of an encapsulated PCM material in a thermal tank, clearly showing that it plays a substantial role in SDHW and heat process systems. We can see significant heat loss in the tank, that takes place in cold countries to a higher extent. The integration with PCMs in the thermal tank used as capsules or insulating layer, will give a better performance and as a result reduce the CO_2 emissions. With this being the biggest concern nowadays and by using PCMs, we can conserve more energy and create better utilisation. In our work, we investigated a matrix set or three variables: Temperature, Quantity, and Sample number of Soy wax 52°C by conducting eight experiments to optimise the performance in a specific thermal tank.

DOI: ***https://doi.org/10.14232/analecta.2020.2.35-42***

Based on the results using R script we generated the mathematical second-degree, non-linear, 3-factors interaction equation. Moreover, to generate the second-order coefficients, two other experiments were needed before and after the set variables. Furthermore, to have a better visualization, Pareto plot illustrates the most influential factors of the non-linear equation, where Temperature has the most significant positive magnitude followed by sample and quantity of PCM. In contrary, the temperature has the most potent negative magnitude, which is proof of the non-linearity.
On the other hand, the contour plot of each 2-factor interaction generated to illustrate the contour lines and the direction of the equation optimization. Easier observation of the curved temperature contour line illustrates the melting temperature of the PCM's. Despite new efforts to generate the modelling and experiments, more research is needed to obtain new models of other cheap and available PCMs like Soy wax 68°C, white beeswax, and Paraffin wax 58°C.

ACKNOWLEDGEMENT

This work was supported by the Stipendium Hungaricum Programme and by the Mechanical Engineering Doctoral School, Szent István University, Gödöllő, Hungary.

REFERENCES

[1] A. J. Gallego et al., "Mathematical modeling of a PCM storage tank in a solar cooling plant," Sol. Energy, vol. 93, pp. 1–10, 2013, doi: 10.1016/j.solener.2013.03.026.
[2] M. Al-ktranee, "overview of the hybrid solar system," vol. 14, no. 1, pp. 100–108, 2020, doi: 10.14232/analecta.2020.1.100-108.
[3] M. Noro, R. M. Lazzarin, and F. Busato, "Solar cooling and heating plants: An energy and economic analysis of liquid sensible vs phase change material (PCM) heat storage," Int. J. Refrig., vol. 39, no. 0, pp. 104–116, 2014, doi: 10.1016/j.ijrefrig.2013.07.022.
[4] R. Ghabour and P. Korzenszky, "Optimal design of solar-assisted industrial processes considering solar energy hybridized with pasteurizer," in Researched Risk Factors of Food Chain, G. Géczi and P. Korzenszky, Eds. Gödöllő, Hungary: Szent István Egyetemi Kiadó, 2018, pp. 93–96.
[5] A. Tolnay, A. Nath, and A. Koris, "CHALLENGES OF SUSTAINABLE FOOD TECHNOLOGY - A REVIEW," vol. 14, no. 1, pp. 118–129, 2020, doi: 10.14232/analecta.2020.1.118-129.
[6] L. F. Cabeza, M. Ibáñez, C. Solé, J. Roca, and M. Nogués, "Experimentation with a water tank including a PCM module," Sol. Energy Mater. Sol. Cells, vol. 90, no. 9, pp. 1273–1282, 2006, doi: 10.1016/j.solmat.2005.08.002.
[7] B. Zalba, J. Marin, L. F. Cabeza, and H. Mehling, Review on thermal energy storage with phase change: materials, heat transfer analysis and applications, vol. 704. 2003.
[8] M. Ibáñez, L. F. Cabeza, C. Solé, J. Roca, and M. Nogués, "Modelization of a water tank including a PCM module," Appl. Therm. Eng., vol. 26, no. 11–12, pp. 1328–1333, 2006, doi: 10.1016/j.applthermaleng.2005.10.022.
[9] D. Haillot, E. Franquet, S. Gibout, and J. P. Bédécarrats, "Optimization of solar DHW system including PCM media," Appl. Energy, vol. 109, pp. 470–475, 2013, doi: 10.1016/j.apenergy.2012.09.062.
[10] R. Padovan and M. Manzan, "Genetic optimization of a PCM enhanced storage tank for Solar Domestic Hot Water Systems," Sol. Energy, vol. 103, pp. 563–573, 2014, doi: 10.1016/j.solener.2013.12.034.
[11] B. Kanimozhi and B. R. R. Bapu, "Experimental study of thermal energy storage in solar system using PCM," Adv. Mater. Res., vol. 433–440, pp. 1027–1032, 2012, doi: 10.4028/www.scientific.net/AMR.433-440.1027.

[12] M. Medrano, M. O. Yilmaz, M. Nogués, I. Martorell, J. Roca, and L. F. Cabeza, "Experimental evaluation of commercial heat exchangers for use as PCM thermal storage systems," Appl. Energy, vol. 86, no. 10, pp. 2047–2055, 2009, doi: 10.1016/j.apenergy.2009.01.014.
[13] J. Deng, S. Furbo, W. Kong, and J. Fan, "Thermal performance assessment and improvement of a solar domestic hot water tank with PCM in the mantle," Energy Build., vol. 172, pp. 10–21, 2018, doi: 10.1016/j.enbuild.2018.04.058.
[14] Víg. P, Seres. I. Application of PCM in food storage, In: Géczi, Gábor; Korzenszky, Péter (szerk.) Researched Risk Factors of Food Chain, Gödöllő, Magyarország : Szent István Egyetemi Kiadó, (2018) pp. 165-168. , 4 p.
[15] L. Moens, D. M. Blake, D. L. Rudnicki, and M. J. Hale, "Advanced thermal storage fluids for solar parabolic trough systems," J. Sol. Energy Eng. Trans. ASME, vol. 125, no. 1, pp. 112–116, 2003, doi: 10.1115/1.1531644.
[16] Bődi. Sz. , Víg. P, Farkas. I. Comparison of water and paraffin for heat storage, MECHANICAL ENGINEERING LETTERS: R AND D: RESEARCH AND DEVELOPMENT 17 pp. 7-13. , 7 p. (2018)

DOI: ***https://doi.org/10.14232/analecta.2020.2.35-42***

Analecta Technica Szegedinensia
Vol. 14, No. 2. ISSN 2064-7964 2020

EXPERIMENTAL INVESTIGATION OF A HIGH EFFICIENCY ELECTRIC HEATER AND DEHUMIDIFIER PROTOTYPE UNIT

[1]Norbert Szaszák, [2]Ákos Pozsa

[1,2]University of Miskolc, Egyetemi út 1., H-3515, Miskolc-Egyetemváros, Hungary,
e-mail: aramszn@uni-miskolc.hu

Received: August 3, 2020 • Accepted: September 4, 2020

ABSTRACT

In this paper the principle of operation and preliminary laboratory measurements of a prototype of a high-efficiency electrical air heater unit is presented. Unlike conventional heaters, which apply Joule-heat formed by electrical resistance, the developed device uses thermoelectric modules for heating ambient air. Just like in case of resistance heaters, most of the heat is produced as a result of the internal ohmic resistance of the thermoelectric module (resistance heating), however, in case of appropriate air conditions our device is capable of transforming the latent heat of the air moisture into heat energy. In case of condensation mode, some of the moisture condensates on the cold side of the module while its latent heat is transferred to the hot side of the module where it heats the dried air. In this mode, the heating efficiency of the device (e.g., the ratio of the heat added to air and the consumed electricity) is over unity. Following the idea and basic equations of the operation of this device, the results of the laboratory measurements in a climate test chamber is presented.

Keywords: latent heat, condensation, thermoelectric-module, heater, air dryer.

1. INTRODUCTION

In many cases electric heating is a cheap and convenient solution where relatively low heating power (up to some kW) is required. Although, the electrical power is relatively expensive compared to another primary energy sources (e.g. district heating, natural gas or firewood), in case of smaller rooms or additional heating the simplicity (consequently its low price) of an electric heater decides in its favour. In addition, most of the electric heaters use ohmic resistance on which the electric current produces Joule-heat: approximately the total amount of the electrical power transforms into heat (the efficiency of the energy conversion is about 100%). The released heating power (P_h) is proportional to the voltage (U) on the heater's resistance (R) and the current (I) flowing through it, or it can be expressed by using quantities of R and I or U and R (see Equation 1):

$$P_h = U \cdot I = I^2 \cdot R = \frac{U^2}{R} \tag{1}$$

As it was mentioned, the smaller electric heaters are mainly used in residential rooms (primarily in bathrooms, kitchens and bedrooms), as an additional heating. Especially, in bathrooms and kitchens, the average level of the humidity is relatively high compared to the other rooms, which means that the air contains a considerable amount of water in form of vapour. It is well known that the evaporation of the water requires a large amount of energy (in the order of $\mathrm{MJ/kg_{H2O}}$). This heat (so-called latent heat as referred later here) can be recovered by condensing a portion of the water vapour out of the humid air.
Our prototype is capable of utilizing the latent heat by condensing a part of the vapour of the humid air by cooling the local air temperature below its dew point (T_{dew}), within the device. The released heat is then applied to heat up the air leaving the unit. In order to cool down the air below its dew point (so that condensation occurs while its relative humidity $\varphi = 1$), so called Peltier thermoelectric modules are used in the prototype. These devices have simple setup: they consist of two parallel electrically insulating plates with high thermal conductivity and among these, several semiconductor elements are placed. Based on the

DOI: https://doi.org/10.14232/analecta.2020.2.43-49

Peltier's effect, heat energy is transferred from one junction to another if different kind of metals or semiconductors are connected and electric current is flowing through the circuit.
Since Peltier modules have internal ohmic resistance (R), they can be used as conventional resistive electric heaters, even if no condensation occurs on theirs colder plates (e.g. the air contains relative low amount of water vapour, thus its dew point is much lower than its temperature). In this operation case the electric heater's heating efficiency (η) is about unity as a conventional electric heater. If the device operates in a room with considerable humidity (i.e. its dew point is not so far below its temperature), condensation occurs on the colder side of the Peltier modules. Therefore, latent heat can be pumped to the hot side of the Peltier modules where it increases the temperature of the leaving, heated air. In this case, besides that the released Joule-heat increases the temperature of the air, the latent heat raises even further its temperature. Since the total energy input is the electrical power only, in case of condensation, the heating efficiency is greater than unity, $\eta > 1$.
The schematic diagram of the energy flow can be observed on Fig. 1.

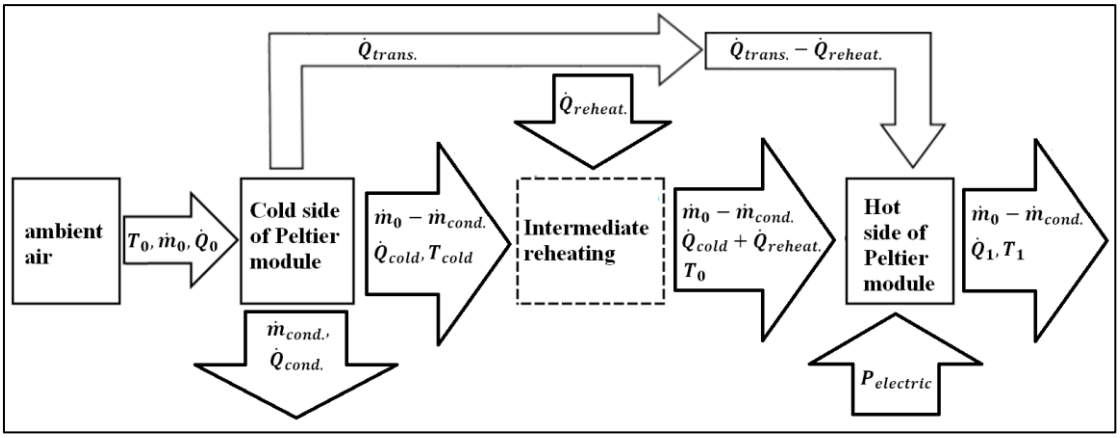

Figure 1. Schematic diagram of the heat and mass flow through the heating unit

Subscript "0" denotes the condition of the ambient air entering the unit, while subscript "1" corresponds to the leaving, heated (and in certain cases drier) air. T is the temperature, $\dot{m}$ is the mass flow and $\dot{Q}$ denotes the heat flow. Within the heater unit the temperature firstly decreases while condensation may occur ("*cond*" subscript denotes condensate). Following the cooled air gets to the hot side of the Peltier module where its temperature increases. In order to describe the process thermodynamically, an intermediate step is inserted (intermediate reheating, temperature up to T_0). In the next step the overheating of the air takes place, while the remained heat energy from the transferred heat ($\dot{Q}_{trans.}$) and the consumed electric energy of the Peltier module ($P_{electric}$) is added to the heat of the air. Based on these, it was possible to draw basic equations which were applied to perform preliminary calculations about the efficiency of the unit at different working conditions. For the calculations it was necessary to take into account the thermodynamic properties of the wet air entering the unit. The mass flow of the entering air ($\dot{m}_0$, see Equation (2)) is not constant when condensation occurs: the exiting mass flow ($\dot{m}_1$) is less than the incoming amount while the difference is the mass flow of the condensed water (condensate). Hence, for our calculations the constant mass flow of the dry portion of the wet air was used, and our results were presented with respect to the dry air.

$$\dot{m}_0 = \dot{V} \cdot \rho_0 \cdot \frac{1}{1+x_0} \tag{2}$$

DOI: https://doi.org/10.14232/analecta.2020.2.43-49

In Equation (2) $\dot{V}$ is the volume flow rate and ρ_0 is the density of the incoming air, while x_0 is the specific vapour content. The specific enthalpy of the wet air (h_{1+x}) is related to its energy content and it is a function of several quantities, such as the temperature (T), vapour content (x), etc. As Ref. [1] introduces, if the wet air cools down below its dew point (T_{dew}, where $\varphi = 1$), condensation occurs: the value of the specific vapour content decreases while a considerable amount of energy released due to the latent heat of the water. This heat is then pumped by the Peltier module to its hot side where the equipped heat sink transfers the heat to the air. By reheating the air to its initial temperature (and following above this value), one hand a lower relative humidity can be achieved (drier air) and on the other hand, for reheating, the required heat energy is less because of the air's lower vapour content.
Based on the foregoing, our idea, namely the air cooling while condensing a part of its humidity and then the reheating process using the recovered heat together the Peltier module's consumed electrical energy seems to be the key of a high-efficiency, relatively simple heater unit. First of all, detailed preliminary calculations were done in order to find the relations between the efficiency and several parameters (relative humidity, temperature, volumetric flow rate, temperature-difference of the Peltier module, etc.). Ref. [2] contains these calculations and dependence of the efficiency on the temperature and relative humidity. We found that in case of $\varphi_0 = 0.5$ the theoretical efficiency can reach the value of 1.1, while in case of $\varphi_0 = 0.7$ it increases value up to 1.3. Following the calculations, a prototype unit was designed and built. The operation of the unit was then investigated in a climate chamber at different air conditions (several temperature and humidity values were set while the heating performance of the unit was measured).

2. MATERIALS AND METHODS

A small prototype unit was designed which contains two Peltier modules connected in parallel and equipped with cooling fins on both cold and hot sides, a 12 V radial fan with speed-control (type JMC/DATECH DB9733-12HBTL), an Arduino® Uno panel with LCD display, relays, MOSFET transistor and 3 pcs DHT11 type thermocouple combined relative humidity sensors. Ref. [3] gives information about the applied TEC1-12706 type Peltier modules. Since the air was circulated with a radial fan, a case was needed in which the flow is directed in the appropriate way. For this reason, a case for the unit was designed and then 3D printed from ABS plastic. The disassembled prototype unit can be observed on Fig. 2.

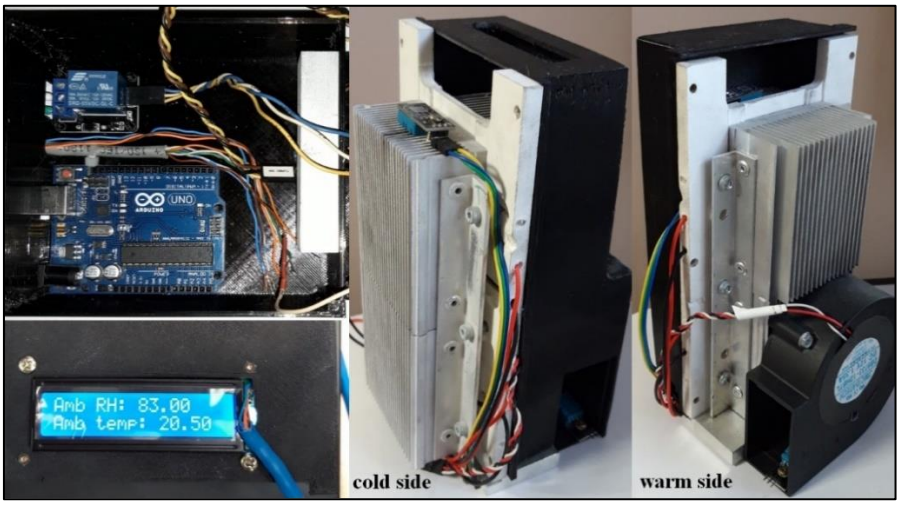

Figure 2. The main components of the heater: Arduino® unit, LCD display, cooling fins on the cold and warm sides of the Peltier modules, radial fan, humidity & temperature sensors.

DOI: https://doi.org/10.14232/analecta.2020.2.43-49

In Ref. [4] the design procedure and the assembly were described in details. The Arduino® Uno unit was necessary in order to the heater operates at the most suitably mode (i.e. with the largest available efficiency). Ref. [2] points out that the heating efficiency depends on several parameters. On the one hand the larger specific quantity of condensate the greater the efficiency is. Based on this, the cooler the cold side of the Peltier module, the higher the efficiency is. Unfortunately, the higher the temperature difference between the two sides of the Peltier module, the lower its efficiency is. This means that more electric power is required to keep a higher value of temperature difference which results lower ratio between the transferred heat and the heat released from the electric power. Because all of these, we kept the temperature difference as low as it was possible in which case condensation still occurred. For this reason, the rotational speed of the radial fan and the power of the Peltier modules were adjusted based on the relative humidity and the required temperature, controlled by a self-made, dedicated program ran on the Arduino® Uno. Ref. [4] contains the detailed construction and operation of the unit. The Peltier modules were controlled in hysteresis mode: theirs cold-side temperature was kept in the range of $(T_{dew} - 3\ °C) \div (T_{dew} - 2\ °C)$, while T_{dew} was determined using the measured parameters T_0 and φ_0 and an empirical equation based on [1]. The temperature difference of the cold and hot sides of the Peltier modules was kept within the range of $15°C \leq \Delta T \leq 20°C$ while the voltage was set to $U = 10.5\ V$ while the current had the value of $I = 4.8\ \mathrm{A/module}$. This operating condition resulted the value of the cooling efficiency of the module in the range of $COP \approx 0.6 \div 0.7$ (estimated based on graphs provided by the manufacturer [3], while the ratio of the current and the maximum allowed current, $I/I_{max} = 0.79$).

The preliminary investigation of the heater was performed in a laboratory climate chamber with air volume capacity of 41.5 m^3, temperature range of $+5\ °C \div +43\ °C$, with accuracy of temperature of $\pm 0{,}5\ °C$. The relative humidity of the chamber is adjustable in the range of $\varphi = 30\% - 95\%$ with accuracy of $\pm 4\ \%$. For the measurements three different nominal values of relative humidity was set: $\varphi = 50\%, 70\%, 90\%$. In case of each humidity setting three different values of nominal air temperature were set: $T_0 = 14°C, 18°C, 22°C$. These resulted nine different parameter settings altogether. Since condensation occurred in the most parameter settings, it was necessary to estimate the releasing latent heat. For this reason, the quantity of the condensed water was measured using a precision laboratory scale.

During the measurements the cooling fins were directed vertically (see Fig. 2) so that the condensate drops could slip into a small pot. To prevent the drops to adhere on the fins, a special super-hydrophobic coating was sprayed on the cooling fins. At each parameter settings, each measurement took adequate long time (one hour) to get enough amount of condensed water that it can be measured with a sufficient degree of accuracy. Furthermore, a certain time was required to get stationary state of the device (i.e. equilibrium temperature of the heat transfer). Following the measurement, by knowing the elapsed time and the mass of the collected water it was possible to calculate the mass flow of the condensed water ($\dot{m}_{cond}$), from which the released heat power ($\dot{Q}_{extra}$) was then calculated using Equation (3):

$$\dot{Q}_{extra} = \dot{m}_{cond} \cdot r_{H2O} + \dot{m}_{cond} \cdot c_w \cdot (T_{dew} - T_{cc}) \tag{3}$$

where

r_{H2O} is the heat of vaporization of water at the temperature of the dew point (T_{dew}),
c_w is the mean specific heat capacity of the water within the range of $T_{dew} \div T_{cc}$,
T_{cc} is the temperature of the cooled condensed water on the cold side of the Peltier module.

Since the temperature of the cold side of the Peltier modules was kept in the range of $2 \div 3\ °C$ below the dew-point temperature, the second product in Equation (3) yields only less than 0.5% extra heat related to the heat released from the phase-change (first product in Equation (3)).

DOI: https://doi.org/10.14232/analecta.2020.2.43-49

3. RESULTS AND DISCUSSION

The measured mass flow of the condensate at different parameter settings can be seen on Fig. 3 a.), while the part b.) shows the extra power due to the condensation.

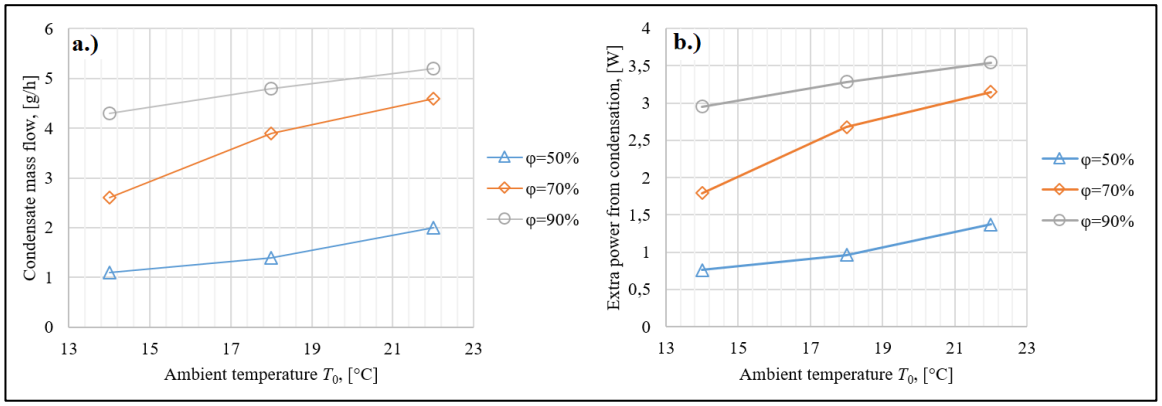

Figure 3. a.) The mass flow of the condensate and b.) the released extra power due to condensation as a function of different air condition (ambient temperature and relative humidity(φ)) settings.

Based on Fig. 3 it can be stated that the mass flow rate of the condensate and hence, the released extra power increases with ambient temperature in all three humidity settings. At a given temperature, higher value of the humidity resulted higher value of mass flow rate of the condensate which means higher released heating power. These all means that the heating efficiency of the developed heating unit increases with both the increasing initial humidity and both with the increasing ambient temperature.

In order to calculate the heating efficiency, monitoring of the electric power demand of the heater unit would have been necessary however, it was not possible to measure such quantity during the measurement. The voltage and the current of the Peltier-module pair were measured as it was mentioned before (with Arduino® module), hence the power consumption of the modules had the value of $P_{electric} = 100.8\,\mathrm{W}$. However, this value changed with time thanks to the switching program ran on the Arduino® unit which controlled the modules in hysteresis mode (i.e. they were switching on and off depending on the temperature). If we suppose that the modules would have operated continuously during all parameter settings, the heating efficiency can be underestimated. Hence, obviously new measurements are required in the future while the electric power demand as a function of the time has to be acquired.

The definition of the heating efficiency of this device is not obvious. On one hand, the efficiency can be defined as the ratio of the useful energy/power and the total introduced energy/power. In case of this device the introduced power is mostly the power of the Peltier modules, however the Arduino® unit and the fan have electric power demand as well from which the power of the Arduino® unit can be omitted. Since it was not possible to measure the power consumption of the fan (moreover its speed was controlled), in our definition the introduced power equals the electric power demand of the Peltier modules ($P_{electric}$). The useful power can be defined as the power which heats the air. This power nearly equals to the sum of the introduced electric power of the Peltier modules and the power yielded from the condensation of the moisture and the heat extracted by cooling the condensate. Following this approach, Equation (4) shows the definition of the efficiency:

$$\eta = \frac{P_{electric} + \dot{Q}_{extra}}{P_{electric}} \tag{4}$$

DOI: https://doi.org/10.14232/analecta.2020.2.43-49

Based on the Equation (4) and supposing constant power demand of the Peltier modules, the efficiency of the unit as a function of the humidity and temperature can be observed on Figure 4.

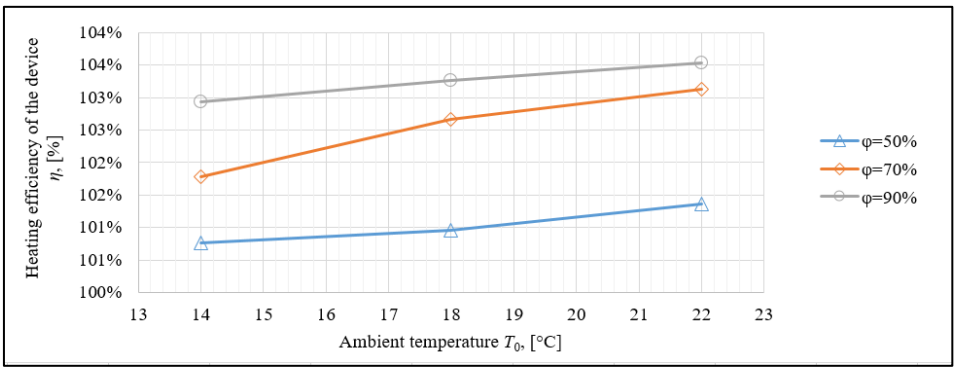

Figure 4. The underestimated heating efficiency of the unit as a function of the relative humidity (φ) and the temperature of the air (T_0).

Based on Fig. 4 it can be noticed that values of efficiency greater than unity were calculated in all measurement cases however, the efficiency was surely underestimated in our calculations. The real efficiency values are supposed to be greater at the corresponding measurement cases: the power demand of the Peltier modules were not constant (duty cycle < 1), the time averaged power should be less than that of was used in Equation (4). Besides this, the real quantity of the condensed water (along with this the released extra power) was slightly greater than that of presented on Figure 3a: some droplets were stuck on the heatsink. Nevertheless, these remarkable values are the result of the heat released from the condensation, since it ensures greater value of the numerator in Equation (4) than the value of the denominator. The efficiency increases both with the initial temperature of the air and it increases with the relative humidity. This phenomenon can be explained by the amount of the condensable vapour per unity air volume, which increases both with the relative humidity and with the temperature as it can be seen on Figure 5.

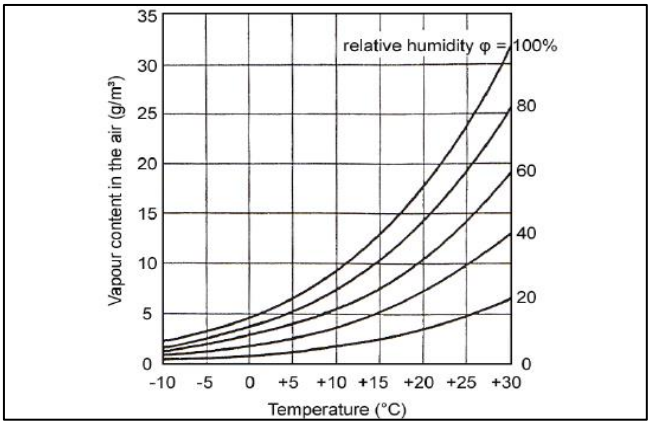

Figure 5. The relationship between temperature, vapour content and relative humidity [5]

Since the developed device utilizes the extra heat released from the condensation, the more condensed vapour per unity time the higher its efficiency is.

DOI: https://doi.org/10.14232/analecta.2020.2.43-49

Unlike the former definition of the heating efficiency, different approach can be introduced, the efficiency can be defined more freely as the ratio of the usefulness and the investment. In our case, the extra heat is not the only yield of the developed device. Another important advantage of this unit is that it reduces the moisture content of the air. Since the water vapour represents a huge amount of energy (i.e. the amount of the heat of vaporisation of the water is significant), at a given temperature the specific enthalpy of the air-vapour mixture can be significantly reduced by reducing its vapour content. This means that by cooling down the air on the cold side of a Peltier module, and in this way by condensing a part of its vapour content, the drier air can be reheated to a higher temperature by introducing the same amount of heat which was extracted on the cold side. Notice that, in spite of the fact that up to this point there was no external heat added to the air medium, its temperature became higher. If extra energy (electrical energy which drives the Peltier modules, released energy from condensation, and the extra energy released by cooling down the condensate) is added to this – drier – air with lower specific enthalpy, its temperature even more increases. In this approach we would get even higher values of efficiency, however this efficiency would require a more complex definition.

4. CONCLUSIONS

It was found that our novel design, heat pump type heater unit can be applied as an air heater with heating efficiency higher than 100%. The results of the performed experiment proved that based on the operating principle (e.g. condensation of the vapour of the ambient air) it is possible to achieve more economical heating compared to the popular resistive, electrical heating technique. Based on the results, - considering the possible achievable higher efficiency - an example for the primary location of the application of this device are wet rooms, e.g. bathrooms, kitchens. Forthcoming experiments will include continuous acquisition of the power demand of the unit for more precise calculation of its efficiency during different operating conditions. Since the efficiency can improve by fine tuning of both the values of the temperature of both the cold and the hot sides of the Peltier modules.

ACKNOWLEDGEMENT

The described article was carried out as part of the EFOP-3.6.1-16-00011 “Younger and Renewing University – Innovative Knowledge City – institutional development of the University of Miskolc aiming at intelligent specialisation” project implemented in the framework of the Szechenyi 2020 program. The realization of this project is supported by the European Union, co-financed by the European Social Fund.

REFERENCES

[1] Buck, Arden L. Boulder, New Equations for Computing Vapour Pressure and Enhancement Factor, Journal of Applied Meteorology and Climatology (1981), ISSN 1527–1532.
[2] Á. Pozsa et al., Hőszivattyús fűtő és páramentesítő készülék tervezése, Jelenkori társadalmi és gazdasági folyamatok, 14(1) (2019), ISSN 1788-7593, pp. 111-121.
[3] Thermonamic, Specification of Thermoelectric Module TEC1-12706. www.thermonamic.com.cn (available: 17 July 2020)
[4] Á. Pozsa, Kondenzációs légfűtő készülék tervezése, megvalósítása és laboratóriumi vizsgálata, MSc. Thesis, University of Miskolc, 2019.
[5] The relationship between temperatures, vapour content and relative humidity. Image. https://www.researchgate.net/figure/The-relationship-between-temperatures-vapour-content-and-relative-humidity_fig1_267236044 (available: 17 July 2020)

Analecta Technica Szegedinensia
Vol. 14, No. 2 ISSN 2064-7964 2020

AUTOMATED BATCH SETTLING COLUMN WITH VIBRATED RODS AND EVALUATION PROTOCOL FOR LIVING WATERS MUD THICKENING

József Faitli

University of Miskolc, Institute of Raw Material Preparation and Environmental Processing, 3515 Miskolc-Egyetemváros, Hungary
e-mail: ejtfaitj@uni-miskolc.hu

Received: August 27, 2020 • Accepted: October 6, 2020

ABSTRACT

Gravity solid-liquid phase separation is applied in minerals industries, waste water treatment, filtration, sewage, drinking water, ocean (water) engineering, dredging, environment and biotechnology. The healthy nation of freshwaters like Lake Balaton and River Bodrog can be maintained by regular mud dredging. The on-water pure mechanical mud thickening would be a really beneficial technology. A new automated batch settling column with vibrated rods had been developed and fundamental tests had been carried out with model materials (glass sand) and muds (Siofok, Tihany, Tokaj). A numerical evaluation protocol with spline interpolation and derivation had been developed by with simple key parameters were determined. Results can be used for the design of a new type of thickener called the rod-lamella thickener.

Keywords: Batch settling test (BST), free - hindered and zone settling, mud thickening, tank - lamella and vibrated rod thickener.

1. INTRODUCTION, AIM AND LITERATURE SUMMARY

Gravity sedimentation is the most common technique applied for solid-liquid separation, and batch settling tests (BSTs) are generally used to obtain detailed information of sedimentation behaviour of suspensions. Before sizing thickeners and clarifiers for many different professional areas BSTs are performed. Different areas can be mentioned, such as minerals industries, waste water treatment, filtration, sewage, drinking water, ocean (water) engineering, dredging, environment and biotechnology [1]. Dredging of the accumulated mud from living waters in Hungary, - especially from Lake Balaton and Rivers Tisza and Bodrog – is really important for keeping the healthy nature of these waters. In the mentioned professional areas, the thickening of suspensions containing very fine particles is often solved by using different chemical or organic additives as flocculants. These are fairly expensive processes and the usage of these materials for mud thickening might cause environmental problems for the nature. Our exclusive aim was the development of pure mechanic equipment and technology by with the hydraulically dredged mud from living waters can be processed on the water on the hydraulic dredging ship. Dredged sand should be separated and carried back to the water and only the thickened mud should be transported out to the bank. If water content of the thickened mud is low enough that even makes some kind of mud utilization to be possible. This paper reports about the preliminary scientific work, done before the development of the rod-lamella thickener. A new automated batch settling column (45 dm^3) was developed. The height of the settling pulp was measured by an optical system. The column was equipped with an interchangeable rod system submerged into the pulp. Rods could be vibrated by a linear motor and this way almost any motion function of different vibrations could be set, depending on the programming of the linear motor. A model material, namely fine glass sand from Fehérvárcsúrgó, Hungary and mud samples from Lake Balaton and River Bodrog were used for sedimentation testing. A numerical evaluation method using National Instruments LabWindows C++ software with the SpInterp spline function was developed. By this software the first (velocity) and second (acceleration) derivatives of the spline smoothed settling curve (height of the settling mud as function of time) and the main technical parameters for thickener design can be determined. Theoretical terminal settling velocity calculations were carried out by methods developed earlier [8, 9, 10]. The aim of the carried out research work was to reveal consequences necessary for the rod-lamella thickener development.

DOI: https://doi.org/10.14232/analecta.2020.2.50-60

In a comprehensive study in 1993 Concha and Barrientos [2] revised the existing gravity thickener design methods. Three types of design methods were listed. Methods based on macroscopic balances (Coe and Clevenger, Mishler), those based on kinematic models (Kynch, Talmage and Fitch, Oltmann, Yoshioka-Hasset, Wilhelm and Naide) and those based on dynamic models (Concha and Bustos, Adorjan, Michaels and Bolger, Robert). According to the macroscopic balances models [3] four discrete zones can be distinguished in industrial thickeners (settling tanks) as well as in batch settling columns. At the top, there is a zone of clarified liquid labelled zone I. If bad thickener operation happens this zone might be turbid because of un-thickened solids, this case is called the thickener overflow. Beneath the clarified liquid is zone II, called the hindered settling zone. Zone II contains pulp of uniform concentration settling at a constant rate. If the concentration is high enough, because of particle – particle interactions, the higher terminal settling velocity particles are not able to settle with this high speed, therefore all the particles are forced to settle together. If there are too many cars in a highway, all the cars must go with the same speed. The situation is similar here. The actual concentration of zone II primarily depends on the solids mass feed rate of the thickener. If the solids feed rate exceeds a maximum the height of zone I bottom is decreasing and the thickener soon starts to overflow. Below zone II a transitional layer, namely zone III might be evaluating. Below zone III the so called compression zone (IV) containing a thick pulp or sediment is situated. The transitional zone (III) does not evolve at all the cases but it separates the above settling zones (region) from the below consolidating zones (region). The solids concentration in the transitional zone sharply increases from the evolved concentration of hindered settling into the much higher concentration of the settled consolidating or compressing solids in zone IV. The concentration in zone IV is further increasing vertically downwards up to the lower discharge point reaching the thickened slurry concentration of the product of the thickener. The kinematic thickener design models are generally based on Kynch's theory about the sedimentation velocity, that at any point in the suspension it is only a function of the local particle concentration. It is evidently valid only in zone II; therefore dynamic design methods had been developed. The consolidation of the sediment under its own weight involves forces not taken into account in the kinematic theory, especially when flocculants are used. Dynamic models take into account compressibility features of the settled solids. Garmsir and Haji Amin Shirazi [1] carried out 300 batch settling tests and compared many equations and methods for the evaluation of tests and for the determination of key parameters for the thickener design. They suggested the calculation of the so called I index determined on the basis of certain parameters of the settling curve for the easy comparison of different settling behaviour of different materials and flocculants. Balbierz and Rucka [4] presented the results of a series of batch settling column tests conducted on sludge from pilot-scale two-stage de-ammonification treatment facility. They compared the well-known settling models and equations of Vesilind, Takacs et al. and Liu et al. for their tests. They concluded that the batch settling tests allowed for a proper characterization of sludge settling properties and the Takacs sedimentation model provided a good prediction of sludge settling behaviour, if the sludge had a flocculent-like nature. Elena Torfs et al. [5] published a practical guide for precise execution of batch settling tests especially for wastewater treatment applications. The usage and determination of the so called stirred specific volume index (SSVI3.5) and the hindered settling velocity were presented. Stirring a sample during settling reduces wall effects, short circuits bridge formation effects, thereby creates conditions more closely related to real sludge behaviour. Lately numerical simulation techniques have arrived on board of this field too. Xu et al. [6] employed the coupled CFD–DEM (Computational Fluid Dynamics – Discrete Element Method) method to simulate the sedimentation process. Such wide range of solid concentration (0.05~0.6 m/m) was simulated. The fluid phase was solved in the CFD program by the locally-averaged incompressible Navier–Stokes equations and particles' motions were tracked in the DEM module based on Newton's second law of motion. The contact force exerted on every particle due to the fluid–particle interactions and collisions between particles and particle-wall collisions during the settling was simulated.

DOI: https://doi.org/10.14232/analecta.2020.2.50-60

2. MATERIALS AND METHODS

2.1. Materials

A model material and real living water muds had been selected for the investigation. The model material should be inert, very fine granular and easily reproducible. The selected material was processed glass sand from Fehérvárcsúrgó, Hungary from a glass mineral mine processing plant. Two dry samples - of about 100 kg each - were taken labelled GS30 and GS75. 30 and 75 indicates the name of product of the processing plant, namely 90 % is smaller than 30 or 75 μm. The removal of the accumulated mud is especially important for the Lake Balaton and the River Bodrog, both are situated in Hungary. Higher quantities of samples (about 600 l thickened suspension from each) had been taken from the north and south part of the Lake Balaton (Tihany and Siófok) and the River Bodrog in Tokaj labelled as Tihany, Siofok and Tokaj samples. After appropriate sample processing many subsamples were produced for fundamental material testing and for later technological investigation. Particle size distribution was measured by wet hand sieving with a standard 400 mm laboratory sieve series above 45 μm and below this size a Horiba LA950-V2 laser particle sizer was used. Figure 1 shows measured particle size – distribution (PSD) curves of the samples.

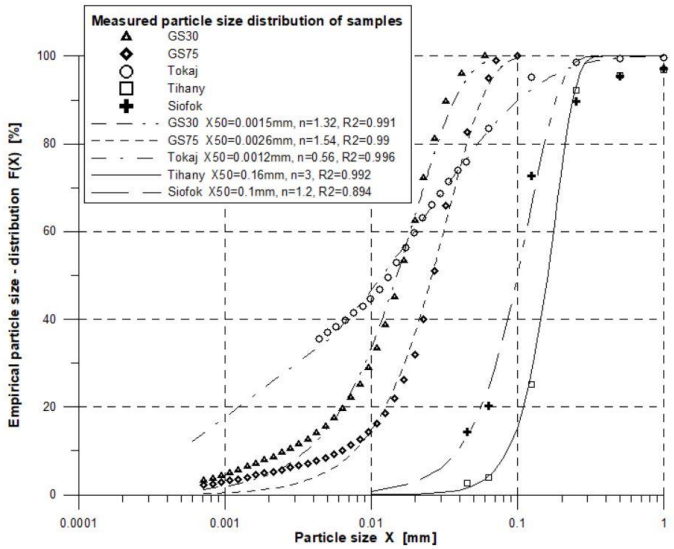

Figure 1. Measured PSD curves of the samples.

The well-known Rosin-Rammler (RR) function: $F(X)=1-\exp\{-\ln 2((X/X50)^n\}$ was curve fitted. Despite of the fact that the Coefficient of Determination (R^2) values are really high and that indicates good fit in a mathematical sense, but clearly visible to the naked eye that the RR curves do not fit well into the very fine and very coarse particle size regions. The Tihany sample had the narrowest (n=3) and the Tokaj sample had the widest (n=0.56) PSD. The Tokaj sample contained the highest amount of fine particles, namely 37 % was still finer than 5 μm. The particle density (ρ_s) was measured in a 500 cm^3 laboratory pycnometer in either denaturised alcohol or distilled water. All tests had been repeated four times; only the averages are shown here. The glass sand samples could be treated as a one-component material; therefore carefully splitted subsamples were tested only. In contrast the particle density of each sieved discrete particle size fraction of the mud samples had been tested. Table 1 shows the measured particle density values.

DOI: https://doi.org/10.14232/analecta.2020.2.50-60

Table 1. The measured particle densities of samples.

GS30	**GS75**	Particle size fraction	**Tokaj**	**Tihany**	**Siofok**
kg/m^3	kg/m^3		kg/m^3	kg/m^3	kg/m^3
2530	2532	0-45 μm	2171	1901	2162
		45-63 μm	2263	2693	2585
		63-125 μm	2442	2662	2607
		125-250 μm	2421	2625	2483
		250-500 μm	2014	2552	2510

The particle density and size distribution of mud samples give some clues about what materials were contained. The finest granular material was the Tokaj sample, and the lower densities of the fine size fractions indicate clay minerals. The intermediate size fractions of the Tihany and Siofok samples were mainly sand, but the measured low particle density values of the fine and coarse size fractions indicate either $CaCO_3$ or some organic materials. Particle shape of each size fraction was tested in an optical microscope (Zeiss AxioCam). Figure 2 shows two characterising photos about the particles.

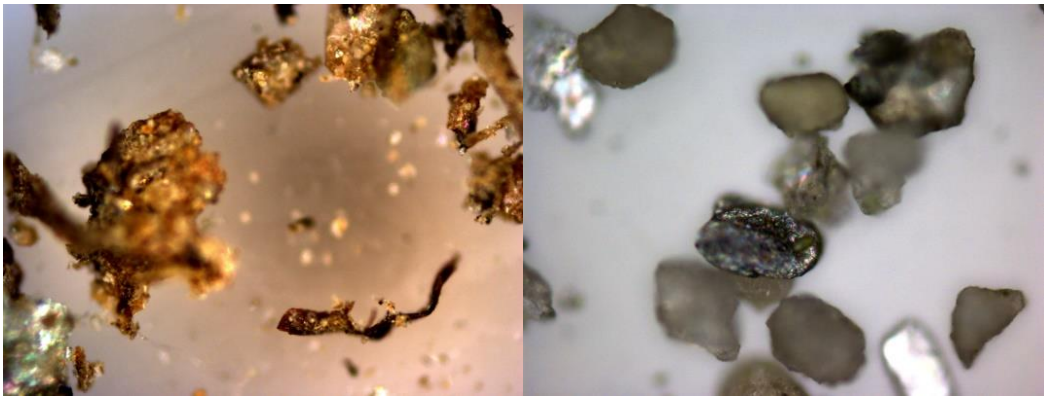

Figure 2. Tokaj sample (left, 100 times magnification) and Siofok sample (right, 200 times magnification).

2.2. Methods

2.2.1. Experimental equipment

A standard plexiglass settling column (height: 33.3 cm, diameter 8.8 cm, volume 2 litres) was used for the preliminary tests. Four 1 cm diameter and 32 cm length rods were mounted on a vibrator and were submerged onto the settling column. The rods could be vibrated by a fixed 50 Hz frequency and the amplitude of the sinusoidal vibration could be set to be 1, 1.2 and 1.4 mm. The applied vibrations are marked V0 (no-vibration), V1 (50 Hz-1 mm), V2 (50 Hz-1.2 mm) and V3 (50 Hz-1.4 mm) here. A new pilot scale automated settling column with vibrated rods had also been developed. Schematic drawing and pictures of it is shown in Figure 3.

DOI: https://doi.org/10.14232/analecta.2020.2.50-60

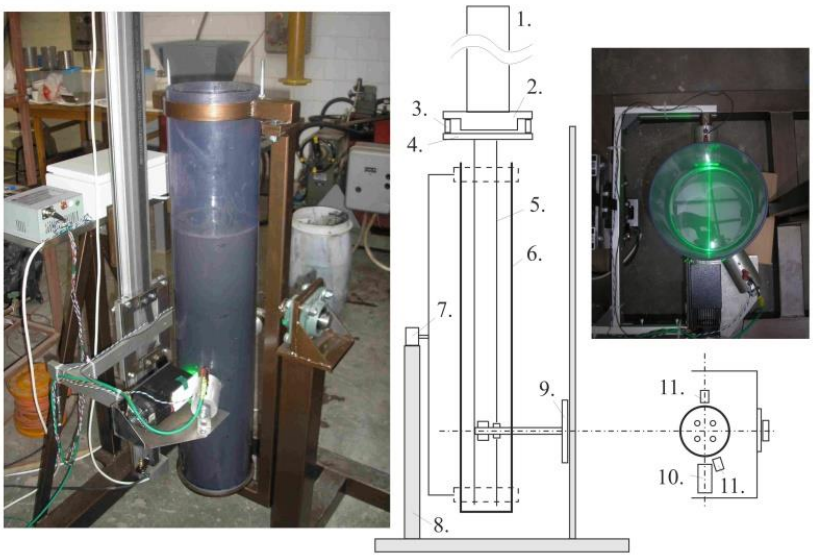

1. Traversing system to uplift the rod structure.
2. Electromagnetic part of the linear motor.
3. Bearing, gap is 0.9 mm.
4. Permanent magnet part of the linear motor.
5. Rod structure.
6. Settling column made by transparent material.
7. Bearing to revolve the settling column.
8. Base frame.
9. Traversing system for the up and down moving of the light sensor.
10. 350 mW laser.
11. Light sensors.

Figure 3. Schematic drawing and photo about the automated settling column.

The settling column was made by transparent plastic material (plexiglass). The diameter of it was 24 cm and the height was 100 cm. Useful volume of it was about 45 l. The manual feed, emptying and mixing in this large size tank compared to normal batch settling columns was difficult, therefore, the tank was mounted on a steel fork and the middle of this fork was mounted on bearing. By this way the tank could be turned around the bearing. To measure the height of the settling pulp and the average solids concentration at a given height an optical system was installed comprising a 350 mW green laser diode and two light sensors. A computer controlled traversing system was also built to move the optical system up and down along the vertical axis of the column. The light sensor installed at the opposite side was calibrated to measure solids volumetric concentration. Unfortunately, at higher concentrations no any light could go through the suspension, therefore this sensor was usable only for lower than about 2 V/V % concentrations. Another light sensor was installed to sense backscattered light. The height of the settling pulp could be exactly measured by this sensor because there was a significant backscattered light intensity drop at moving downward from the clarified zone I into the hindered settling zone II. This pilot scale settling column was equipped with a vibrated rod system comprising a linear motor mounted on another traversing mechanism. Different rods could be mounted onto the moving magnet part of the linear motor and the rods and the linear motor altogether could be lifted up by the traversing mechanism during the feed of the settling column. The resolution of the linear motor was 0.01 μm. Parameters (frequency, amplitude) and the motion function as well of the vibration was just matter of programming of the linear motor to be set. The data acquisition and control software of the automated settling column was written in C++ in LabWindows CVI.

2.2.1. Evaluation protocol

The result of a batch settling test (BST) is the measured H-t (height of the settling pulp versus time) point pairs. Physical parameters of the solids and liquid in the column can also be measured. Csőke et al. [7] applied the curve fitting of the well-known concatenated sections cubic spline function (Equation 1) into the measured H-t points as the first step of the evaluation protocol.

$$y = a_3 \cdot x^3 + a_2 \cdot x^2 + a_1 \cdot x + a_0 \quad (1)$$

DOI: https://doi.org/10.14232/analecta.2020.2.50-60

This numerical mathematical method was replicated here. The evaluation software had been written in National Instruments: LabWindows CVI, C++ language using the "Spline" and "SpInterp" functions. Figures 4 and 5a show some measured settling curves (H/H_0-t) as examples. H_0 is the loaded height and C_0 is the initial volumetric concentration of the suspension in the column. The no-vibration (V0) curves follow the well-known shape and the zones described earlier can be well identified. The interpolated spline function goes through all the measured points. The first (v - velocity) and the second (a - acceleration) derivatives as continuous functions can be calculated as function of the settling time. A quick change of the derivatives (non-smooth function) indicate non-perfect measurement points. By this way the measured results can be checked and corrected. Among others, Figure 5a shows the settling curve of the 0.2 initial volumetric concentration (volume of solids over volume of suspension) no-vibration (V0) Siofok mud. The hindered settling zone, where the H/H_0-t function is linear according to the Kynch kinematic theory can be well seen. Just looking at Figure 5a this function seems to be linear on that zone, but Figure 5b shows its first derivative, namely the velocity of settling or compressing. According to Figure 5b the measured hindered settling velocity (v_H) is not constant here, because the interpolated spline function follows precisely the measured points, and there are always some minor measurement errors. This indicates how powerful this numerical method is. By this spline interpolation technique new points can also be generated. And most importantly this numerical method can be applied for both the kinematic and dynamic thickener models, because derivatives of the complete settling curve can be determined. The volumetric concentration of the pulp (C_z - suspension below the visible boundary layer) can be calculated by Equation 2left, according to the Kynch theory. This concentration is determined by another way and it is called as "dilution".

$$C_z = \frac{H_0 \cdot C_0}{H + v \cdot t} \qquad D = \frac{1 - C_z}{\rho_s \cdot C_z} \qquad S = \rho_s \cdot C_z \cdot v \tag{2}$$

The dilution is the volume of the liquid phase over the mass of the solids phase. The dilution (D) can be calculated by Equation 2middle and the so called solids flux (S) by Equation 2right. Figure 6a shows measured solids flux versus time curves of Siofok mud samples and Figure 6b shows the dilution and the integral of dilution versus time curves of Siofok mud samples. The presented method and the obtained curves can be utilised for later thickener design, however the aim of this study is the investigation of the effect of vibration into settling; therefore, simple characterising numbers were needed. The so called hindered settling velocity was determined as the average velocity of the hindered settling zone (linear range of H/H_0-t). See Figure 5b. The maximum solids flux was determined as the maximal value of the solids flux – time curve. These two values characterise the settling region of BSTs. The compression region was characterised by the volumetric concentration of the settled and compressed solids. This parameter was simply calculated on the basis of the height of the solids on the bottom of the column after a longer time period. Vibration really affected the concentration of the settled solids.

3. RESULTS AND DISCUSSION

Fundamental tests with the selected model material, namely with glass sand were carried out. Figure 4 shows the measured H/H_0-t points and the fitted spline functions of the GS30 samples, when the initial suspension volumetric concentration was set to be 0.1 as an example.

DOI: https://doi.org/10.14232/analecta.2020.2.50-60

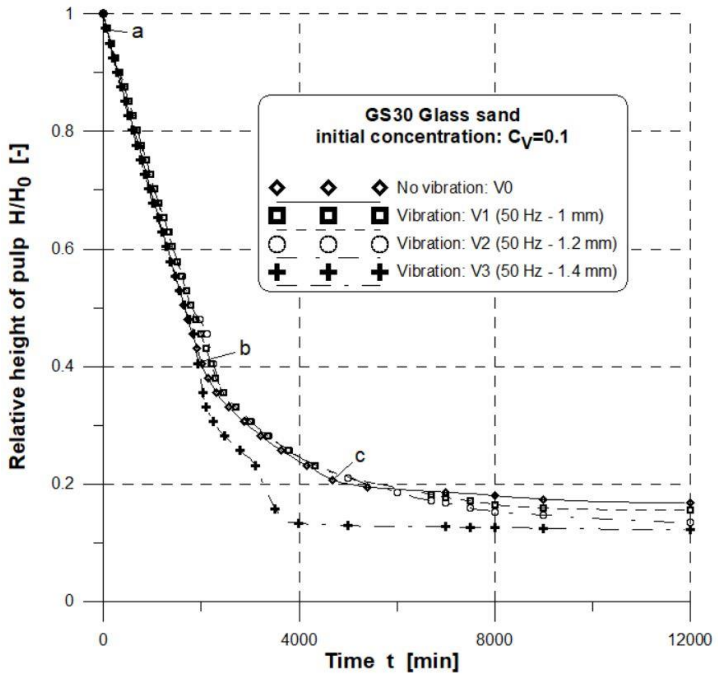

Figure 4. Settling curves of GS30 glass sand as function of vibration.

The no-vibration (V0) settling curve follows the well-known shape described in the literature [5]. After a very short lag phase at point (a) zone (hindered) settling with a constant speed of pulp boundary decreasing starts and then lasts until point (b). The transition phase starts at point (b) when the sludge blanket reaches the transition layer. The last phase called compression starts at point (c). Looking at Figure 4 many conclusions can be drawn about the effect of vibration into settling. First of all the settling curve of the most intense vibration (V3) is significantly different in the compression BST region. It is obvious that granular materials can be compressed by vibration. A mason in the construction industry generally compacts concrete with vibration. The result of the vibration is a much higher solids concentration. On the other hand compaction starts to happen earlier too; therefore the shape of the settling curve is different. It is also interesting that in this case vibration almost does not affect settling speed in the settling BST region. The linear height – time phase (hindered settling phase) of all of the vibration settling curves is clearly visible and there is only a very slight difference on the slope as function of the vibration amplitude. The developed spline smoothing technique can efficiently be used for all the curves because this function goes through all the points and its derivatives show immediately any un-smoothness of them. Table 2 shows the measured settling parameters of the GS30 glass sand sample BSTs.

Table 2. Measured settling parameters of model material (GS30) tests.
(Measured in the standard 8.8 cm diameter plexiglass settling column.)

Sample	Initial volumetric concentration [-]	Vibration	Hindered settling velocity [mm/min]	Maximum solids flux [kg/m^{2}h]	Volumetric concentration of settled solids [-]
GS30	0.1	V0	0.1	1.8	0.61
GS30	0.1	V1	0.095	1.5	0.64
GS30	0.1	V2	0.09	1.6	0.73
GS30	0.1	V3	0.15	1.9	0.81
GS30	0.2	V0	0.025	1.1	0.46

DOI: https://doi.org/10.14232/analecta.2020.2.50-60

GS30	0.2	V1	0.025	1.2	0.6
GS30	0.2	V2	0.027	1.5	0.86
GS30	0.2	V3	0.025	1.2	0.86
GS30	0.3	V0	0.0095	0.9	0.52
GS30	0.3	V1	0.011	1.0	0.55
GS30	0.3	V2	0.014	1.3	0.62
GS30	0.3	V3	0.011	1.1	0.66

The initial concentration does really affect the settling behaviour of the glass sand suspensions. Higher initial concentration results lower hindered settling velocity and lower maximum solids flux. It is obvious because higher concentration results higher rate of hindering among the particles. The hindered settling velocity and maximum solids flux are features of the settling BST region. These values are pretty similar for a given initial concentration independently from the vibration; so data in Table 2 also indicates that for this material vibration almost does not affect settling in the settling BST region. The volumetric concentration of settled solids is the feature used for the characterisation of the compression BST region. Higher vibration amplitude results higher final concentration on the tested range. The maximum final volumetric concentration is 0.86 and that is a really high number. It depends on the particle size and shape distributions of the solids, namely how the vibration can compress the particles. Because of the vibration particles can have better and better orientation; therefore more tight space filling is the result. The free settled volumetric solids concentration is about 0.52 – 0.61 without vibration and vibration can significantly increase it up to 0.86. Table 3 shows the measured settling parameters of the GS75 glass sand sample BSTs.

Table 3. Measured settling parameters of model material (GS75) tests.
(Measured in the standard 8.8 cm diameter plexiglass settling column.)

Sample	Initial volumetric concentration [-]	Vibration	Hindered settling velocity [mm/min]	Maximum solids flux [kg/m^{2}h]	Volumetric concentration of settled solids [-]
GS75	0.1	V0	0.162	3.4	0.54
GS75	0.1	V1	0.145	2.5	0.57
GS75	0.1	V2	0.142	2.9	0.65
GS75	0.1	V3	0.14	3.8	0.75
GS75	0.2	V0	0.06	2.44	0.44
GS75	0.2	V1	0.055	3.5	0.56
GS75	0.2	V2	0.055	4.2	0.7
GS75	0.2	V3	0.055	3.2	0.85
GS75	0.3	V0	0.02	1.4	0.52
GS75	0.3	V1	0.022	2.28	0.56
GS75	0.3	V2	0.023	1.8	0.59
GS75	0.3	V3	0.025	1.5	0.62

The only difference between GS30 and GS75 is the particle size range, GS75 is coarser a little. Therefore the hindered settling velocity and maximum solids flux values are higher but the observed tendencies in the settling BST region are the same. The tendencies are similar in the compression BST region also, final free settling volumetric solids concentration without vibration is about 0.44 – 0.54 and the maximum measured vibrated final volumetric concentration is 0.85.

The effect of vibration on the settling behaviour of real living water muds had also been tested. The settling curves of the Siofok samples are shown on Figures 5 and 6.

DOI: https://doi.org/10.14232/analecta.2020.2.50-60

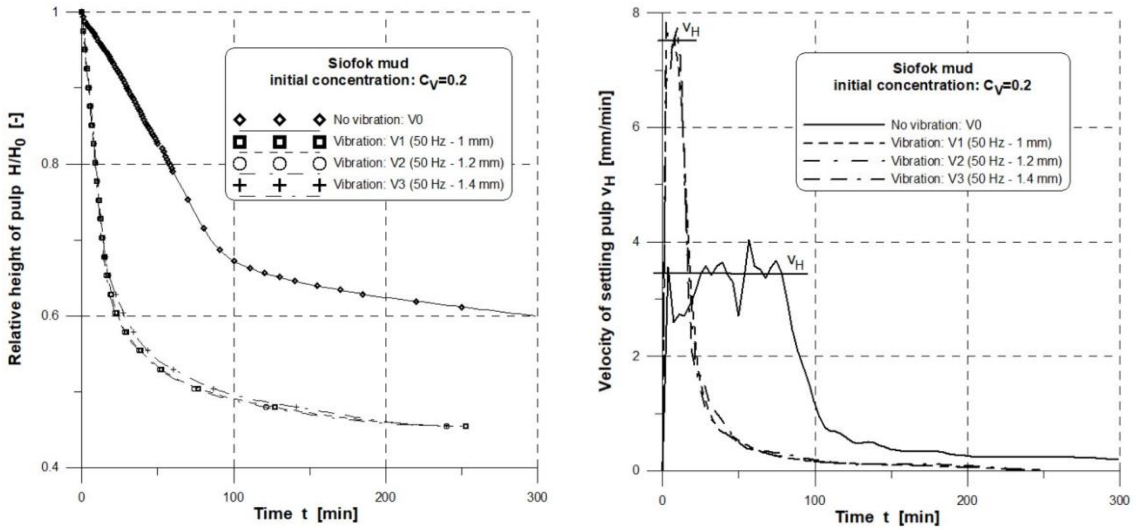

Figure 5. Settling curves of Siofok mud as function of vibration.
Fig. 5a. Relative height of pulp versus time (left), Fig. 5b. Velocity of settling pulp versus time (right).

The no-vibration - Siofok mud - initial volumetric concentration 0.2 BST curve was measured in the 24 cm diameter automated settling column, while the vibrated curves were measured in the 8.8 cm diameter traditional one. Therefore, the visible big difference might be result of the vibration or the size of the column. Unfortunately, there are no more measured data yet, so there is no answer to this question, namely which of them is the reason of this visible big difference. Figure 5b shows how the hindered settling velocity was determined. Because the quantitative value of this velocity will not be used for process engineering design, therefore this value was simply read as the average value of the v-t plot of linear (hindered) settling zone and statistical evaluation has not been performed.

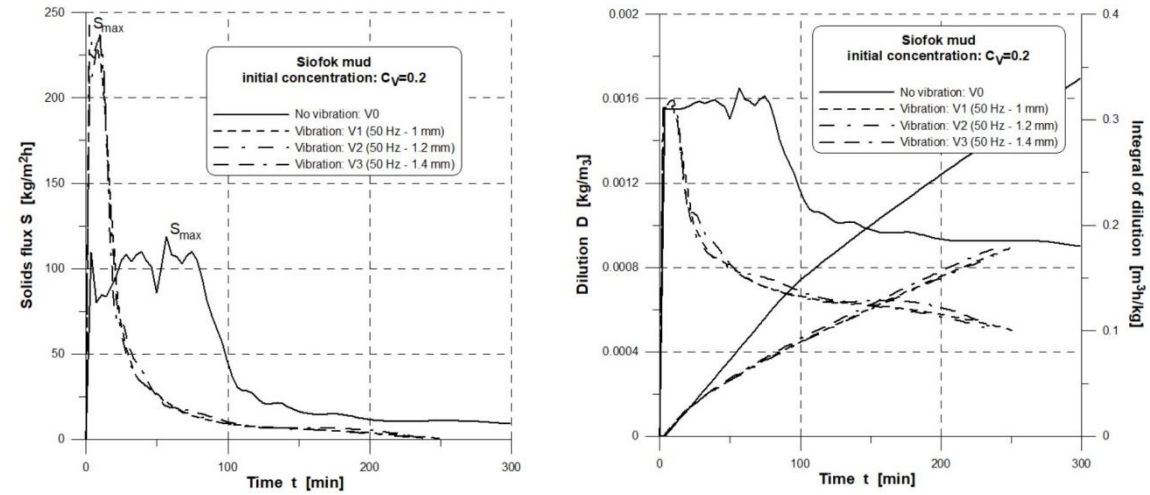

Figure 6. Settling curves of Siofok mud as function of vibration.
Fig. 6a. Solids flux versus time (left), Fig. 6b. Dilution and integral of dilution versus time (right).

DOI: https://doi.org/10.14232/analecta.2020.2.50-60

Table 4 summarises the measured data of living water muds BST tests.

Table 4. Measured settling parameters of mud tests.
(Vibrations were measured in the standard plexiglass settling column, others were measured in the automated settling column.)

Sample	Initial volumetric concentration [-]	Vibration	Hindered settling velocity [mm/min]	Maximum solids flux [kg/m^{2}h]	Volumetric concentration of settled solids [-]
Tokaj	0.1	V0	0.8	9.94	0.189
Tokaj	0.2	V0	0.012	0.43	0.22
Siofok	0.1	V0	14.41	230	0.35
Siofok	0.2	V0	3.5	119	0.38
Siofok	0.2	V1	7.57	232	0.44
Siofok	0.2	V2	7.87	243	0.44
Siofok	0.2	V3	7.73	234	0.44
Siofok	0.3	V0	2.7	116	0.45
Tihany	0.1	V0	11.62	256	0.41
Tihany	0.2	V0	4.3	153	0.39
Tihany	0.3	V0	1.9	91	0.41

Real mud BST data also indicates that vibration slightly affects slurry thickening on the settling region, but it affects thickening very significantly on the compression region. On the settling region particles or particle flocs are still moving downward. Vibration might induce many different effects, and many of them might slow down and many others might speed up the downward particle movement. If vibration is too intensive the result might be mixing instead of thickening. Intense vibration might break down the formed flocs and therefore settling speed of the individual particles will be lower. A moderate amount of energy input might decrease the hydrodynamic drag around the particles and might decrease particle – wall interactions, therefore settling speed might increase. While higher energy input might result in sufficient kinematic energy for the particles to be mixed. The described tests are not suitable to answer these fundamental questions, but consequences can be drawn for the design of a new type of mud thickener. The new thickener should be comprised of two parts. A pre-thickening part is necessary where the settling region of thickening is carried out. The pre-thickening part might be a lamella thickener. The compression of the pre-thickened slurry might be carried out in the second machine part where vibrated rods are used to intensify compression. This is the operating principle of the so-called rod-lamella thickener.

4. CONCLUSIONS

Special batch settling tests had been carried out in a traditional and in the newly developed automated settling columns, where vibrated rods were submerged onto the settling suspension. The developed spline interpolation and derivation test evaluation protocol was proved to be an effective method for both the traditional and the vibrated BSTs. Simple features: the hindered settling velocity, the maximum solids flux and the volumetric concentration of the settled and compressed solids were determined for all the tests. Conclusions can be drawn on the basis of these features. Vibration only slightly affected the thickening in the settling BST region while vibration strongly affected it in the compression BST region. The settling curve of a vibrated BST looks totally different, but the developed spline interpolation technique can be effectively used for the evaluation. Conclusions can be used for the design of the rod-lamella thickener, namely a pre-thickening unit is necessary for the settling region and in the post-thickening unit vibrated rods can be used for the compression.

DOI: https://doi.org/10.14232/analecta.2020.2.50-60

ACKNOWLEDGEMENT

The described article was carried out as part of the "Sustainable Raw Material Management Thematic Network - RING 2017", EFOP-3.6.2-16-2017-00010 project in the framework of the Széchenyi 2020 program. The realisation of these projects is supported by the European Union, co-financed by the European Social Fund.
The research was carried out at the University of Miskolc, within the framework of the Thematic Excellence Program funded by the Ministry of Innovation and Technology of Hungary (Grant Contract reg. nr.: NKFIH-846-8/2019).

REFERENCES

[1] Garmsir M.R. and Haji Amin Shirazi H.: A new approach to define batch settling curves for analyzing the sedimentation characteristics. JOURNAL OF MINING & ENVIRONMENT, Vol.3, No.2, pp. 103-111. (2012)
[2] Concha F., Barrientos A.: A Critical Review of Thickener Design Methods. KONA POWDER AND PARTICLE JOURNAL Vol. 11. pp. 79-104. (1993)
[3] Vesilind P.A.: Design of prototype thickeners from batch settling tests. WATER AND SEWAGE WORKS 115: pp. 302-307. (1968)
[4] Balbierz P. and Rucka K.: Sludge settling characterization for the mathematical modelling of sidestream treatment processes. 9th Conference on Interdisciplinary Problems in Environmental Protection and Engineering EKO-DOK, E3S Web of Conferences 17, 00003 (2017)
[5] Elena Torfs et al.: Experimental Methods In Wastewater Treatment. Edited by van Loosdrecht M.C.M., Nielsen P.H., Lopez-Vazquez C.M. and Brdjanovic D. (eBook) Published by IWA Publishing, London, UK (2016)
[6] Xu, S., Sun, R., Cai, Y. et al.: Study of sedimentation of non-cohesive particles via CFD–DEM simulations. GRANULAR MATTER 20, 4 (2018)
[7] Csőke B., Bőhm J., Antal G., Faitli J.: Számítógéppel támogatott mérési és tervezési eljárás zagysűrítők méretezésére. (Computer aided measurement and design method for slurry thickeners design) GÉP 46: Vol. 2. pp. 34-39. (1994)
[8] Bőhm J., Debreczeni Á., Faitli J., Gombkötő I., Meggyes T.: High-concentration hydraulic transport of tailings. LAND CONTAMINATION AND RECLAMATION 15: 2, pp. 195-217. (2007)
[9] Faitli J., Gombkötő I.: Some technical aspects of the rheological properties of high concentration suspensions to avoid environmental disasters. JOURNAL OF ENVIRONMENTAL ENGINEERING AND LANDSCAPE MANAGEMENT 23: 2, pp. 129-137. (2015)
[10] Faitli J.: Continuity theory and settling model for spheres falling in non-Newtonian one- and two-phase media. INTERNATIONAL JOURNAL OF MINERAL PROCESSING 169: 1, pp. 16-26. (2017)

Analecta Technica Szegedinensia
Vol. 14, No. 2 ISSN 2064-7964 2020

BEHAVIOR OF THE STRUCTURE OF DIFFERENT MATERIALS UNDER STATIC FORCE

[1]Balázs P. Szabó, [1]Zita Zakupszki, [2]Balázs Szabó

[1] University of Szeged, Faculty of Engineering, Department of Food Engineering,
6725 Moszkvai krt. 5-7., Szeged, Hungary
[2] University of Szeged, Faculty of Dentistry, Department of Periodontology,
6720 Tisza Lajos krt. 64., Szeged, Hungary
*e-mail: szpb@mk.u-szeged.hu

Received: August 13, 2020 • Accepted: October 29, 2020

ABSTRACT

The subject of rheology is the study of force-induced deformation and creep in materials, taking into account the effect of time too. The purpose of the measurements is to study time-dependent tension-deformation correlations, which include creep and tension-relaxation parameters, and viscosity. Due to the characteristic structure of biological materials, we try to introduce rheology through different materials. Our samples also include soft, semi-hard and hard materials from fish meat to human teeth. It is very clear from the obtained results that the internal structure of each material is influenced by many factors. These factors also interact with each other and they cannot be standardized in a single study.

Keywords: rheological tests, viscoelastic material, mechanical fracture test

1. INTRODUCTION

Relatively many experiments have been performed in the recent past to understand/evaluate the physical as well as mechanical properties of different materials. These studies included the study of the relationships between load-deformation and tension-relative elongation, the cases of pressure, tensile, shear, bending and hydrostatic compression, supplemented by the studies required for the viscoelastic characterization of materials. During the tests, the status indicators, which are influencing the mechanical properties are included as variables (Sitkei 1981, Mohsenin 1968).

In the study of materials, the correlations between force and deformation are most often examined. The load can be applied with a cylindrical pressure head, a spherical head and a flat slab. It is assumed that the steel load heads can be considered rigid with respect to the examined material, so they do not deform (Rosenthal 1999). The elasticity factor E, the biological pour point, the breaking point and the Poisson's ratio can be determined from the force-deformation correlations. During the measurements, the various status indicators of the material must be accurately recorded.

A striking feature of biological materials is that the correlation of force-deformation also depends on the rate of deformation. This means that the correlation should be sought between three factors rather than between two factors (tension and deformation). Materials where we also have to take into consideration the effect of time are called viscoelastic materials. These substances have the properties of partly solids and partly of liquids (Peleg 1982). For some materials, the relatively small loads result in tension and deformation, which are only dependent from the amount of time, but does not show correlation with the tension. Such materials are called linear viscoelastic materials (Ferry 1980). For many materials, when a significant amount of the deformation caused by loading cannot be recovered during unloading, the tension-deformation correlation depends not only on time, but also on the magnitude of the tension. In this case we speak of non-linear viscoelasticity. For synthetic models that illustrate the theoretical results of rheology, „rheological bodies" embodying the basic forms of mechanical behavior were introduced as basic models: The behavior of elastic materials is comparable to that of a spring, while the properties of fluids are similar to those of damping element. Accordingly, the behavior of viscoelastic materials can be formed by a coupling combination of these two phenomes switches. It can be serial (Maxwell model) and

DOI: https://doi.org/10.14232/analecta.2020.2.61-68

parallel (Kelvin model) (Figure 1). By connecting two rheological bodies in *parallel*, we mean that the deformation of the bodies is the same, and the uptake of the deformation tension is shared by the two bodies according to their resistance. By *serial* connection of the two bodies is meant that the deforming tension acts on both bodies with its total value, and the total deformation of the coupled pair is the sum of the deformations of the two bodies.

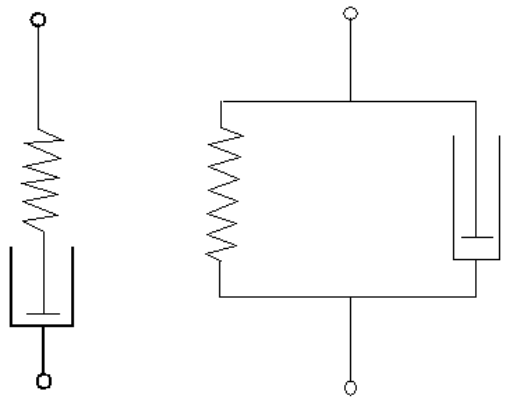

Figure 1. Schemas of the Maxwell model and the Kelvin model

The deformation of a viscous body or Maxwell's body (b) (according to the assumptions of the so-called linear viscosity) is constant under constant tension and increases at a rate proportional to the tension. This is described by the equation below:

$$\frac{d\varepsilon}{dt} = k\sigma \tag{1}$$

where k is a constant characterizing the viscosity of the material.

2. MATERIAL AND METHODS

One of the most important properties of materials is their hardness, which exerts against the penetration of a rigid material. Two groups of processes are known, the classical method, in which the measurement is performed by creating a deformation, and methods based on other physical action. The latter includes, for example, the impact test method or the acoustic stock test.

Classical methods for measuring deformation can be grouped according to the method of inducing the deformation (quasi-static or dynamic methods), the method of measuring the deformation due to external influence (measuring the diameter, which is determining the surface of the print), the indentation depth, and in terms of the design of the measuring instrument. In terms of the design of the measuring device can be a manual, portable or fixed measuring device with a desktop by stand arrangement – simple, with manual or automatic operation with computer (or PLC) control, or automatic evaluation using an image processing method (Steffe 1996).

In our work we present the results of such static measurements. In our studies, we have a number of measurements regarding their hardness, from various foods to human teeth, of which we highlight only a few in the course of this current work.

DOI: https://doi.org/10.14232/analecta.2020.2.61-68

The principle of quasi-static measurement is that during the measurement a hard body (measuring head) of standard material, shape and size is pressed on / into the surface of the material to be measured with load acting for a certain time. The load is slowly increased, which is why the methods are called quasi-static or static hardness measurements. Its schematic drawing is shown in Figure 2.

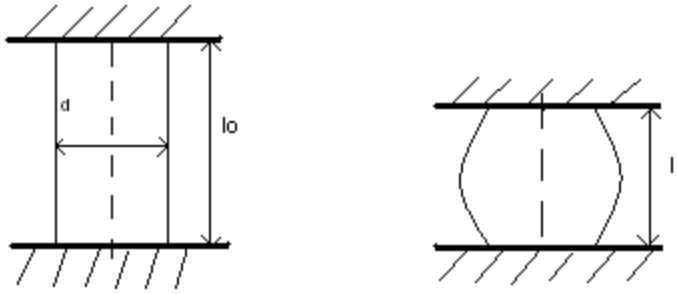

Figure 2. Deformation of samples under load

For most of the tests, the force is usually transmitted by a cylindrical measuring head, which has a circular cross-section. The resulting σ compressive tension can be calculated from the F force and the A surface of the measuring head

$$\sigma = F/A \tag{2}$$

It is advisable to calculate and apply the relative deformation instead of deformation:

$$\varepsilon = \Delta l/l \tag{3}$$

Where: the original size of the raw material tested:
before deformation: l_o
after deformation: l - Δ l

According to Hooke's law, the E modulus of elasticity (Young's modulus of elasticity) establishes a relationship between the above quantities:

$$\sigma = E \cdot \varepsilon \tag{4}$$

Materials that can be described by Hooke's law are called flexible materials. If a load greater that the destruction limit is applied, macroscopic damage is going to occur on that sample.
Our tests were performed with the Lloyd 1000R Material Testing Machine (Figure 3).
The device operates on uniaxial pressure (load mode). During experiments the device must meet the following requirements in order to obtain usable results:

- the load must be exactly axial so that no bending effect occurs,
- minimizing friction between the end plate and the pressure plate of the measuring head so that the transverse elongation of the measuring head is not limited,
- such a length-to-diameter ratio must be selected in which the risk of buckling does not yet exist.

DOI: https://doi.org/10.14232/analecta.2020.2.61-68

Figure 3. Lloyd 1000R Material Testing Machine

The device perfectly shows the compressive force given to the material as a function of the distance travelled by the measuring head. The machine records the data during the measurement and draws the force-displacement curve in a coordinate system (displacement in mm on the x-axis, force in N on the y-axis). Based on the data, we can immediately see the amount of force that the given material can no longer withstand and it is going to break. Depending on the values of 0 N and maximum N in the graph and the path length assigned to them, we can determine the maximum force which is required to break the material, hereinafter referred to as the breaking force, and the associated breaking work which is determined by the area under the curve. We can determine the deformation modulus from the force-displacement curve. For the measurements, the measuring head, the speed and the height change must be set (Lloyd Instruments 1991).

3. RESULTS AND DISCUSSION

In our studies, we encountered different curves (described above) that nicely showed the relationship with the structure of the material. In the case of agricultural materials, it is clear from Figure 4 (wheat) that the material has a so-called biological pour point (circled in the figure). This is the point on the force-displacement (tension-deformation) curve from where the tension decreases or remains constant as the deformation increases. This point indicates that an initial fracture occurs in a small volume of the cell system. Therefore below this point the structure has not changed yet, but above this point even if it is not visible to the eye, the structure of the material is already damaged.

DOI: https://doi.org/10.14232/analecta.2020.2.61-68

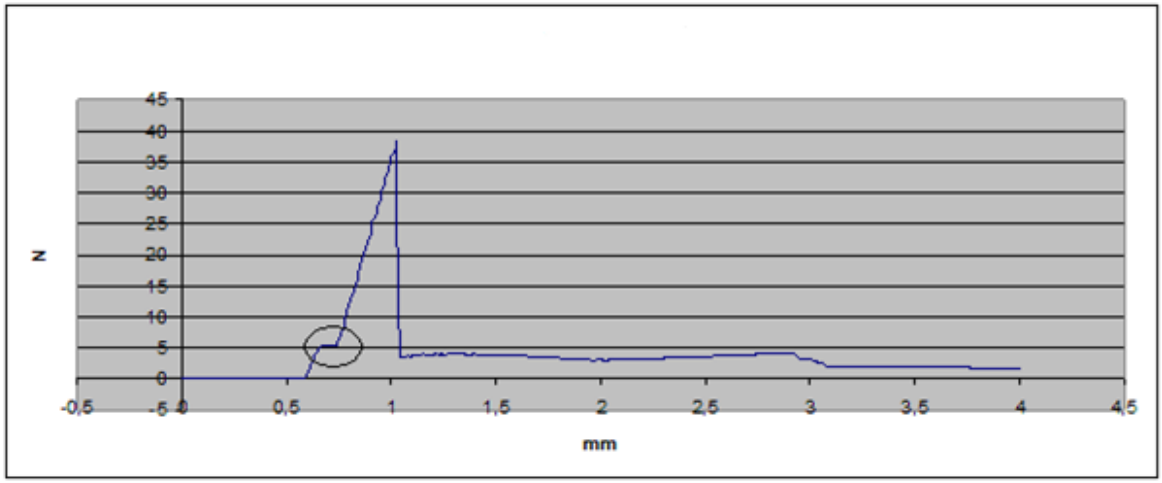

Figure 4. The force-displacement curve of wheat

By looking at the course of the curve, after the previously mentioned point we reach the breaking point (maximum breaking force). This point is the point on the force-displacement (tension-deformation) curve where the tension decreases sharply and significantly as the deformation increases. This point indicates that a significant volume of the material fractured. The curve shows that this point is reached steeply, over a very short exposure range (~0,5mm), thus we are dealing with a rigid, hard material. This initial, rapid ramp-up of the curve can also be characterized by the direction tangent of a more or less straight section. This is nothing more than the modulus of elasticity, which is an excellent material characteristic figure.
In contrast, in case of a soft, resilient material, fracture occurs after significant plastic deformation. Such a course is seen in Figure 5 (fish meat). Here it is clear that the substance has a biological pour point (circled in the figure) in the same way. Due to the nature of flexible materials, the curve shows that the maximum force required for complete fracture is reached slowly, after a long penetration distance (and does not have such a classic visible maximum breaking force), so as opposed to a hard, rigid material, the curve does not rise steeply. This elastic change can be clearly seen from the beginning of the measurement.

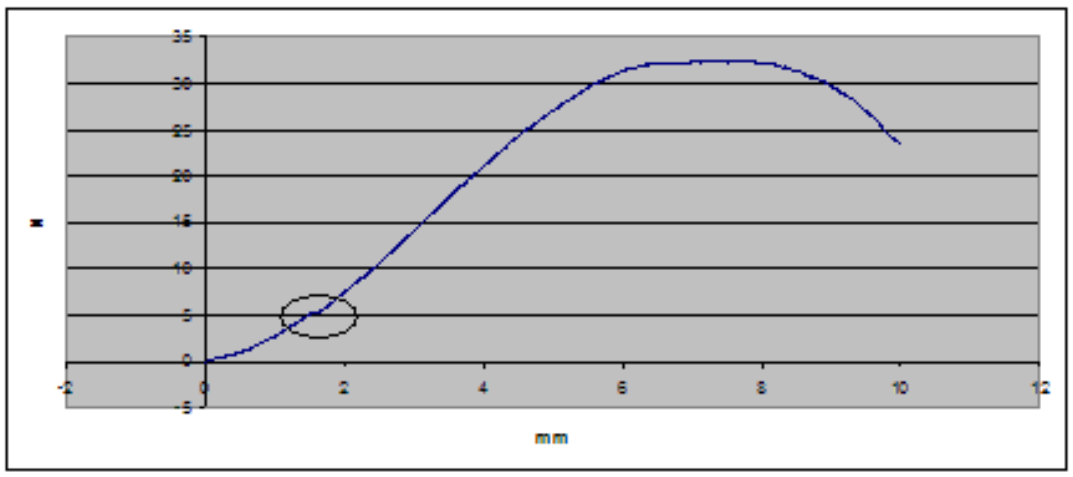

Figure 5. The force-displacement curve of fish meat

DOI: https://doi.org/10.14232/analecta.2020.2.61-68

Interesting results can be found when teeth are loaded and tested, which highly depend on the mechanical properties (elastic modulus, flexural strength, fracture toughness) of the materials used to restore the teeth, the positioning (extracoronal or intracoronal) of the restorative materials, and also the way the restorative material is luted to the dental structures, tissues. In case of correctly using the now widespread and most commonly used adhesive dentistry to restore teeth the restorative material will form a unit with the adhering dental structures and their mechanical properties will cummulate. It is important to note that both fracture resistance and the pattern of fracture will be determined by the amount of restorative material used to substitute the missing dental tissues, and also by the similarity between the mechanical features of the substituted dental tissues and the used restorative materials. Originally for a direct filling dentists use a less elastic restorative material (packable composite resin), which more resembles enamel than dentin regarding its mechanical properties. This is nicely shown by the brittleness, low fracture toughness and high wear resistance of packable composite resins. These materials rather behave as rigid materials on their own and even inside the tooth (Figure 6.). This results in unfavorable fracture pattern going through the tooth-restoration unit when of fracture occurs.

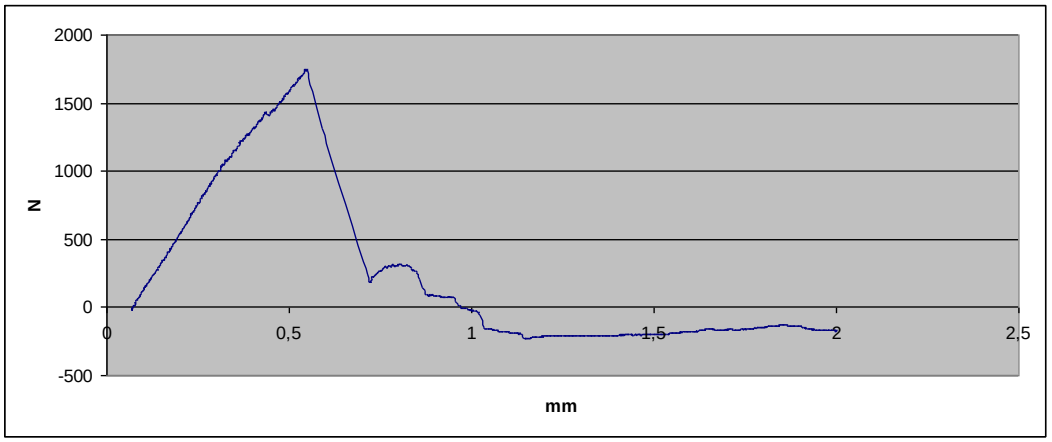

Figure 6. Curve showing a fatal, unrepairable fracture in case of restored teeth

The difference in mechanical features of different restorative materials become visible and clinically relevant when significant amount of dentin needs to be substituted during the restorative procedure (Forster et al, 2018). The reason behind this is the remarkable elasticity of dentin, leading to a unique stress-reducing and crack-arresting feature (Figure 7.) (Lassila et al, 2018). Thus it is logical that in case of severe dentinal loss the tooth can only be reinforced if the operator uses a highly elastic material to replace the missing dentin. The fracture toughness and flexural strength of new short fiber-reinforced composite materials are similar to that of dentin's, therefore they behave as elastic materials (Lassila et al, 2018).

DOI: https://doi.org/10.14232/analecta.2020.2.61-68

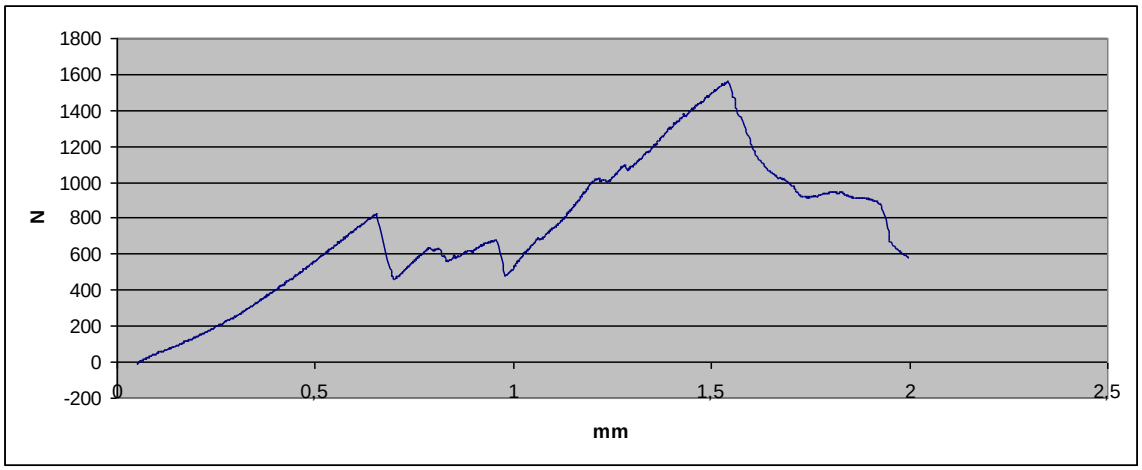

Figure 7. Curve showing the fracture resistance of an elastic materials

Many studies have shown that better results can be obtained if short fiber-reinforced composite is used rather than conventional composite resin to substitute great amount of missing dentin (Fráter et al, 2019; Fráter et al, 2020; Forster et al, 2016). Furthermore the pattern of fracture is dominantly favorable when using fiber-reinforced composite, meaning the fibers first absorb, then dissipate and redirect the stress in the form of crack and/or fracture towards the surface of the tooth (Figure 8.) (Fráter et al, 2014; Sáry et al, 2020).

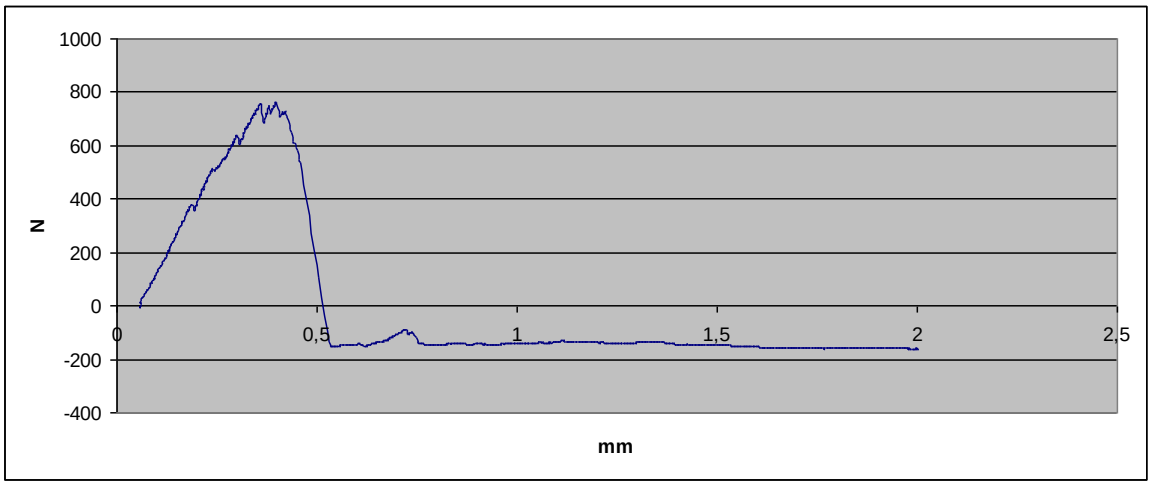

Figure 8. Curve showing the fracture resistance of a tooth restored with short fiber-reinforced composite

4. CONCLUSIONS

Our studies have shown that whatever living matter is used during the mechanical examination, their structure can behave in many different ways under the influence of mechanical action. This behavior is influenced by a number of factors. These factors can also strengthen or weaken each other. In the case of an agricultural material, in addition to the factors influencing the basic structure (e.g.: variety/type),

DOI: https://doi.org/10.14232/analecta.2020.2.61-68

weather, vintage, and fertilization also appear. In case of testing restored teeth the results can be influenced by the medium in which the teeth were kept, cracks and fractures occuring in the teeth before or during extraction, and the age of the tooth (Szabó et al, 2019; Szabó P et al, 2019). Unfortunately not all factors can be standardized during a test like this. In clinical practice all factors which influence the structures of dental hard tissues (developmental diseases of enamel or dentin, the age of the patient, extreme mechanical impact or biting force) can alter the mechanical behavior of the restoration-tooth unit.

REFERENCES

[1] Ferry J.D. (1980): Viscoelastic Properties of Polymers. Wiley New York
[2] Forster A, Braunitzer G, Tóth M, Szabó B.P., Fráter M. (2019): In Vitro Fracture Resistance of Adhesively Restored Molar Teeth with Different MOD Cavity Dimensions. J Prosthodont., 2019
[3] Forster A, Sáry T, Braunitzer G, Fráter M. (2016): In vitro fracture resistance of endodontically treated premolar teeth restored with a direct layered fiber-reinforced composite post and core. J Adhes Sci Technol. 2016;31:1454–66.
[4] Fráter M, Forster A, Keresztúri M, Braunitzer G, Nagy K. (2014): In vitro fracture resistance of molar teeth restored with a short fibre-reinforced composite material. J Dent., 2014, 42(9):1143-50.
[5] Fráter M, Lassila L, Braunitzer G, Vallittu P.K, Garoushi S. (2019): Fracture resistance and marginal gap formation of post-core restorations: influence of different fiber-reinforced composites. Clin Oral Investig. 2020, 24(1):265-276.
[5] Fráter M, Sáry T, Néma V, Braunitzer G, Vallittu P, Lassila L, Garoushi S. (2020): Fatigue failure load of immature anterior teeth: influence of different fiber post-core systems. Odontology, 2020
[6] Lassila L, Keulemans F, Säilynoja E, Vallittu P.K., Garoushi S. (2018): Mechanical properties and fracture behavior of flowable fiber reinforced composite restorations. Dent Mater. 2018, 34(4):598-606.
[7] Lloyd Instruments (1991):Materials testing machines, Operating instructions, Copyright: Lloyd Instruments Limited
[8] Mohsenin N (1968): Physical Properties of Plant and Animal Materials, Gordon and Breach
[9] Peleg M, Bagley E.B. (1982): Physical Properties of Food. AVI Publishing, Westport
[10] Rosenthal A.J. (1999): Food Texture, Perception and Measurement. Aspen Publishers Gaithersburg, 89 p.
[11] Sáry T, Garoushi S, Braunitzer G, Alleman D, Volom A, Fráter M. (2019): Fracture behaviour of MOD restorations reinforced by various fibre-reinforced techniques - An in vitro study. J Mech Behav Biomed Mater, 2019
[12] Sitkei Gy. (1981): Mezőgazdasági anyagok mechanikája, Akadémiai Kiadó, Budapest
[13] Steffe J.F. (1996): Rheological Methods in food Process Engineering, 2nd ed. Freeman Press, East Lansing.
[14] Szabó B, Garoushi S, Braunitzer G, Szabó P.B, Baráth Z, Fráter M. (2019): Fracture behavior of root-amputated teeth at different amount of periodontal support – a preliminary in vitro study. BMC Oral Health. 2019, 19(1):261.
[15] Szabó P.B, Sáry T, Szabó B. (2019): The key elements of conducting load-to-fracture mechanical testing on restoration-tooth units in restorative dentistry. Analecta Technica Szegedinensia. 2019 Vol. 13, No. 2.

DOI: https://doi.org/10.14232/analecta.2020.2.61-68

Analecta Technica Szegedinensia
Vol. 14, No. 2 ISSN 2064-7964 2020

IMPACT ASSESSMENT OF MICROWAVE TREATMENT OF RAW COW'S MILK ON ITS MICROBIOLOGICAL PROPERTIES

[1]Viktória Kapcsándi, [1]Martin Cserpán, [1]Erika Hanczné Lakatos

[1]Institute of Food Science, Faculty of Agricultural and Food Sciences, Széchenyi István University, Lucsony utca 15-17., H-9200, Mosonmagyaróvár, Hungary
e-mail: kapcsandi.viktoria@sze.hu

Received: November 11, 2020 • Accepted: December 6, 2020

ABSTRACT

The aim of our research was to examine the impact of microwave radiation on the microbiological parameters of raw cow's milk. In the measurements, our samples (raw cow's milk) were treated at different power levels [100, 200, 300, 400, 496 (~500), and 600 W], and the effects of microwave irradiation were assessed regarding total plate count and yeast cell count. Treatment temperature was maximized in all cases (40 °C) in order to eliminate the thermal effect generated by microwaves, and hence, to justify the possible microbial inhibitor or destruction impact of the non-thermal effect of radiation. Based on the results, microwave treatment had an impact on both the total plate count and the yeast cell count as well. Treatments were performed to justify the non-thermal effect of the treatments, and significant results were obtained ($p \leq 0.05$).

Keywords: cow's milk, microwave radiation, microbial destruction impact

1. INTRODUCTION

Microwave equipment are widely used today in households, in health care and in the agri-food industry as well where they are used for drying, baking, sterilizing, pasteurizing, defrosting and tempering purposes as well. For this reason, other possible uses of microwaves have been widely investigated, the importance of which is based on the fact that in traditional heat treatment procedures, food is heated up from the outside towards the inside whereas the process takes place in the exact opposite way in case of microwave treatment. The food heating property of microwaves as well as the changes that this implies is well known, however much less information is available on their actual impact on content quality and microbiological properties of food, not being associated with the temperature increase.

Microwaves are electromagnetic waves with a wavelength (λ) ranging from 1 m to 1 mm, hence, they are similar to light waves that are visible to the naked eye or to X-rays emitted by X-ray equipment, and even if they are only different with regards to their wavelength, frequency and energy, there are still huge deviations between each range [1]. The frequency of microwaves varies between 0.3 and 300 GHz, and they are classified under the so-called non-ionizing radiations which means that they do not have sufficient energy to create ions. These waves are used in various sectors, and radar technology can be probably considered the most important of them because it is thanks to this field that the heating property of microwaves has been revealed as well. They also play an important role in telecommunications, given that they penetrate much more efficiently through the atmosphere of the Earth as compared to other wavelengths. In telecommunication devices, microwaves are also used by Bluetooth and WLAN, and the 2.45 GHz frequency is used in general in household appliances for heating food [2].

Researches on the application and possible effects of microwaves have been carried out in several fields already, such as in sample preparation, wastewater treatment, increasing enzymatic activity, impact on fermentation and milk fat determination methods. It has been shown for example that using microwaves, certain processes may be shortened such as the derivatization of fatty acids in milk samples for HPLC-based analysis for example [3]. In the research conducted on the removal of ammonia nitrogen from biological wastewaters it has been shown that as compared to conventional heat transmission, thermal effects were complemented by non-thermal effects in the samples heated with microwave (700 W, 2450 MHz) to achieve a higher removal efficiency [4]. Another research conducted with microwave

DOI: https://doi.org/10.14232/analecta.2020.2.69-76

treatment of agri-food industry wastewaters has shown that the Fenton-reaction combined with microwave can reduce the biological and chemical oxygen demand [5]. Beszédes et al. [6] investigated the degradability of dairy by-products by microwave treatment. Lakatos et al. [7] worked out a method in their experiments that allowed to determine the fat content of various milk samples with sufficient accuracy using microwave treatment. In subsequent researches the influence of microwave radiation on lipase and xanthine oxidase enzyme activity was analyzed in consumer milks due to which an increase of enzymatic activity was found in the milk samples [8]. Certain researches show that a higher increase in glucose content was achieved for microwave treated vine-branch samples treated with cellulose enzyme, hence justifying the increase of enzymatic activity [9].

Besides all the above, the analysis of its impact on microorganisms also constitutes the subject of several researches. In case of analyzing the impact on microbes the phenomenon may be approached from several perspectives. It may be examined based on the frequency applied, on the power applied, on the final temperature of the irradiated sample or from the perspective of the irradiation time. When these types of experiments are conducted, it is important to differentiate thermal effects from non-thermal ones.

In the experiment of Roohi and Hashemi [10] *Enterococcus faecalis, Bacillus cereus, Staphylococcus aureus* and *Shigella flexneri* hosted on carrot slices were analyzed using radiation at various power levels. Power values were selected as 200, 400 and 600 W. It has been stated that a higher power level results in a higher microbial destruction impact even without a significant temperature effect. In other researches, the analysis of microwave irradiation of *Salmonella enteritidis* in potato omelet at various power levels has shown that this microorganism is resistant to high-power microwaves in such a medium. Inactivation of the microbe population was detected even in case of radiation at 600 or 800 W only after a significant rise in temperature (60 °C) [11]. The analysis of *Escherichia coli* O157:H7 performed in salsa has shown that in case of irradiation at 915 MHz and 4.8 kW, population started to decline only due to a temperature influence and not as a result of irradiation [12]. Nevertheless, the period of treatment in the above experiments has been defined as a short time range of only several minutes, and longer exposure might lead to a different outcome.

Kapcsándi [13] proved that low-power (50 W) microwave treatment makes a positive impact on the life activity of *Saccharomyces cerevisiae* (30 °C), therefore the influence on microbes strongly depends on the power level applied. This effect has been proven by the increase of the glucose utilization capacity of yeast during fermentation processes. By the exposure of *Escherichia coli* and Bacillus *subtilis* to the same microwave radiation it has been shown that even though the cells had been inactivated, their lysis had not taken place. [14].

From a microbiological perspective, milk can be considered to be sterile, it is contaminated when milking is performed. The microbiological status of raw milk depends on various factors such as the lactation period or the cow breed [15].

2. MATERIALS AND METHODS

2.1. Applied materials and tools

In order to analyze the impact of microwaves on microorganisms raw milk has been used as raw material, procured from a raw milk vending machine (in Mosonmagyaróvár). The bottles used for transporting the milk had been sterilized by autoclave (121 °C, 20 min) to exclude contamination. Our experiments were conducted at the Department of Food Science using a MARS5 (Microwave Accelerated Reaction System, CEM Corporation, USA) microwave equipment. MARS5 is a sample preparation equipment operated with microwave, applying a frequency of 2455 MHz that corresponds to the frequency used in household microwave ovens. The power configuration settings allowed for the treatment of the samples at an output power of 400, 800 and 1600 W, with a possible modulation of the standard power levels by further increments of 1%.

DOI: https://doi.org/10.14232/analecta.2020.2.69-76

2.2. The method of microwave treatment

Before starting the measurements, the sample processing vessels provided for the microwave equipment were sterilized with hot air (103 °C) in a THELCO 70M drying oven for laboratory use. These processing vessels (HP-500 Plus) are resistant up to a pressure of nearly 2.5 MPa and a temperature of 210 °C.
During the microwave treatments, several power levels (100, 200, 300, 400, 500 and 600 W) have been defined for analyzing non-thermal efficiency. The lowest applied power level was 100 W that was increased by increments of 100 W in case of different samples. The highest power level applied for the treatment was 600 W. Due to the justification of the non-thermal effects of microwave radiation, maximum temperature of the samples was set to 40 °C, using a treatment without temperature holding. Detection of the sample temperature was performed using an optic fiber sensor (RTP-300 Plus) that can be placed in a microwave environment. At all power levels examined, 3 x 75 mL of samples were placed in the microwave treatment equipment, meaning that we were working with three repetitions and three parallel measurements.

2.3. Microbiological analysis

Pour plate method was used for the development of microorganisms. From the perspective of food safety and technological hygiene, the critical limit for total plate count is at 105/cm3 in raw milk because in order to obtain sufficient efficiency, pasteurizing processes may be used in case of such microbial counts.
Sample preparation was performed based on the MSZ EN ISO 6887-1:2017 [16] standard. Milk samples had been stored in refrigerator (on 4 °C) until testing, and homogenized by shaking before the decimal dilutions were done. To prepare the decimal dilution line, 9 ml of the peptone water was put in test tubes, which were then sterilized in pressure cooker for 30 minutes at about 120 °C. Peptone water contained 8.5 g of sodium chloride (VWR International Ltd., Hungary) and 1.0 g of peptone (Merck Kft., Hungary), dissolved in distilled water, then sterilized.
Based on the MSZ EN ISO 4833-1 [17] standard, determination of the total microbial count was performed on a PC (Plate Count, Biolab) agar, with an incubation time of 72 hours, at a temperature of 30±1 °C. Determination of the yeast and mold count has been performed on the selective agar defined in the MSZ ISO 7954:1999 [18] standard, incubated at 25 °C for 48 hours. As defined in the standard, YGC agar (Yeast Extract Glucose Chloramphenicol Agar, Biolab) has been used for their indication.
Our measurement results have been plotted using Microsoft Office Excel 2016®. During the interpretation of microbiological results, the microbial count has been plotted in a logarithmized format, with the gradient values of the straight lines fitted to specific points characterizing the exponential propagation phase of microorganisms.

3. RESULTS AND DISCUSSION

3.1. Heating trends in the samples

During microwave treatments, a temperature profile has been defined for the treatment at each power level in order to (*Fig.1*) demonstrate the decrease of the treatment time occurring due to the increase of power. It can be seen that there is a linear connection between the two values, and the value of the correlation coefficient is 0.98, therefore there is a strong relationship between the applied power and the speed of heating at the power levels examined.

DOI: https://doi.org/10.14232/analecta.2020.2.69-76

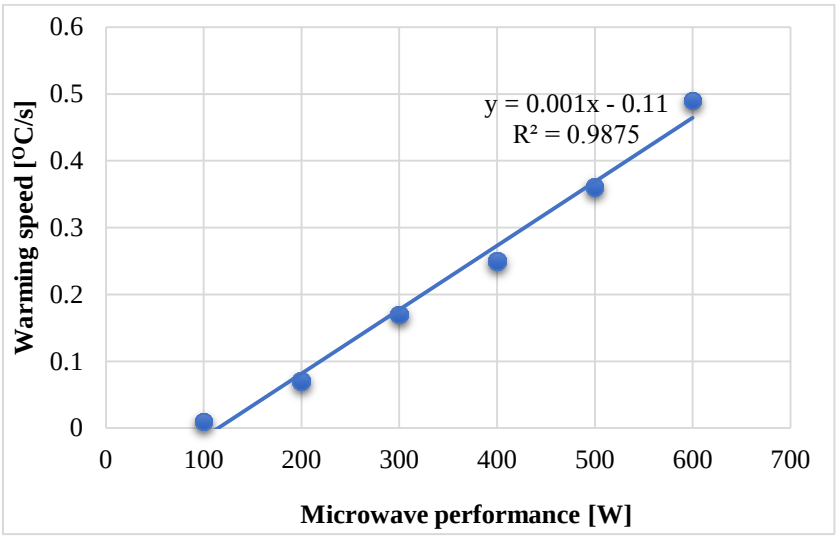

Figure 1. Heating speed of samples against power

3.2. Impact of the treatments on total plate count

Fig.2 shows that during the microwave treatment of raw milk, by increasing the microwave power, the total plate count decreases in milk. These results indicate that already in case of a treatment at 100 W, the cell count of 8.54 log CFU/cm^3 decreased to 6.24 log CFU/cm^3. This clearly represents a significant deviation ($p \leq 0.05$). Comparing the samples, it can also be seen that except for the treatments at 200 and 300 W, by comparing the results of other samples, significant differences can be found in all cases when the results of the culture are interpreted.

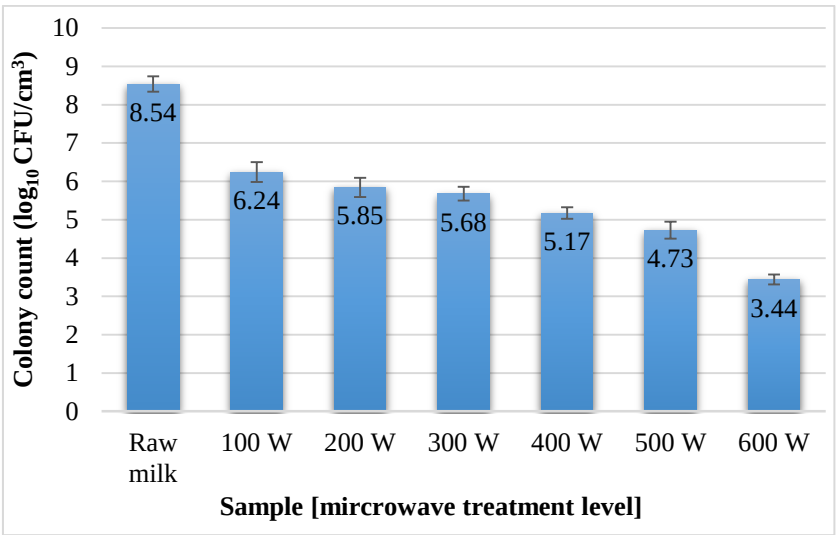

Figure 2. Total plate count results of raw milk and microwave treated

Tremonte et al. [19] conducted similar experiments. Samples were also procured from milk vending machines, then treated with microwave at 750 and 900 W and a treatment time of 75 s, using a household

DOI: https://doi.org/10.14232/analecta.2020.2.69-76

microwave oven. The results of their total plate count measurements in raw milk were similar to those of our experiments. In their experiment, a 750 W treatment resulted in a destruction of 1 magnitude regarding total plate count, whereas the 950 W treatment gave an almost sterile result. In our case, the 600 W treatment resulted already in a destruction of 5 magnitudes, with a treatment time of 47 s.
Jaynes [20] performed research on pasteurization of raw milk in a microwave system. A countercurrent heat-exchanger has been used in the equipment for heating up the inflowing milk and for cooling back the outflowing milk. During the treatment, the pasteurization temperature was tried to be kept at 72 °C. The experiments were performed with various flow rates, in case of which temperature differences were corrected by modulating the power. In addition to the microwave treatment, control samples have been treated in a 62.8 °C water bath that produced a similar result with regards to microbial destruction. The most important microbial destruction was stated in case of the treatment with a flow rate of 300 mL/min and a power level of 735 W.

3.3. The impact of the treatments on yeast count

In addition to the determination of yeast count, cultivation on a YGC agar is suitable for determining the mold count as well. However mold was not present in such volumes in our samples that would allow for drawing numerical data and conclusions, therefore in our analysis, the emphasis was put on the results obtained for yeast counts.
Fig.3 indicates that microwave radiation of various doses has an impact on the presence of yeast as well. Although, no significant difference can be shown between the samples of 200-300-400 W ($p \leq 0.05$), a clear destruction can be identified as compared to the results of raw milk, in case of which a decrease of yeast cell count of 1 magnitude can be observed from an initial cell count of 5.56 log CFU/cm^3 to cell counts of 4.28-4.23-4.15 log CFU/cm^3. In case of a power level of 400 W, the results obtained are even more striking, during which the cell count of yeast decreased to 2.06 CFU/cm^3, and, in case of even higher power levels (500 and 600W), to 0.65 and 0.18 log CFU/cm^3 as compared to the initial value. This severe destruction means a destruction rate of 89.4% in case of 500 W and 96.8% in case of 600 W.

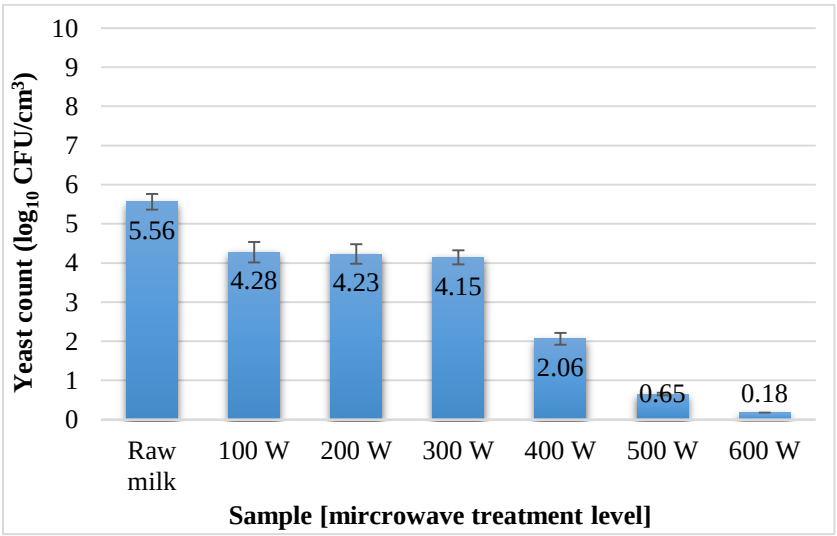

Figure 3. Yeast cell count results of raw milk and microwave treated samples

The data indicate that microwave irradiation has a smaller impact on yeast at lower power levels, however, a sharp increase can be identified when a power level of 600 W is applied, reaching a rate of 96%.

DOI: https://doi.org/10.14232/analecta.2020.2.69-76

This corresponds to the experiments of Kapcsándi [13] where *Saccharomyces cerevisiae* suspensions were examined at similar power levels and treatment times. In their case, the survival rate of yeast presented a higher value, but the extent of destruction followed the same trend. With regards to deviations in survival rates it should be noted however that in their case one type of yeast was examined, the size of the sample treated at once was more than twice as large, and the medium containing the microbes was also different, hence, the much higher destruction rates might have been caused by these factors.

Ali et al. [21] conducted experiments to examine the impact of 900 W microwave treatment on microbes, namely yeast amongst others in raw buffalo milk, using various treatment times and hence temperatures. In their case, the initial 5.23 log CFU/cm^3 value decreased to 3.6 log CFU/cm^3 using a treatment time of 30 s. However, based on our results, the initial 6.61 log CFU/cm^3 value decreased to 4.18 log CFU/cm^3 using a treatment time of 47 s with the highest power level of 600 W. In our case, the more severe microbial destruction can be justified by the fact that the liquid column of our samples was much narrower, and this way, microwaves penetrated even into the middle of the sample with less damping as compared to the above mentioned experiment. Hence, it can be concluded that microwave treatments are most efficient in narrow processing vessels because a better penetration into the material can significantly increase the destruction impact of microwaves.

Although, several papers have been published already on the non-thermal microbe destruction impact of microwaves, the microwave pasteurization processes currently used in the dairy industry are still only based on the thermal impact. Our experiments have shown that an increased power can significantly hold back microbiological life activities already at a lower temperature of 40 °C, even in case of using very short treatment times. It should be noted that in our case, samples have been treated in predefined portions with a small sample size, and in order to be able to apply this microbial inhibitor property to larger extents, the size of the treatable sample should be increased.

The simplest solution for increasing the sample size is to use a continuous flow treatment equipment in which the materials to be treated flow through a coil in the microwave treatment zone. Such an equipment would offer a large variety of control options in order to reach the most suitable result with regards to the microbe inhibitor effect. Given that in this case, non-thermal effects of microwave are desired to be used, power should be kept static, but in this case, the final temperature of the material would depend on the initial temperature, and parameters could only be controlled by modulating the flow rate or by modifying the dimensions of the treatment equipment. Nevertheless, if power control was possible, by building such an equipment, it would be possible to define more precisely the power level where the method could be applied in the most cost-efficient manner.

The results indicate that the microbial destruction impact is more present with regards to the decrease in the yeast cell count as compared to the total plate count. Taking this into account, the destruction properties of other microorganisms that can be found in milk may be subject to further analysis.

4. CONCLUSIONS

Heat treatment of raw milk is one of the key technological steps in the agri-food industry, and especially at milk processing plants. Heat treatment of the raw material, and hence, guaranteeing its microbiological safety are in the interest of both the producers and the consumers as well. Besides the conventional heat treatment process, microwave treatment has been present in various sectors of the agri-food industry. This type of process could be introduced as a new technology in the dairy industry, using which the non-thermal effect produced by the microwaves could be applied during the manufacturing of the products, enjoying the benefits of low-impact raw material handling at a lower temperature, and reducing the deterioration of content quality parameters.

DOI: https://doi.org/10.14232/analecta.2020.2.69-76

ACKNOWLEDGEMENT

The project is supported by the European Union and co-financed by the European Social Fund (Grant Agreement No. EFOP-3.6.1-16-2016-00024).

REFERENCES

[1] L.A. Vainshtein, Elektromagnitnye Volny [Electromagnetic Waves] Radio i Svyaz, Moscow, 1988
[2] D. M. Pozar, Microwave Engineering, Fourth Editions, University of Massachusetts at Amherst, John Wiley & Sons, Inc, 2012, pp. 658-712.
[3] R. Shrestha, Y. Miura, K. I. Hirano, Z. Chen, H. Okabe, H. Chiba, S. P. Hui, Microwave-assisted derivatization of fatty acids for its measurement in milk using high-performance liquid chromatography, Analytical Sciences, 34 (5) (2018), pp. 575-582. https://doi.org/10.2116/analsci.17P557
[4] L. Lin, S. Yuan, J. Chen, Z. Xu, X. Lu, Removal of ammonia nitrogen in wastewater by microwave radiation, Journal of Hazardous Materials, 161(2-3) (2009), pp. 1063-1068. https://doi.org/10.1016/j.jhazmat.2008.04.053
[5] M. Zakar, D.I. Farkas, E. Lakatos, G. Keszthelyi-Szabó, Zs. László, Purification of model dairy wastewaters by ozone, Fenton pre-treatment and membrane filtration, Periodica Polytechnica-Chemical Engineering, 64(3) (2020), pp. 357-363. https://doi.org/10.3311/PPch.15046
[6] S. Beszédes, Z. Jákói, B. Lemmer, C. Hodúr, Enhanced biodegradability of dairy sludge by microwave assisted alkaline and acidic pre-treatments, Review on Agriculture and Rural Development, 7(1-2) (2019), pp. 92-97.
[7] E. Lakatos, A.J. Kovács, M. Neményi, Milk fat content determination by combined physical (microwave and convective dehydration) method, Milchwissenschaft-Milk Science International, 65(4) (2010), pp. 373-376.
[8] E. Lakatos, A.J. Kovács, V. Kapcsándi, M. Neményi, Influence of the cellobiase enzyme activity by microvawe radiation. [Alacsony teljesítményű mikrohullámú sugárzás hatása a cellobiáz enzim működésére], Acta Agronomica Óváriensis, 54(1) (2012), pp. 3-11.
[9] V. Kapcsándi, M. Neményi, E. Lakatos, Microwave steam explosion and enzymatic hydrolysis of vine-branch, Acta Alimentaria, 47(4) (2018), pp. 443-452. https://doi.org/10.1556/066.2018.47.4.7
[10] R. Roohi, S.M.B Hashemi, Experimental, heat transfer and microbial inactivation modelling of microwave pasteurization of carrot slices as an efficient and clean process, Food and Bioproducts Processing, 121(2020), pp. 113–122. https://doi.org/10.1016/j.fbp.2020.01.015
[11] A. Valero, M. Cejudo, R.M. García-Gimeno, Inactivation kinetics for *Salmonella enteritidis* in potato omelet using microwave heating treatments, Food Control, 43(2014), pp. 175-182. https://doi.org/10.1016/j.foodcont.2014.03.009
[12] H. J. Sung, D. H. Kang, Effect of a 915 MHz microwave system on inactivation of Escherichia coli O157: H7, *Salmonella typhimurium*, and *Listeria monocytogenes* in salsa, LWT-Food Science and Technology, 59(2) (2014), pp. 754-759.
[13] V. Kapcsándi, A.J. Kovács, M. Neményi, E. Lakatos, Investigation of a non-thermal effect of microwave treatment, Acta Alimentaria, 45(2) (2016), pp. 224-232. https://doi.org/10.1556/066.2016.45.2.9
[14] I. S. Woo, I. K. Rhee, H.D. Park, Differential damage in bacterial cells by microwave radiation on the basis of cell wall structure, Applied and Environmental Microbiology, 66(5) (2000), pp. 2243-2247. DOI**:** 10.1128/AEM.66.5.2243-2247.2000

[15] F. M. Petróczki, T. A. Tonamo, B. Béri, F. Peles, The effect of breed and stage of lactation on the microbiological status of raw milk, Acta Agraria Debreceniensis, 2019(1), pp. 37-45. https://doi.org/10.34101/actaagrar/1/2367 37
[16] Hungarian Standards Institution, Microbiology of the food chain. Preparation of test samples, initial suspension and decimal dilutions for microbiological examination. Part 1: General rules for the preparation of the initial suspension and decimal dilutions (ISO 6887-1:2017), Retrieved from: https://prod.mszt.hu/hu-hu/, 2017
[17] Hungarian Standards Institution, Microbiology of the food chain. Horizontal method for the enumeration of microorganisms. Part 1: Colony count at 30 degrees C by the pour plate technique (ISO 4833-1:2013), Retrieved from: https://prod.mszt.hu/hu-hu/, 2014
[18] Hungarian Standards Institution, Microbiology. General guidance for enumeration of yeasts and moulds. Colony count technique at 25 °C [MSZ ISO 7954:1999.], Retrieved from: https://prod.mszt.hu/hu-hu/, 1999
[19] P. Tremonte, L. Tipaldi, M. Succi, G. Pannella, L. Falasca, V. Capilongo, E. Sorrentino, Raw milk from vending machines: Effects of boiling, microwave treatment, and refrigeration on microbiological quality, Journal of Dairy Science, 97(6) (2014), pp. 3314-3320. https://doi.org/10.3168/jds.2013-7744
[20] H. O. Jaynes, Microwave pasteurization of milk, Journal of Milk and Food Technology, 38(7) (1975), pp. 386-387.
[21] M.A. Ali, K. A. A. Khater, S. A. Soliman, The effect of microwave treatment as compared to heat treatments on microbiological quality of raw milk, Journal of Food Industries and Nutrition Science, 5(1/2) (2015), pp. 13-23.

DOI: https://doi.org/10.14232/analecta.2020.2.69-76